

AD_____

Award Number: W81XWH-11-1-0493

TITLE: Development of Magnetic Resonance Imaging Biomarkers for
Traumatic Brain Injury

PRINCIPAL INVESTIGATOR: E Mark Haacke

CONTRACTING ORGANIZATION:

Wayne State University, Detroit, Michigan 48201

Á

REPORT DATE:

Ju→] 2013

TYPE OF REPORT: Ô↔^al

PREPARED FOR: U.S. Army Medical Research and Materiel Command
Fort Detrick, Maryland 21702-5012

DISTRIBUTION STATEMENT: (Check one)

X ☐ Approved for public release; distribution unlimited

REPORT DOCUMENTATION PAGE				Form Approved OMB No. 0704-0188	
Public reporting burden for this collection of information is estimated to average 1 hour per response, including the time for reviewing instructions, searching existing data sources, gathering and maintaining the data needed, and completing and reviewing this collection of information. Send comments regarding this burden estimate or any other aspect of this collection of information, including suggestions for reducing this burden to Department of Defense, Washington Headquarters Services, Directorate for Information Operations and Reports (0704-0188), 1215 Jefferson Davis Highway, Suite 1204, Arlington, VA 22202-4302. Respondents should be aware that notwithstanding any other provision of law, no person shall be subject to any penalty for failing to comply with a collection of information if it does not display a currently valid OMB control number. PLEASE DO NOT RETURN YOUR FORM TO THE ABOVE ADDRESS.					
1. REPORT DATE July 2013		2. REPORT TYPE Final		3. DATES COVERED 2 June 2011 - 1 June 2013	
4. TITLE AND SUBTITLE Development of Magnetic Resonance Imaging Biomarkers for Traumatic Brain Injury				5a. CONTRACT NUMBER	
				5b. GRANT NUMBER W81XWH-11-1-0493	
				5c. PROGRAM ELEMENT NUMBER	
6. AUTHOR(S) E Mark Haacke email: nmrimaging@aol.com				5d. PROJECT NUMBER	
				5e. TASK NUMBER	
				5f. WORK UNIT NUMBER	
7. PERFORMING ORGANIZATION NAME(S) AND ADDRESS(ES) Wayne State University, Detroit, Michigan 48201				8. PERFORMING ORGANIZATION REPORT NUMBER	
9. SPONSORING / MONITORING AGENCY NAME(S) AND ADDRESS(ES) U.S. Army Medical Research and Materiel Command Fort Detrick, Maryland 21702-5012				10. SPONSOR/MONITOR'S ACRONYM(S)	
				11. SPONSOR/MONITOR'S REPORT NUMBER(S)	
12. DISTRIBUTION / AVAILABILITY STATEMENT Approved for Public Release; Distribution Unlimited					
13. SUPPLEMENTARY NOTES					
14. ABSTRACT The purpose of this research program is to develop an imaging-based protocol to improve diagnosis and outcome prediction of mild traumatic brain injury (mTBI). Our major findings over the last year include: First, we have demonstrated that these new advanced MRI methods nicely complement conventional imaging methods in their ability to detect mTBI in the acute setting. Second, susceptibility weighted imaging and mapping (SWIM) are able to delineate venous structures and microbleeds making it possible to quantify and monitor evolution of pathological changes. Third, we have continued to use DTI data to look for local variations in ADC and FA values to assess tissue damage. And fourth, we have begun to accelerate the data collect process in patients with added support in both Radiology and Emergency medicine for both volunteers and mTBI patients. The significance of this work to date is that we are now able to find evidence of damage in mTBI where that has heretofore been difficult with conventional MRI. Keywords: Mild traumatic brain injury, susceptibility weighted imaging and mapping, temporal nature of TBI recovery, medullary vein damage					
15. SUBJECT TERMS- none provided					
16. SECURITY CLASSIFICATION OF:			17. LIMITATION OF ABSTRACT UU	18. NUMBER OF PAGES 96	19a. NAME OF RESPONSIBLE PERSON USAMRMC
a. REPORT U	b. ABSTRACT U	c. THIS PAGE U			19b. TELEPHONE NUMBER (include area code)

Table of Contents

	<u>Page</u>
Introduction.....	(
Body.....)
Key Research Accomplishments.....	1'
Reportable Outcomes.....	%
Conclusion.....	1(
Appendices.....	Attachment

The views, opinions and/or findings contained in this report are those of the author(s) and should not be construed as an official Department of the Army position, policy or decision unless so designated by other documentation.

INTRODUCTION

Background: Traumatic brain injury (TBI) has been labeled as a “signature wound” in the anti-terrorism wars in Iraq and Afghanistan. 15% - 25% of surveyed returning service members have been reported to have possible long-term mild traumatic brain injury (mTBI) or concussion. In the civilian sector, the prolonged neuro-cognitive and functional symptoms following mTBI affects over 1.2 million Americans annually. However, our understanding of the neuropathology of mTBI and its recovery process is still very limited due to the lack of sensitive clinical and diagnostic tools. First, current TBI classification scales are mainly based on results from computed tomography (CT) scans of moderate to severe TBI patients, and thus can hardly be applied to mTBI cases. Secondly, current laboratory biological markers, clinical CT and conventional magnetic resonance imaging (MRI) are either insensitive or not specific to the subtle abnormalities in mTBI and poorly predict patient’s long-term outcome. It is in urgent need of developing a set of advanced MR imaging biomarkers that can: i) be sensitive enough to differentiate mTBI patient population from normal healthy subjects, ii) have the potential for outcome prediction; and iii) assist in management of mTBI patients in acute settings.

Objective/Hypothesis: The overall goal of the current research is to develop imaging-based biomarkers to improve diagnosis and outcome prediction of mTBI. Advanced MRI techniques reveal many more details than conventional imaging. For example, susceptibility weighted imaging (SWI) and susceptibility mapping (SWIM) can detect and quantify temporal reduction of hemorrhagic lesions associated with mTBI patients’ functional outcome and diffusion tensor imaging (DTI) can detect axonal injury at the acute stage and possible changes over time. As the next generation of SWI developed in our lab, SWIM will be used to quantify iron in microbleeds and oxygen saturation in major veins throughout the brain. Our central hypothesis is that axonal injury (measured by DTI) and vascular damage (detected as hemorrhagic lesions by SWI/SWIM) are important pathologies in mTBI that are associated with patients’ neurocognitive and clinical symptoms in their recovery.

Study Design: Adult mTBI patients are screened and enrolled at the acute stage (within 24 hours after injury) from the emergency department of our local Level-One Trauma Center. Both up-to-60-minute MRI scan and neuropsychological/clinical assessment will be conducted in mTBI patients. In the subacute (1 month) and chronic (6 months) stages after injury, the patients are brought back to repeat both the MRI scans and neurocognitive evaluations. Age/gender/education-matched healthy controls will be recruited and followed up using the same imaging and neuropsychological protocol of evaluation.

Specific Aims: **Specific Aim 1** is to assess whether the advanced MRI data (SWI and DTI) acquired acutely (within 24 hours after injury) are more sensitive than conventional imaging (CT and cMRI) in detecting mTBI. **Specific Aim 2** is to determine at what time point after the injury (i.e., acute, subacute and chronic) these advanced MR techniques can differentiate mTBI patients from healthy controls. **Specific Aim 3** is to use susceptibility weighted imaging and mapping (SWIM), our next generation of SWI technique, to quantify the amount of iron in microbleeds, to monitor any changes (evolution) of the microbleed over time and to monitor oxygen saturation compared to normal volunteers. And **Specific Aim 4** is to determine which MRI indices have statistically significant associations with neurocognitive outcome in mTBI patients over all time points.

BODY

Summary of the Statement of Work for Phase 1:

Phase I (Years 1-2): Recruit a cohort of 50 mTBI patients from the emergency setting of our local Level-One trauma center, and 50 non-TBI volunteers to establish and validate an image-based diagnostic approach to brain injury.

- a) Screen and enroll mTBI patients; perform the MRI protocol (conventional imaging, DTI and SWI); conduct NP tests and clinical outcome measures.

Due to the late approval of IRB, we started enrollment fairly late (March, 2012). To date, we have successfully recruited 26 mTBI patients and scanned them at the acute stage (within 24 hours after injury). Our momentum dramatically improved this last quarter and we have strong momentum now that we are confident will make it possible to easily complete the study over the next year.

- b) Screen and enroll healthy volunteers and perform the same procedures as mentioned above.

We have successfully enrolled 22 control subjects in the past year. As above, our momentum here has dramatically improved and we are getting key data here for normal controls.

- c) Follow up mTBI patients at 1-month and 6-months after injury and controls at 1-month after first scan by using the same imaging protocol, NP tests and outcome measures.

We have successfully performed 1-month follow up in our 21 patients and 21 controls. We also followed up in all 4 patients who are mature for 6-month follow up.

- d) Analyze data and establish a quantitative approach to identifying abnormal brain voxels on DTI data.

Based on a baseline database for all controls, we developed a lesion load approach to quantifying those abnormal white matter clusters as “lesion load.” Our initial analysis demonstrated that DTI lesion load is significantly correlated with patients’ neurocognitive performance at the acute stage (Pearson correlation coefficient $r=-0.87$, $p<0.02$). Meanwhile, we are in the process of analyzing the test-retest reliability analysis for DTI baseline database.

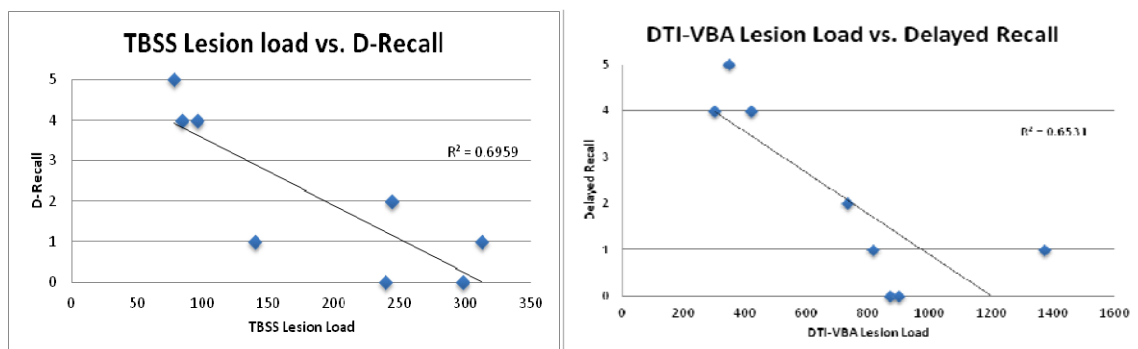


Figure 1. Correlations between DTI lesion load and patients’ neurocognitive data. As demonstrated in the figures, DTI lesion load (both TBSS and VBA data) is correlated significantly with patients’ overall SAC score and delayed recall. R squared values are shown on each figure for linear regression.

e) Correlation MR imaging data with blood biomarker data.

Our pilot data demonstrated that blood biomarker GFAP levels are significantly higher in patients with intracranial bleeding than those without bleeding. This finding has never been reported before. It implies that a blood biomarker might be able to serve as a screening tool for MRI in the acute stage.

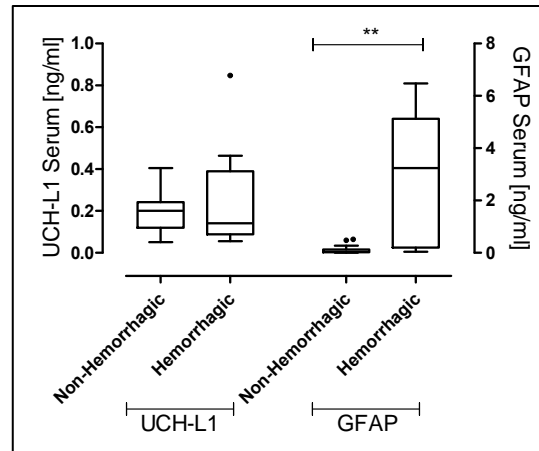


Figure 2. Box-and-whisker plots demonstrating UCH-L1 and GFAP concentrations in patients with ventricular hemorrhages and hemorrhagic contusions and in patients with non-hemorrhagic lesions. The black horizontal line in each box represents the median, with the boxes representing the interquartile range. Significant differences are indicated * ($P < 0.05$) or ** ($P < 0.01$) (Mann–Whitney U-test).

f) Resting state functional MRI (rsfMRI) analysis of mTBI patients at the acute stage.

Our rsfMRI analysis demonstrated up-regulation of patients functional status at the acute stage, which is consistent with the increased cerebral blood flow measured by ASL technique.

Group ICA analysis

The group ICA was performed in two steps: 1) The number of associated voxels to the networks for each desired region and voxels' value were measured. Voxels' value indicates voxel dependency to the networks. 2) "Cross-Validation" was carried out in order to investigate the reliability and the reproducibility and to verify the result of the previous step. Among all investigated areas in DMN and BGN, only the precuneus and the posterior cingulate cortex have shown a difference between the two groups in both the number and the dependency of associated voxels (see Figures 3 and 4). The cross validation results support this difference in the precuneus and the posterior cingulate cortex (see supplement 3 table 2). The voxel-wise analysis was performed on the subgroups' selected networks. The two-sample t-test analysis revealed significant statistical differences for a p-value of 0.001 in the posterior cingulate cortex (50 voxels) and precuneus (442 voxels). Neither voxel value nor the number of voxels reveals a difference in the basal ganglia network regions. To sum up, ICA indicates that there is a group difference between healthy subjects and patients in various regions. The precuneus, the posterior cingulate cortex, and the frontal lobe show significant differences between groups and these differences are constant among difference group ICA analysis. This proves that these regions could discriminate between patients and healthy subjects. In the next step, individual analysis was performed to investigate alteration in patients' resting-state network compared to healthy control subjects at the individual level.

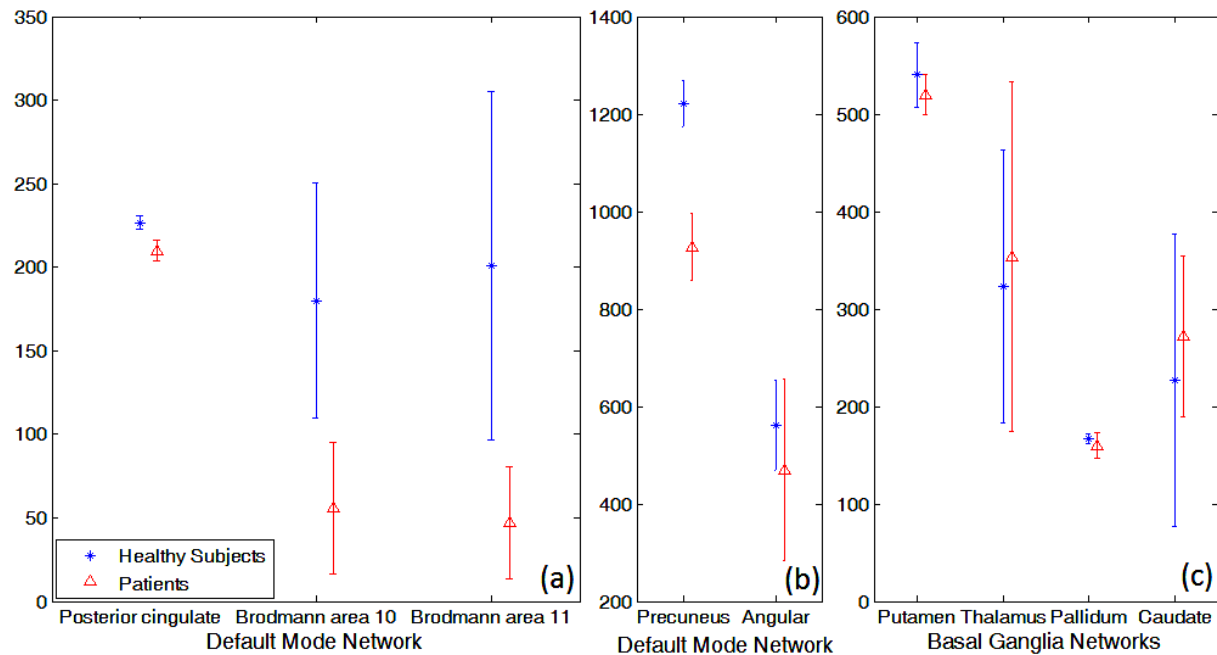


Figure 3. Number of associated voxels to the resting state networks: (a) and (b) Default mode network shows difference between two groups in the posterior cingulate cortex (a) and precuneus (b), and (c) Basal ganglia network does not show a significant difference.

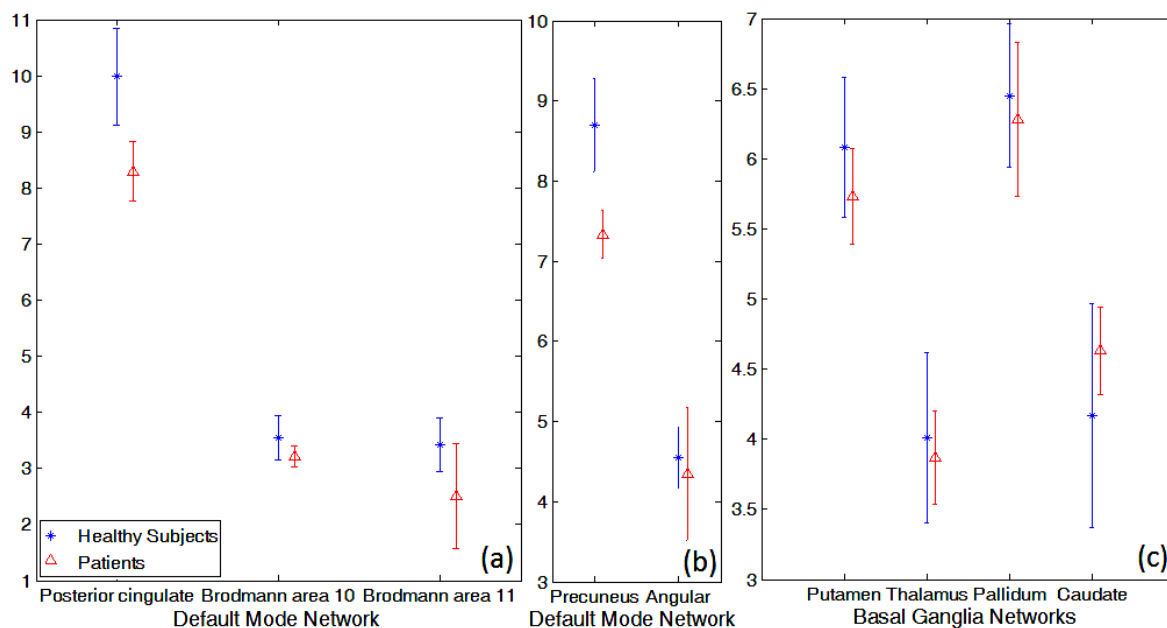


Figure 4. The voxel dependency to resting state networks: (a) and (b) Default mode network shows a difference between the two groups in the posterior cingulate cortex (a) and precuneus (b), and (c). The basal ganglia network shows none.

Individual analysis

All the statistical analyses for group ICA were carried out using all three individual ICA methods. A subject in which either BGN or DMN was not extracted properly was eliminated from further statistical analysis. Neither "dual regression" nor "back-projection", was able to discriminate between the groups in an individual analysis. However, the suggested method, spatial constraint ICA using the chosen template ("A baseline for the multivariate comparison of resting-state networks", Allen, E. A., and et al (2011), demonstrates an intriguing result. The two-sampled t-test analysis on components extracted by using the proposed method reveals a statistically significant difference between two groups especially in the posterior cingulate cortex and surrounding areas like the precuneus in DMN. For $p\text{-value} = 0.05$, the statistical two-sample t-test map, which was corrected by the spatial threshold using MonteCarlo simulation, manifests a cluster with 137 voxels which includes the posterior cingulate cortex (55 voxels) (see Figure 5).

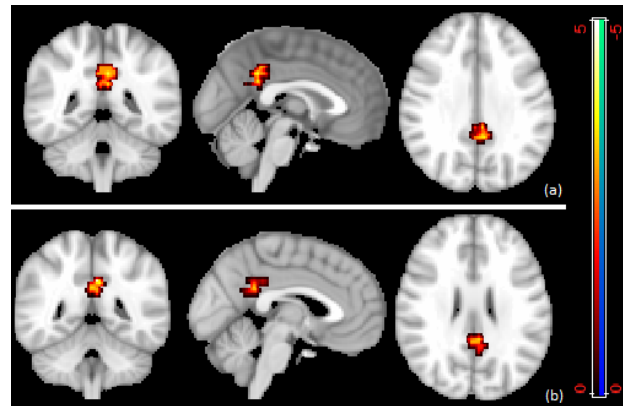


Figure 5. Two-sampled t-test results showing the difference in default mode network (DMN) between two groups in individual independent component analysis (ICA). Panel (a) shows the cluster which is statistically significant ($p=0.05$), and panel (b) shows the result in the posterior cingulate cortex (55 voxels). The warm color labels the region where the healthy group has more activation than patients.

Seed point Analysis

We also performed seed point analysis, which is the most common method in functional connectivity to evaluate the alteration in larger scope using univariate approach. The activation map that was extracted for each subject using the correlation between all voxels in the region and whole brain voxels did not show any significant difference between healthy and patient groups. However, the statistical analysis, which used the average of the time series in the region and measured the group difference, revealed statistically significant results. In the posterior cingulate cortex map, univariate functional connectivity analysis shows that the correlation map in patients group is larger than healthy subjects group, and it is more distributed in patients' brain (includes more region of brain). Patients showed a more powerful connection between the cingulate posterior cortex and the frontal lobe regions. For a $p\text{-value}$ of 0.01, control subjects group includes no functional connectivity in the dorsolateral prefrontal cortex (BA 9) and the anterior cingulate cortex (BA 32), and it includes a few voxels in the anterior prefrontal cortex (BA 10), while patient group is significantly correlated in these regions. One-sample t-test in seed point analysis also demonstrated a group difference in PCC and precuneus, which is consistent with ICA data. The two-sample t-test shows differences between two groups. Notably the dorsolateral prefrontal cortex (BA 9) and adjoining voxels in Brodmann area 8, and the anterior cingulate cortex (BA 32) (see Figure 6). For $p\text{-value}=0.01$, the two-sampled t-test map has two clusters with 117 and 223 voxels. These clusters include 77 and 87 voxels in the dorsolateral prefrontal cortex (BA 9) respectively, and the biggest cluster contains 44 voxels in the dorsal anterior cingulate cortex (BA32) which shows the importance of these regions' liaison in mild-TBI patients.

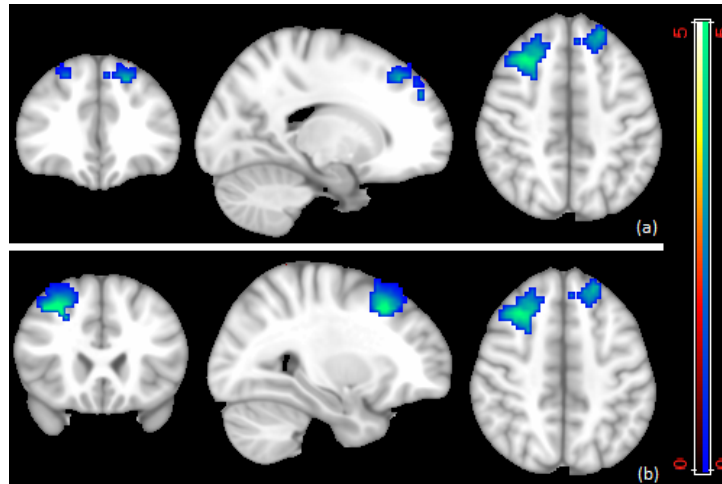


Figure 6. Two-sample t-test ($p=0.01$) for the posterior cingulate cortex correlation map: The cold color labels the region that the patients group has more correlation with the posterior cingulate and the warm color shows the voxels that healthy group has more correlation with the posterior cingulate cortex. Cross bar located in different positions in images a and b.

In the precuneus map, the between group comparison for p -value = 0.05 reveals two regional differences. The first statistically significant region is in the supramarginal gyrus with 82 voxels; the other cluster has 85 voxels, which includes Brodmann area 8 and the interface of the mid-cingulate cortex, the frontal superior, and the sup-motor area (interface Brodmann area 8, 32) (see Figure 7.). Interestingly, almost the same area is statistically significant when the posterior cingulate cortex or the thalamus is a seed region. For one-sample t-test and more details see supplements.

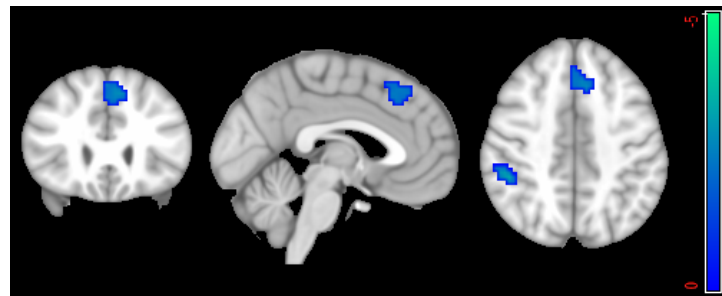


Figure 7. Two-sample t-test ($p=0.05$): The precuneus correlation map shows group difference in the supramarginal gyrus and the interface Brodmann areas 8 and 32. The cold color labels the region that Patients group has more correlation with the precuneus. Additionally, the activated area in BA 32 and BA 8 are also activated, with spatial variation, when the posterior cingulate or the thalamus are used as seed point.

In the next step, the thalamus correlation map was investigated. For p -value = 0.01, between group comparison shows the statistically significant difference between groups in the anterior prefrontal cortex (BA10) (see Figure 8(a)) and part of the supramarginal gyrus (BA 40) (see Figure 8(b)), which indicates the effect of brain injury on the thalamus connections.

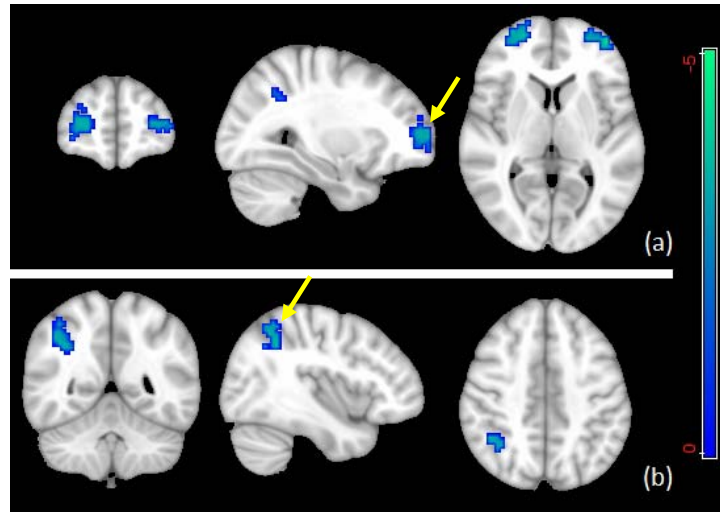


Figure 8. Two-sample t-test ($p=0.01$): The region of interest is in the thalamus and cold color shows the regions that patient group has more correlation with seed point compare to healthy group. (a) indicate that there is a statistical difference between two group at the anterior prefrontal cortex (BA10) and (b) manifest the difference in the supramarginal gyrus (BA 40).

For the amygdala correlation map, the healthy group shows higher connectivity inside the amygdala. For the one-sample t-test and $p\text{-value} = 0.01$, healthy group includes 73 and 67 voxel while for patients group this number decrease to 39 and 22 (see Figure 9). The two-sample t-test ($p\text{-value} = 0.01$) demonstrate significantly increased connectivity in the left parietal superior cortex in the patients group (cluster size = 104) (see Figure 9).

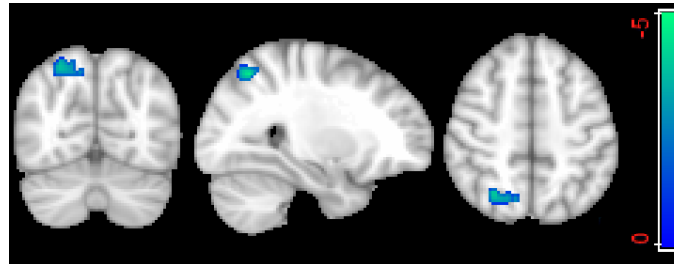


Figure 9. Two-sample t-test ($p=0.01$) for the amygdala correlation map: The cold color labels the region (the left parietal superior cortex) that patients group has more correlation with the amygdala.

The univariate functional connectivity analysis for hippocampus as ROI demonstrates significant alteration in mTBI patients. For $p\text{-value} = 0.01$, three clusters (cluster sizes= 135 ,61, and 52) are significantly difference between two groups. While the increased connectivity in the fusiform gyrus and the somatosensory association cortex (BA 7) are observed in the patients group, the decreased intrinsic connectivity is observed in the BA 48 (see Figure 10).

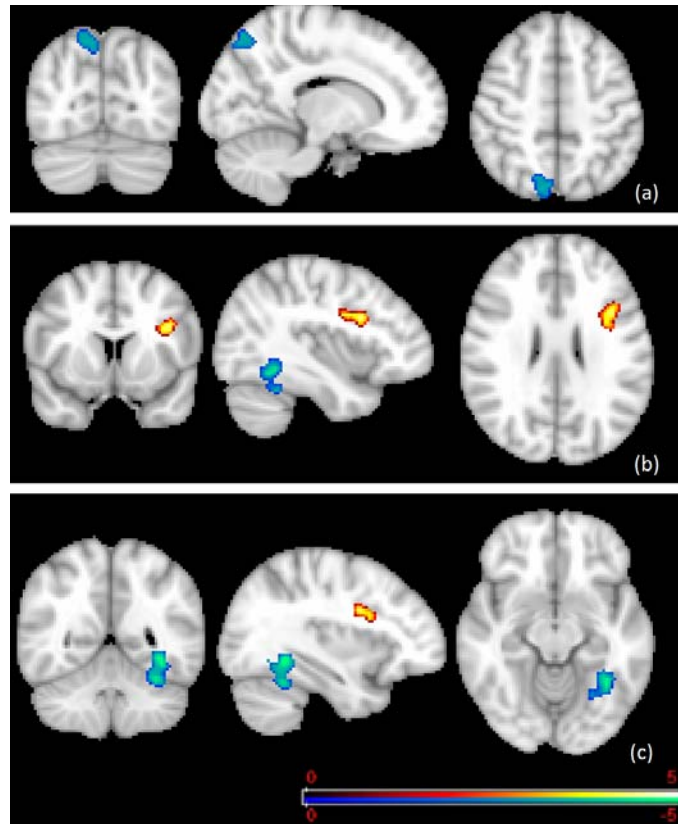


Figure 10. Two-sample t-test ($p=0.01$) for the hippocampus correlation map: The cold color labels the region that the patients group has more correlation with the hippocampus while hot color labels the region that the healthy group has more correlation. In (a) cross bar located on BA, in (b) cross bar located on BA 48, and in (c) cross bar located on the fusiform gyrus.

We could not find any statistical significant correlation between the neurocognitive tests, delayed recall and SAC score, and any of statistical analysis results. The largest correlation value (0.42) was found in the seed point analysis for PCC correlation map between the mean of the correlation value of the dorsal anterior cingulate and delay recall test.

g) Develop susceptibility weighted imaging and mapping (SWIM) results to quantify the amount of iron in microbleeds, to monitor any changes (evolution) of the microbleed over time and to monitor oxygen saturation compared to normal volunteers.

We have had a very successful two years in enhancing the ability of SWIM to quantify iron in the brain. Our work has appeared in numerous papers listed at the end of this report and one of our data sets for both SWI and SWIM was used as an image on the front cover of the book: *Cerebral Microbleeds: Pathophysiology to Clinical Practice*, edited by David Werring, published 2012.

The main efforts we have had in this direction has been to understand how to best reproduce quantitative susceptibility maps given the ill-posedness of the solution using a single orientation acquisition approach. To address the questions of microbleeds, we published a paper on “*Quantitative susceptibility mapping of small objects using volume constraints*” (see ref. 1 below) where we showed that even though absolute susceptibility may be inaccessible for small bleeds, the magnetic moment could in fact be well calculated.

We followed this work up with a new iterative approach to QSM or SWIM as we call it that helped to correct for some of the current weaknesses of the methods. This paper was entitled: *“Improving susceptibility mapping using a threshold-based k-space/image domain iterative reconstruction approach”* (see ref. 2 below). This method was designed specifically to help detect changes in oxygen saturation that might in the future be used to estimate perfusion deficit in mTBI. Although we have not done this study yet, *we believe that this is a very important direction for future research and clinical care in mTBI*. We also published a chapter related to mTBI, imaging veins, SWIM and perfusion entitled: *“The Presence of Venous Damage and Microbleeds in Traumatic Brain Injury and the Potential Future Role of Angiographic and Perfusion Magnetic Resonance Imaging”* (see ref. 7 below).

Still, there are practical issues in getting the right phase information and getting it unwrapped rapidly. To address this issue we studied a multi-echo approach to doing phase unwrapping and doing it on a pixel-by-pixel basis so that it would be rapid and robust. This led to another paper: *“Catalytic multiecho phase unwrapping scheme (CAMPUS) in multiecho gradient echo imaging: Removing phase wraps on a voxel-by-voxel basis.”*(see ref. 6 below). Although this technique used 11 echoes, we are now trying to accomplish this with two echoes instead.

Once we have a good working SWIM dataset, it becomes possible to do something that leads to a new type of SWI dataset, what we refer to as “True SWI” that uses the susceptibility map to create a mask that does not suffer from orientation effects on the phase and is a local mask again not suffering from non-local field or phase effects. This has been tentatively accepted for publication and is entitled: *“True susceptibility weighted imaging. Tentatively accepted in J Magn Reson Imaging.”* (see ref. 1 in the under preparation section).

Imaging iron and even mapping iron is now possible with MRI. Our approach is straight forward and our reconstruction is rapid thanks to the iterative method we propose. However, knowing exactly how SWIM data corresponds with actual iron is more difficult. Along these lines, we did a comparison of MRI with XRF and published the following paper: *“Measuring iron in the brain using quantitative susceptibility mapping and X-ray fluorescence imaging.”* (see ref. 3 below).

Imaging veins and microbleeds is important but there is more to the story than just veins in the vasculature. For more severe impacts, the arterial system may well be compromised as well. In that case, we want to be able to image the vasculature as well as possible, and that can now be done with or without a contrast agent using our double echo SWI sequence as shown in: *“Noncontrast-enhanced magnetic resonance angiography and venography imaging with enhanced angiography.”*

Finally, bring together other aspects of imaging along with detection of hemorrhage and the need for neuroradiologists to be involved, we looked at combining DTI with SWI and other conventional imaging. Here we published the paper: *“Detection of hemorrhagic and axonal pathology in mild traumatic brain injury using advanced MRI: implications for neurorehabilitation.”*

In summary, we have created an entirely new foundation for studying mTBI using SWI and SWIM and in combining these with DTI and hopefully in the future with perfusion imaging. It is our hope that this will lead to not only better diagnosis but hope for better treatment for patients.

KEY RESEARCH ACCOMPLISHMENTS

The following accomplishments have been made in the past year:

- Recruitment and follow up of patients and controls. Now we are in the fast lane of scanning subjects on average 4+ scans each week. With the approval of a no-cost extension, we are very confident of recruiting total 50 patients and 50 controls as our original proposal.
- Analysis of preliminary data. Our data demonstrated that, in addition to an increased blood flow as an early response of mild TBI patients, patients' resting functional connectivity tends to increase as well.
- Blood biomarker GFAP levels significantly increased in intracranial cases. This implies a screening tool of biomarker might be able to serve for MRI identification.
- DTI abnormalities account for patients' neurocognitive symptoms at the acute stage.

REPORTABLE OUTCOMES

Papers in preparation based on the material discussed above. Note that in this section and the next section that an asterisk means that the paper has referenced the support of this award as will future papers.

- a) *S. Liu, K. Mok, J Neelavalli, YC Cheng, J. Tang, Y. Ye and E.M. Haacke, True susceptibility weighted imaging. Tentatively accepted in J Magn Reson Imaging.
- b) *Zhifeng Kou, Ramtilak Gattu, Firas Kobeissy, Robert Welch, Brian O'Neil, John Woodard, Sayed Imran Ayaz, Andrew Kulek, Robert Kas'shamoun, Valerie Mika, Conor Zuk, E Mark Haacke, Ronald Hayes, Francesco Tomasello, Stefania Mondello. Combining Biochemical and Imaging Markers to Improve Diagnosis and Characterization of Mild Traumatic Brain Injury in the Acute Setting: Results from a Pilot Study. Submitted to PLoS ONE, in review.
- c) Z. Kou et al, another paper on resting state fMRI is also in preparation for submission.

Papers and book chapters:

- 1) *S. Liu, J. Neelavalli, Y.-C. N. Cheng, J. Tang, and E. M. Haacke, *Quantitative susceptibility mapping of small objects using volume constraints*, Magn. Reson. in Med., vol. 69, no. 3, pp. 716-723, 2013.
- 2) *J. Tang, S. Liu, J. Neelavalli, Y.-C. N. Cheng, S. Buch, and E. M. Haacke, *Improving susceptibility mapping using a threshold-based k-space/image domain iterative reconstruction approach*, Magn. Reson. in Med., vol. 69, no. 5, pp. 1396-1407, 2013.
- 3) W. Zheng, H. Nichol, YC Cheng, EM Haacke. *Measuring iron in the brain using quantitative susceptibility mapping and X-ray fluorescence imaging*. Neuroimage, Sep;78:68-74, 2013.
- 4) *Y. Ye, J. Hu, D. Wu, E.M. Haacke. *Noncontrast-enhanced magnetic resonance angiography and venography imaging with enhanced angiography*. J Magn Reson Imaging. [Epub ahead of print] 2013.
- 5) Benson RR, Gattu R, Sewick B, Kou Z, Zakariah N, Cavanaugh JM, Haacke EM. *Detection of hemorrhagic and axonal pathology in mild traumatic brain injury using advanced MRI: implications for neurorehabilitation*. NeuroRehabilitation. 2012;31(3):261-79. doi: 10.3233/NRE-2012-0795.
- 6) Feng W, Neelavalli J, Haacke EM. *Catalytic multiecho phase unwrapping scheme (CAMPUS) in multiecho gradient echo imaging: Removing phase wraps on a voxel-by-voxel basis*. Magn Reson Med. 70(1):117-26, 2013.
- 7) E.M. Haacke, W. Raza, W. Bo and Z. Kou. *The Presence of Venous Damage and Microbleeds in Traumatic Brain Injury and the Potential Future Role of Angiographic and Perfusion Magnetic Resonance Imaging in Cerebral Blood Flow, Metabolism, and Head Trauma: The Pathotrajjectory of Traumatic Brain Injury*, Chapter 4, editors C. W. Kreipke and J. A. Rafols, Springer, 2012.

Presentations:

Our group has given a number of presentations in national and international meetings. Over and above those already quoted for 2011 and 2012 in the previous annual report, these include:

2013 presentations

Jie Yang, Zhifeng Kou, Robert Dean Welch, Randall Benson, Ramtilak Gattu, Valerie Mika, and E. Mark Haacke. Neuroimaging biomarkers of mild traumatic brain injury (mTBI) and its recovery: A preliminary study in acute setting 30pm. 21st Annual ISMRM Salt Lake City, 2013. Electronic poster 3561.

E. Mark Haacke and Zhifeng Kou. "Development of MRI Biomarkers for Improved Diagnosis of TBI" Mon, 5/13 in the Session "Future of Human Assisted Devices Impacting TBI Rehabilitation". 10th Annual Society for Brain Mapping and Therapy, Baltimore, 2013.

Zhifeng Kou, Neuroimaging of mild traumatic brain injury at the acute stage. Invited talk. Penn State University Brain Concussion Workshop, Oct. 2012.

Grants, Honors and Awards

A major award (Seed Grant Award) was received by Dr. Zhifeng Kou from the International Society for Magnetic Resonance in Medicine (ISMRM) to investigate the relationship between MR imaging and blood biomarkers in acute detection and outcome prediction of mTBI.

CONCLUSION

During the last year we have made major progress in collecting the data on both mTBI patients and normal controls. We have demonstrated already in this group the value of SWI and DTI and potential correlations with neuro-psychological testing. This extension year will allow us to both complete collection of the data and answer a number of key questions in the quest for better diagnosis and understanding of the pathophysiology in mTBI patients.

PLOS ONE

Combining Biochemical and Imaging Markers to Improve Diagnosis and Characterization of Mild Traumatic Brain Injury in the Acute Setting: Results from a Pilot Study

--Manuscript Draft--

Manuscript Number:	
Article Type:	Research Article
Full Title:	Combining Biochemical and Imaging Markers to Improve Diagnosis and Characterization of Mild Traumatic Brain Injury in the Acute Setting: Results from a Pilot Study
Short Title:	Biochemical and Imaging Markers of mTBI
Corresponding Author:	Zhifeng Kou, Ph.D. Wayne State University Detroit, MI UNITED STATES
Keywords:	traumatic Brain Injury (TBI); mild traumatic brain injury (mTBI); biomarkers; magnetic resonance imaging (MRI); neuroimaging; UCH-L1; GFAP; susceptibility weighted imaging (SWI); diffusion tensor imaging (DTI)
Abstract:	<p>Background: Mild traumatic brain injury (mTBI) is a significant public healthcare burden and its diagnosis remains a challenge in emergency department. Serum blood biomarker-based tests and advanced magnetic resonance imaging (MRI) techniques have already demonstrated their potentials to improve brain injury detection even in patients with negative computed tomography (CT) finding. The objective of this study was to determine the clinical value of a combinational use of both blood biomarkers and MRI in mTBI detection and characterization in the acute setting (within 24 hours after injury).</p> <p>Methods: Nine patients with mTBI were prospectively recruited from the emergency department. Serum samples were collected at the time of hospital admission and every 6 hours up to 24 hours post injury. Neuronal (Ubiquitin C-terminal Hydrolase-L1 [UCH-L1]) and glial (glial fibrillary acidic protein [GFAP]) biomarker levels were analyzed. Advanced MRI data were acquired at 9±6.91 hours after injury. Patients' neurocognitive status was assessed by using the Standard Assessment of Concussion (SAC) instrument.</p> <p>Results: The median serum levels of UCH-L1 and GFAP on admission were increased 4.9 folds and 10.6 folds, respectively, compared to reference values. Three patients were found with intracranial hemorrhages on SWI, and they all had very high GFAP levels. Total volume of brain white matter (WM) with abnormal diffusion tensor imaging (DTI) fractional anisotropy (FA) measures were negatively correlated with patients' SAC scores, including memory. Both increased and decreased DTI-FA values were observed in the same subjects. Serum biomarker level was not correlated with patients' DTI data nor SAC score.</p> <p>Conclusions: Blood biomarkers and advanced MRI may correlate or complement each other in different aspects in mTBI detection and characterization. GFAP might have potential to serve as a clinical screening tool for intracranial bleeding. UCH-L1 complements MRI in injury detection. The patients' neurocognitive symptoms were accounted by impairment at WM tracts.</p>
Order of Authors:	<div>Zhifeng Kou, Ph.D.</div> <div>Ramtilak Gattu</div> <div>Firas Kobeissy</div> <div>Robert Welch</div> <div>Brian O'Neil</div> <div>John Woodard</div> <div>Sayed Imran Ayaz</div> <div>Andrew Kulek</div> <div>Robert Kas'shamoun</div>

	Valerie Mika
	Conor Zuk
	Ewart Mark Haacke
	Ronald Hayes
	Francesco Tomasello
	Stefania Mondello
Suggested Reviewers:	<p>Samuel Slobonov, Ph.D. Professor, Penn State University sms18@psu.edu The reviewer is an expert in mild traumatic brain injury research. He also serves as the director of the Center for Sport Concussion Research and Service. He will be well qualified and suitable to review our work.</p>
	<p>Quan Jiang, Ph.D. Senior Staff Investigator, Henry Ford Hospital QJIANG1@hfhs.org The reviewer is an expert in neuroimaging of traumatic brain injury and stroke study. He is a well established investigator in this field. He is well qualified for reviewing our work.</p>
Opposed Reviewers:	

Table of Contents

	<u>Page</u>
Introduction.....	(
Body.....)
Key Research Accomplishments.....	1'
Reportable Outcomes.....	%
Conclusion.....	14
Appendices.....	Attachment

The views, opinions and/or findings contained in this report are those of the author(s) and should not be construed as an official Department of the Army position, policy or decision unless so designated by other documentation.

**Combining Biochemical and Imaging Markers to Improve Diagnosis and
Characterization of Mild Traumatic Brain Injury in the Acute Setting: Results from
a Pilot Study**

Zhifeng Kou ^{1,2}, Ramtilak Gattu ², Firas Kobeissy ³, Robert Welch ⁴, Brian O'Neil ⁴, John
Woodard ⁵, Sayed Imran Ayaz ⁴, Andrew Kulek ⁴, Robert Kas'shamoun ⁴, Valerie Mika ⁴,
Conor Zuk ², E Mark Haacke ^{1,2}, Ronald Hayes ⁶, Francesco Tomasello ⁷, Stefania
Mondello ⁷

¹Department of Biomedical Engineering,

²Department of Radiology,

⁴Department of Emergency Medicine,

⁵Department of Psychology

School of Medicine, Wayne State University, Detroit, MI, USA;

³Center for Neuroproteomics and Biomarkers Research, Department of Psychiatry,
McKnight Brain Institute, University of Florida, Gainesville, FL, USA;

⁶ Banyan Biomarkers, Inc., Alachua, FL, USA;

⁷ Department of Neurosciences, University of Messina, Messina, Italy.

1 **Key Words:** traumatic Brain Injury (TBI), mild traumatic brain injury (mTBI), biomarkers,
2 magnetic resonance imaging (MRI), neuroimaging, UCH-L1, GFAP, susceptibility
3 weighted imaging (SWI), and diffusion tensor imaging (DTI).

4

5 **Correspondence please address to:**

6 Zhifeng Kou, Ph.D., Assistant Professor

7 Departments of Biomedical Engineering and Radiology

8 Wayne State University, Detroit, MI 48201

9 Email: zhifeng.kou@gmail.com

10

1 **Abstract**

2 **Background:** Mild traumatic brain injury (mTBI) is a significant public healthcare burden
3 and its diagnosis remains a challenge in emergency department. Serum blood
4 biomarker-based tests and advanced magnetic resonance imaging (MRI) techniques
5 have already demonstrated their potentials to improve brain injury detection even in
6 patients with negative computed tomography (CT) finding. The objective of this study
7 was to determine the clinical value of a combinational use of both blood biomarkers and
8 MRI in mTBI detection and characterization in the acute setting (within 24 hours after
9 injury).

10 **Methods:** Nine patients with mTBI were prospectively recruited from the emergency
11 department. Serum samples were collected at the time of hospital admission and every
12 6 hours up to 24 hours post injury. Neuronal (Ubiquitin C-terminal Hydrolase-L1 [UCH-
13 L1]) and glial (glial fibrillary acidic protein [GFAP]) biomarker levels were analyzed.
14 Advanced MRI data were acquired at 9 ± 6.91 hours after injury. Patients' neurocognitive
15 status was assessed by using the Standard Assessment of Concussion (SAC)
16 instrument.

17 **Results:** The median serum levels of UCH-L1 and GFAP on admission were increased
18 4.9 folds and 10.6 folds, respectively, compared to reference values. Three patients
19 were found with intracranial hemorrhages on SWI, and they all had very high GFAP
20 levels. Total volume of brain white matter (WM) with abnormal diffusion tensor imaging
21 (DTI) fractional anisotropy (FA) measures were negatively correlated with patients' SAC
22 scores, including memory. Both increased and decreased DTI-FA values were observed
23 in the same subjects. Serum biomarker level was not correlated with patients' DTI data
24 nor SAC score.

25 **Conclusions:** Blood biomarkers and advanced MRI may correlate or complement each
26 other in different aspects in mTBI detection and characterization. GFAP might have

1 potential to serve as a clinical screening tool for intracranial bleeding. UCH-L1
2 complements MRI in injury detection. The patients' neurocognitive symptoms were
3 accounted by impairment at WM tracts.

4

5

6

1 INTRODUCTION

2 Traumatic brain injury (TBI) is a significant public healthcare burden in the United States.
3 It accounts for 1.7 million incidents in the United States each year [1, 2]. Most TBI
4 patients belong to mild TBI (mTBI) severity due to the improvement of motor vehicle
5 safety design in recent years [3]. mTBI has over 1 million emergency visits in the United
6 States each year [4]. It causes a constellation of physical, cognitive, and emotional
7 symptoms that significantly impact the patients' quality of life, and costs the nation \$16.7
8 billion each year [3, 5, 6]. To date, most mTBI patients stay in the emergency
9 department (ED) for only a few hours and then are discharged home without a concrete
10 follow-up plan. Up to 50% of mTBI patients may develop prolonged neurocognitive
11 problems within one month [7, 8], and 5-15% of them continue to manifest
12 neurocognitive sequelae at one year [7, 9]. Often, their neurocognitive outcomes
13 inconsistently correlate with clinical measures such as the Glasgow Coma Scale (GCS)
14 score and post-traumatic amnesia. Most mTBI patients do not present abnormalities on
15 computed tomography (CT) at admission and conventional magnetic resonance imaging
16 (MRI) [10, 11] in the emergency setting. The immediate challenge for emergency
17 physicians is to identify those CT-negative patients for intracranial abnormalities and
18 long-term neurocognitive symptoms [12].

19

20 Advanced MRI has demonstrated improved sensitivity in detecting TBI pathologies and
21 functional impairments that underlie patients' cognitive symptoms [13, 14]. Examples
22 include diffusion tensor imaging (DTI) of axonal injury [15-24], susceptibility weighted
23 imaging (SWI) of hemorrhagic lesions [25-27], and others. Advanced MRI offers
24 anatomical and pathological information, reflecting brain damage with high spatial
25 resolution [13, 14]. The American College of Emergency Physicians and Center for
26 Disease Control Joint Study Panel highly recommended examining the role of advanced

1 MRI in the acute setting (within 24 hours after injury) [12]. However, to date, very few
2 studies have been designed for scanning mTBI patients within 24 hours after injury when
3 the patients are still in ED. This is mainly due to the high cost of MRI that makes it
4 prohibitive to scan all mTBI patients and the inaccessibility of MRI for 24/7 availability in
5 the acute setting. Consequently, in the majority of medical centers in North America,
6 MRI is not a standard of care of mTBI patients in the acute setting, partially due to the
7 difficulty of reimbursement associated with the high cost of a MRI scan.

8
9 In addition to patient's clinical characteristics and advanced neuroimaging studies,
10 brain-specific proteins released into biofluids after brain injury, as a result of cellular
11 damage and activation, have demonstrated the potential to serve as diagnostic and
12 prognostic markers in mTBI [28, 29]. Along with providing improved diagnostic capability
13 and molecular characterization of subjects who sustained mTBI, appropriate biomarker
14 screening may lead to a more selective strategy for neuroimaging, reducing the need for
15 a substantial number of unnecessary imaging exams. With these aims in mind, recently,
16 several groups reported the application of neuroproteomics to identify and characterize
17 biochemical markers of TBI [30]. Among the variety of blood proteins that have been
18 used to investigate the neuronal marker, Ubiquitin C-terminal Hydrolase-L1 (UCH-L1)
19 [31-33] and the astrocyte-specific protein Glial Fibrillary Acidic Protein (GFAP) [34], and
20 α II-Spectrum Breakdown Products (SBDPs) for axonal injury [35, 36] seem particularly
21 promising.

22
23 UCH-L1 is a small (25 kDa), neuronal protease involved in either the addition or removal
24 of ubiquitin from proteins that are destined for metabolism via the ATP-dependent
25 proteasome pathway; it is highly enriched in the brain (1 – 5% of total soluble brain
26 protein)[37, 38]. Mutations and polymorphisms of UCH-L1 have been associated with

1 familial Parkinson's Disease [39]. UCH-L1 is released into the extracellular space as a
2 consequence of cell destruction under diverse pathological conditions affecting the brain.
3 Previous clinical studies have demonstrated increased UCH-L1 levels in cerebral spinal
4 fluid (CSF) and in serum in severe TBI patients and that the magnitude of this increase
5 correlated with injury severity, CT finding and patient outcome [31, 33]. Recently, a study
6 was completed investigating UCH-L1 in adults with mild and moderate TBI showing
7 increased UCH-L1 levels in mTBI patients compared to uninjured controls and that UCH-
8 L1 was able to detect intracranial lesions on CT with an area under the curve (AUC) of
9 0.73 [40]. Based on these encouraging results and the fact that UCH-L1 is specific to
10 neurons and its high specificity and abundance in the CNS, it appears to be an excellent
11 candidate biomarker for the brain injury clinical studies.

12
13 Compared with UCH-L1, GFAP is a monomeric intermediate filament protein, major
14 constituent of the astroglial cytoskeleton, and highly brain-specific [41, 42]. This glial
15 protein represents an ideal complement of the neuronal UCH-L1, as demonstrated by a
16 recent study showing that the correlations between these 2 markers reflect structural
17 changes detected by neuroimaging and may be used as an indicator for differing
18 intracranial pathologies after brain trauma [43]. Additionally, previous studies evaluating
19 severe TBI patients demonstrated that GFAP concentrations were associated with injury
20 severity and outcome [44, 45]. Recently, in a prospective cohort study of 108 patients
21 with mild or moderate TBI, GFAP was found to be elevated in the serum within 1 h after
22 injury, discerning TBI patients from uninjured controls with an area under the curve
23 (AUC) of 0.90 and discriminating patients with and without intracranial lesion as
24 assessed by CT with an AUC of 0.79 [46].

As a simple biofluid-based rapid diagnostic tool, serum biochemical markers offer great potential for rapid, accurate, and cost-effective diagnosis of brain injury, and a temporal profile of blood protein levels might be indicative of disease progression or resolution. On the other hand, emerging data suggest that MRI and especially advanced MRI techniques are very sensitive in detecting brain injury that are occult in clinical imaging by providing spatial and pathophysiological information. Although the combinational and complementary use of these tools is promising and might have important implications for improving injury detection and outcome prediction, the correlation among injury pathologies at tissue level assessed by neuroimaging and at the protein level as assessed by blood biomarker profiles has not yet been elucidated.

Our objective in this study was to evaluate serum GFAP and UCH-L1 levels after mTBI and their correlation to the advanced MRI findings in a pilot cohort in an acute setting. In particular, we were interested in establishing a serum profile of these biomarkers that might serve as signatures for the presence of brain pathology as assessed by advanced MRI methods, and thus aid in the identification of patients who need an MRI scan in the acute setting.

MATERIALS AND METHODS

Patient Recruitment

This study was approved by both the Human Investigation Committee of Wayne State University and the Institutional Review Board of Detroit Medical Center. Written informed consent was obtained from each subject before enrollment.

A total of 9 patients who sustained mTBI were prospectively recruited from the ED of Detroit Receiving Hospital (DRH), a Level-1 trauma center, which is an affiliated hospital

of Detroit Medical Center (DMC). Patient eligibility was based on the mTBI definition by the American Congress of Rehabilitation Medicine [47] with the following inclusion criteria: Patients aged 18 or older with an initial Glasgow Coma Scale (GCS) score of 13-15 in ED with any period of loss of consciousness less than 30 minutes or any post traumatic amnesia less than 24 hours, or recorded change of mental status (confused, disoriented or dazed). All patients required a CT scan as part of their clinical evaluation. All of them were be able to speak English. The exclusion criteria included patients under the age of 18 years, pregnant woman, medically documented history of brain injury, neurological disorders or psychoactive medications, history of substance abuse, CT indication of any metal in the brain and body, known contraindication to MRI such as a pacemaker or other non-MR compatible implanted device as defined by metal screening procedure, or patients without a clear history of trauma as their primary event (e.g., seizure, epilepsy, etc). In the acute stage, a patient might have mental status change or amnesia in which medical history may not be properly obtained, thus the patient's record was retrospectively screened as well to exclude any patient who does not fit our inclusion criteria. Additionally, we performed an imaging study of 18 healthy controls without history of head injury or antecedents of central nervous system disease.

Neurocognitive Assessments

At the acute setting, once a patient was conscious and stable, they were administered neurocognitive tests and surveyed about their post-concussion symptoms (PCS). Given the situation of emergency care, it is not feasible to perform a full battery of neuropsychological assessment. Instead, a short instrument called Standardized Assessment of Concussion (SAC) [48] was used to assess the patients' neurocognitive status. The SAC instrument was originally developed for onsite testing of subject's neurocognitive performance after sports concussion [49]. It has been reported that SAC

1 is sensitive to the acute changes following concussion and it only requires limited
2 training of an administrator [50]. The SAC assesses 4 cognitive domains including
3 orientation, attention, immediate memory and delayed recall, and the resulting points
4 give a patient score between 0 (indicating greater cognitive deficit) and 30. Previous
5 results report its sensitivity to brain injury in the emergency setting, particularly in that
6 delayed recall is more sensitive to brain injury [50]. The Emergency Room Edition of the
7 SAC instrument also has a graded symptom checklist with all PCS symptoms listed. The
8 patients were asked to grade each symptom from none, mild, moderate, to severe,
9 (graded from a 0 to 3 respectively). The total points were the overall PCS score.

11 **Neuroimaging Protocol**

12 In the ED, once a patient was cleared of any immediate life- threatening risk after a CT
13 scan was completed and was stable enough for an MRI, the patient was transported into
14 the MRI center for imaging scan. All MRI data were collected on a 3-Tesla Siemens
15 Verio scanner with a 32-channel radio frequency head coil. Subjects' head was fixed by
16 a foam pad to restrict motion. Imaging protocol includes SWI, DTI, and resting state
17 functional MRI, in addition to the baseline structural imaging (T1, T2 gradient recalled
18 echo [GRE] and T2 fluid-attenuated inversion recovery [FLAIR]) sequences, with total
19 data acquisition time of 39 min. SWI is a 3-dimensional, T2* based GRE sequence with
20 long TE and 3-D flow compensation. The phase images were high-pass filtered (96x96
21 filter size) by using an in-line manufacture-applied filter and then integrated with
22 magnitude images to generate the processed SWI image to better delineate the spatial
23 relation between microhemorrhages and veins [13, 51]. SWI parameters include TR/TE
24 of 30/20ms, Flip angle of 15 degree, bandwidth of 100 Hz/Px, field of view (FOV) of
25 256x256 mm², imaging matrix of 512x256, 25% oversampling, slice thickness of 2 mm,

total 64 slices, 20% distance factor, GRAPPA iPat factor of 2, with resultant voxel size of 0.5x1x2 mm³ and imaging acquisition time 4m and 18s.

DTI sequence is a standard echo planar imaging (EPI) 2D sequence provided as part of the Siemens package. The parameters include TR/TE of 13300/124 ms, EPI factor of 192, bandwidth of 1240 Hz/Px, FOV of 256x256 mm², imaging matrix of 192x192, slice thickness of 2 mm, total 60 slices, no gap between slices, 30 gradient directions, 2 averages, B values of 0/1000 s/mm², anterior-posterior phase encoding, GRAPPA acceleration factor of 2, with resultant voxel size of 1.3x1.3x2 mm³ and data acquisition time of 14m 26s.

Image Processing and Interpretation

All SWI and DTI images were processed by a co-author who was blinded to the subjects' clinical conditions to avoid any bias. All SWI images were further processed by using our in-house software SPIN (signal processing for NMRI) (MRI Research Institute, Detroit, Michigan). All structural MRI images, including SWI images, were read by two board certified neuroradiologists to identify other conditions that may confound the findings. The neuroradiologists were blinded to the medical history and conditions of subjects to avoid any bias as well. We also graded the structural imaging findings based on their radiologic report for statistical analysis: 0 for negative finding; 1 for non-specific finding, including non-specific WM hyperintensities; and 2 for traumatic hemorrhage.

DTI image processing: Preprocessing of DTI images was carried out by using DTI Studio (<https://www.dtistudio.org>). The preprocessing steps included motion correction and eddy current correction by using automatic image registration (AIR) of all the diffusion weighted images to B0 image as a reference. Fractional Anisotropy (FA) maps

1 were created from the tensor calculations by suppressing the background noise on B0
2 image in DTI Studio. Skull stripping of the B0 image was done by using the BET routine
3 package in Mricro with a fractional intensity of 0.1. A binary mask of the skull-stripped B0
4 image was used on the FA map to preserve the pure brain parenchyma.

5
6 Voxel based analysis (VBA): VBA was performed after the skull stripped FA image was
7 spatially normalized, by using a non-linear algorithm, to the standard FMRIB FA
8 template for all the 27 subjects (9 mTBI patients and 18 healthy controls) in SPM8
9 software

10 (<http://www.fil.ion.ucl.ac.uk/spm/software/spm8/>). A mean FA map and a standard
11 deviation of FA map were created for the controls. A Z-score map was created for each
12 individual patient in a voxel-based approach: For each voxel, the FA difference between
13 each individual patient and the mean of controls was divided by the standard deviation of
14 the controls at the same voxel. Voxels with Z-score > 2 for increased FA and Z-score < -
15 2 for decreased FA were selected after thresholding as abnormal for further
16 consideration.

17
18 Tract based spatial statistics (TBSS): Similar approach was also used to evaluate the
19 lesion load by using TBSS method after registering each subject nonlinearly to the
20 standard FMRIB FA template. TBSS analytical approach was used to compare patient
21 and control groups to evaluate the WM changes after TBI. All the processing steps were
22 performed according to the TBSS manual

23 (<http://fsl.fmrib.ox.ac.uk/fsl/fslwiki/TBSS/UserGuide>). Briefly, every subject's FA image
24 was spatially and non-linearly normalized to a standard FA FMRIB template and
25 transformed into a standard space using FNIRT algorithm from FSL software package.
26 Subsequently, a mean FA image was created from this set of non-linearly transformed

1 images. A search algorithm then created a mean skeleton, looking for the local maxima
2 perpendicular to the WM tract across the whole brain volume in all the transformed
3 images, and then projected this skeleton across all the subjects in the group to extract
4 skeleton of individual subject. Then a voxel-wise permutation-inference analysis was
5 carried out between the skeletons of two groups, and a two tailed t-statistics was
6 performed to extract the voxels that fall below or above a certain threshold. These voxels
7 were converted to a p value based on the threshold set by the t-stat value and the
8 cluster size. Parameters used for the TBSS analysis were a skeleton threshold of 0.3 to
9 eliminate grey matter (GM) voxels or partial volume effects and cluster forming threshold
10 t of 4.

11
12 Masking out non-white matter voxels: The selected abnormal voxels were further filtered
13 to eliminate the GM and the non-WM voxels accounting for the partial volume effects
14 arising from CSF and GM. This filtering was done by segmenting each non- linearly
15 normalized FA map and the mean FA map from the controls into WM, GM and CSF in
16 SPM8 and consequently creating a compound mask by applying a threshold ($p > 0.78$) on
17 these two segmented WM FA images. In this way, we were able to get rid of the false
18 positives arising on the edges of WM because of the mis-registration, and voxels having
19 $FA < 0.3$ were considered to be non WM voxels and discarded by using a mask.
20 Spurious voxels that doesn't form a cluster size of at least 10 voxels were discarded as
21 random noise in VBA and cluster size of less than 5 were discarded as random noise in
22 TBSS. Clusters were extracted using cluster tool in FSL. As a result, the total number of
23 selected voxels was defined as lesion load for each subject in both VBA and TBSS
24 analyses.

26 **Blood Collection and Biomarker Analysis**

All blood samples were collected within 6 hours after injury, upon subject's arrival to ED and then every 6 hours thereafter, until discharge or up to 24 hours. Samples were immediately centrifuged at 4000 rpm for 10 min and frozen and stored at -80°C until the time of analysis. Blinded sample analysis was conducted in a central laboratory (Banyan Biomarkers, Alachua, FL) employing electro-chemiluminescent immunoassay method (ECL-IA) for quantitative analysis of UCH-L1 and GFAP in human serum samples using the MSD platform (MesoScale Discovery, Gaithersburg, MD). The UCH-L1 assay system utilizes a mouse monoclonal IgM anti-human UCH-L1 antibody for solid phase immobilization to capture UCH-L1 from samples. The UCH-L1 antigen in turn binds to a sulfo-tag labeled anti-mouse antibody. The GFAP ECL-IA utilizes a proprietary mouse monoclonal IgG anti-human GFAP antibody for solid phase immobilization and a proprietary polyclonal rabbit antibody for detection. The rabbit IgG polyclonal detection antibody in turn binds to a sulfo-tag labeled anti-rabbit antibody. Detection signal occurs when an electrical current is applied to the electrodes at the bottom of each well of the plate. The signal is measured at 620 nm. Quantitative determination of the biomarker concentration is achieved by comparing the unknown sample signal intensities to a standard curve, obtained from the calibrators run in the same assay. Target concentrations are reported in ng/ml. Each assay plate included 3 QC controls at high, medium and low concentrations of the assay range, each plated in duplicate. Calibrators were prepared in Pooled Human Serum (PHS) matrix. Specifically, a serial dilution of the calibrator protein is prepared and aliquots of that calibrator solution are assayed in the same assay volume and under the same conditions as the samples. The calibrator signal intensities were used to generate a dose response curve and to calculate the sample concentrations using a weighted four parameter logistic function (MSD software and MSD reader). The lower limit of detection of the UCH-L1 and GFAP assays was determined to be 0.10 and 0.008 ng/mL, respectively. Samples with undetectable levels

of UCH-L1 or GFAP were assigned a value of 50% of the lower limit of detection (ie, 0.05 and 0.004 ng/mL, respectively). The median (IQR) serum UCH-L1 and GFAP concentrations determined in blood samples from 29 healthy volunteers using these assays were used as normal reference values (Table 2).

Statistical analysis

Statistical analyses were performed by using SAS version 9.2 (Cary, NC, USA) and R software (<http://www.r-project.org>). Data normality was assessed by using the Kolmogorov–Smirnov test. Results for continuous variables are presented as mean (SD) or median (interquartile range) as appropriate. Frequencies and percentages are presented for categorical variables. Between-group differences were assessed by the Student's t-test (for normally distributed continuous variables) and the Mann–Whitney U test (non-normal continuous variables), Pearson's chi-squared test was used to explore the relationships between categorical variables. Pearson correlations were performed to determine the relationships among different parameters, including imaging, biomarkers and patients neurocognitive measurements. The relationship between biomarker concentration and parameters for TBI severity, neuroimaging and neurocognitive scores was assessed by bivariate correlations (Spearman's). Two sided tests were used and $p < 0.05$ was considered significant.

RESULTS

Characteristics of the Subjects

Individual patient demographic and clinical characteristics are presented in Table 1. In our mTBI cohort ($n = 9$), 8 (89%) subjects were males and 1 (11%) female, the average patient age was 41.22 ± 14.37 (mean \pm standard deviation) years, and all their GCS score were 15 upon ER entrance. Five (55%) patients were injured in assault and 4 (45%)

1 were victims of motor vehicle accidents. The median SAC and PCS scores were 23.5
2 and 15.5, respectively. Two patients presented positive findings in acute CT scan: one
3 with epidural hematoma and cortical contusion in parieto-temporal region and the other
4 with small subarachnoid hemorrhage (SAH). MRI scan were performed at 9 ± 6.91 hours
5 after injury. Three patients, including those two CT positive patients, presented
6 hemorrhagic findings on structural MRI. One of these patients (Case 1) presented small
7 hemorrhages that were completely missed by CT, and another patient was CT positive
8 but missed the intraventricular hemorrhage by CT. In the control population ($n=18$), 61%
9 were men and 39% women, and the average patient age was 34.83 ± 14.30 years. There
10 was no age difference between patient and controls, but a significant gender difference
11 was found between these two groups ($p=0.002$, Chi-square test).

13 **Patients' Neurocognitive Performance**

14 The mean patients' SAC score was $22.75 \pm \text{SD } 2.6$. We compared this mean with
15 published normative data of over 568 subjects [52] (mean \pm SD, 26.3 ± 2.2). The
16 patients' mean SAC score was significantly below this published mean score ($t(8)=-$
17 4.180 , $p=0.0041$). Among each subcategory of SAC test, patients' delayed recall and
18 immediate memory were both significantly lower than published normalized data
19 ($p=0.042$ and $p=0.021$, respectively), and concentration had a trend towards significance
20 ($p=0.056$).

22 **MRI Findings**

23 Both increased and decreased FA beyond the threshold ($t \geq 4$) were found in all patients
24 with variable number of clusters in different locations of the WM. By adding these
25 clusters together, the volume of abnormal FA, called "lesion load", was used to correlate
26 with patients' neurocognitive and biomarker data. DTI "lesion load" with pure increased

FA was found significantly higher than that with pure decreased FA (student t-test, $p=0.034$ for TBSS analysis; and $p=0.017$ for VBA analysis). This suggests the increased FA as the main pathology.

Figure 1 presents the relationship between SAC scores and overall DTI lesion load, which contains total number of voxels with abnormal FA (either increased or decreased). Specifically, SAC scores were found to be inversely correlated with DTI-TBSS lesion load (Pearson $r=-0.883$, $p=0.004$) and DTI-VBA lesion load ($r=-0.796$, $p=0.018$) and had an almost significant correlation with age ($r=-0.701$, $p=0.053$). For subcategory of SAC scores, both DTI-TBSS lesion load and DTI-VBA lesion load were correlated with SAC delayed recall ($r=-0.834$, $p=0.010$ and $r=-0.796$, $p=0.018$, respectively). DTI-TBSS and DTI-VBA lesion loads were strongly correlated (Pearson $r=0.881$, $p=0.002$). There was also a partial correlation of SAC scores with DTI-TBSS and DTI-VBA lesion loads after controlling for age ($r=-0.893$, $p=0.0001$; $r=-0.82$, $p=0.0016$, respectively). There was also a partial correlation of SAC delayed recall with patients' DTI-TBSS and VBA lesion loads, controlling for age ($r=-0.858$, $p=0.001$; $r=-0.811$, $p=0.002$, respectively). Similarly, after controlling for age, DTI-TBSS and DTI-VBA lesion loads remained significantly correlated (Pearson $r=0.853$ and $p=0.001$).

By further investigating the FA increase vs. FA decrease in association with patients' SAC score, the lesion load with pure FA increase was found significantly correlated with patients SAC scores (Pearson $r=-0.87$, $p=0.005$ for TBSS; and $r=-0.86$, $p=0.005$ for VBA) and delayed recall (Pearson $r=-0.79$, $p=0.018$ for TBSS and $r=-0.770$, $p=0.025$ for VBA). In contrast, the lesion volume of pure FA decrease was neither correlated with SAC nor delayed recall (all $p>0.05$ for Pearson correlation).

1 The structural imaging finding, including SWI, was neither correlated with patients' SAC
2 scores nor PCS scores (all $p>0.05$).

3 4 Effect of non-specific MRI findings

5 Given the fact that over half cases have non-specific findings on structural MRI,
6 particularly WM hyperintensities, student T-tests were further performed to see its effect.
7 No group difference was found between cases with non-specific findings and cases
8 without non-specific findings (all with $p>0.3$), in terms of their SAC score, DTI lesion
9 loads (both TBSS and VBA data), and biomarker levels (both UCH-L1 and GFAP).

10 **Serum Concentrations of UCH-L1 and GFAP**

11 Median serum concentrations taken at the time of hospital admission in the patients,
12 within 6 hours after injury, were raised 4.9 folds for UCH-L1, and 10.6 folds for GFAP
13 compared to the laboratory reference values in controls (Table 2 and Figure 2). Serum
14 UCH-L1 concentrations on admission did not correlate with GFAP ($r=-0.24$, $p=0.52$).
15 Serum biomarker concentrations at the time of hospital admission did not correlate with
16 age, time to sample withdrawal, GCS, SAC and PCS score ($p>0.5$). Patients injured in
17 assault had significantly higher UCH-L1 concentrations than patients injured in a MVA
18 (median 0.35 vs 0.10 ng/ml, $p=0.03$) (Figure 3) while GFAP concentrations were not
19 associated with mechanism of injury.

21 Neither UCH-L1 nor GFAP concentrations were associated with structural MRI grading
22 or DTI lesion load, as assessed by Pearson correlation ($p>0.05$). However, patients with
23 hemorrhages on structural MRI presented significantly higher levels of GFAP compared
24 with the non- hemorrhagic group ($p=0.002$) (Table 2 and Figure 3).

1 Temporal profile of biomarker levels indicates that UCH-L1 tend to peak at the
2 admission (within 6 hours after injury) and GFAP at 12 hours after injury. See
3 supplement Figure S1 for details.

4 **Illustrative Cases**

5 *Case 1 - Intraventricular Hemorrhage Missed by CT*

6 A 56-year old male driver suffered mental status change after his car was rear-ended by
7 another vehicle. He presented in the ED with a GCS score of 15 with abrasion and a
8 small laceration on his left eyebrow without closure and left clavicle fracture. His major
9 clinical symptoms were left shoulder pain and headache. Non-contrast CT scan showed
10 no intracranial abnormalities. Initial MRI scanning performed at 20 hours after injury
11 revealed small foci of intraventricular blood on the left side and small blood product in
12 the left lingual gyrus and several nonspecific WM hyperintensities (Figure 4). Graphs
13 displaying time course of UCH-L1 and GFAP are shown in Figure 4. In the sample
14 obtained on admission, GFAP levels were markedly high. GFAP elevation persisted
15 throughout the monitoring time gradually decreasing at 24 hours post injury (median
16 4.610, range 3.241–6.475 ng/ml). In contrast, in the same blood samples, UCH-L1 levels
17 were only slightly higher compared to controls (median 0.098, range 0.055–0.1410
18 ng/ml).

19

20 *Case 2 – Traumatic axonal Injury case with normal structural MRI and high UCH-L1* 21 *level*

22 This 64-year old male patient was a victim of an assault and suffered brief loss of
23 consciousness and femur fracture. He presented in the ED with a GCS score of 15 with
24 symptoms of severe headache, dizziness, not feeling sharp, memory problems, poor

1 concentration, fatigue/sluggish, sadness/depression, and irritability. His SAC score was
2 19 out of 30, and delayed recall 0 out of 5. Non-contrast CT scan showed no intracranial
3 abnormalities. MRI scan performed at 7 hours after injury demonstrated multi-foci of
4 non-specific WM hyper-intensities on FLAIR, but no intracranial bleeding on SWI. DTI
5 data revealed multi-clusters with significantly decreased FA in superior corona radiator,
6 corticospinal tract (see Figure 5), in suggestion of traumatic axonal injury at
7 microstructural level. The results of neurochemical of biomarker time course
8 demonstrated UCH-L1 being consistently elevated ($>0.2\text{ng/ml}$) with high initial values
9 that gradually decreased. GFAP was slightly increased with a peak at 12 hours post-
10 injury (peak 0.063 ng/ml).

11 12 **DISCUSSION**

13 To the best of our knowledge, this is the first effort to combine both blood biomarker and
14 advanced MRI to improve the detection and characterization of mild TBI in the acute
15 setting (within 24 hours after injury). We found that a) the biomarker levels were
16 significantly higher in mTBI patients after injury; b) the levels of GFAP were highest in all
17 subjects with intracranial bleeding on SWI, which is new finding in mTBI research; c) the
18 total volume of WM voxels with abnormal DTI FA measures is correlated with patients'
19 neurocognitive status, including memory; and d) DTI FA values could both increase and
20 decrease at the acute setting, which is also a new finding in mTBI research. In the acute
21 setting, the immediate challenge for emergency physicians is to identify those CT
22 negative but symptomatic patients with intracranial abnormalities that may be predictive
23 of long term neurocognitive sequelae [12]. Given the fact that most mTBI patients stay in
24 the emergency department for a few hours up to 24 hours, our comprehensive approach
25 at this stage, while the patients are still in the emergency department, are more likely to

1 help emergency physicians make decisions on patient's management than examining
2 them days or weeks later.

3
4 This study ideally extends the previous work by our co-authors demonstrating the
5 relationships between different pathways for UCH-L1 and GFAP and different types of
6 brain injury pathophysiology after severe TBI as characterized by CT [53]. In addition to
7 the previous findings, these pilot data suggest that the combined use of biochemical
8 markers and advanced MRI techniques may provide an important tool to evaluate and
9 characterize mTBI patients of importance for the understanding of the different
10 pathophysiological mechanisms following TBI and for the development of effective
11 therapies.

12
13 **The heterogeneity of brain injury pathology.** It is well recognized that brain injury
14 pathology is heterogeneous and complex [54]. Each technique employed in this study
15 brings unique aspects of brain injury pathology and contributes to the whole picture:
16 intracranial bleeding, detected by SWI, manifests blood vessel damage [25]; DTI finding
17 signifies the damage of WM integrity [13, 14]; UCH-L1 for neuronal injury [44, 55]; and
18 GFAP for glial damage [53, 56]. These different pathologies may be correlated with each
19 other and, together, they can cover the spectrum of brain injury that contributes to
20 impaired brain function. Our data demonstrated that intracranial bleeding was associated
21 with elevated GFAP levels, in suggestion of glial injury in association with vascular
22 damage. Meanwhile, the non-association between UCH-L1 and MRI data implies that
23 neuronal injury may not happen together with vascular damage or axonal injury.
24 However, they all demonstrated abnormalities of mTBI in different aspects, in suggestion
25 that they are also complementary to each other for brain injury detection. This further
26 confirms the heterogeneity of brain injury pathology.

Intracranial bleeding and elevated GFAP levels. Searching of intracranial bleeding is critically important in diagnostic radiology. The confirmation of bleeding in mild TBI will automatically categorize a patient into “complicated mild TBI”, who tends to have worse outcome than those without any intracranial bleeding [57]. A most recent study of 135 mTBI patients, scanned at 12 days after injury, demonstrated that one or more brain contusions on MRI, and ≥ 4 foci of hemorrhagic axonal injury on MRI, were each independently associated with poorer 3-month outcome [58]. From pathophysiological perspective, GFAP is a structural protein of astroglial cells that are located in the intracellular space of astrocytes. The damage to astrocytes will cause the release of GFAP into extra-cellular space and that might leak into the blood stream through a compromised blood–brain barrier (BBB) [59]. Furthermore, the end processes of astrocytes surround the endothelial cells of vasculature system and make astrocytes an integral part of neural vascular unit [60]. The damage or temporal opening of the BBB will also likely further damage to the surrounding astrocytes as well. Supporting this, in stroke studies, considerable amount of data demonstrated significantly increase of GFAP in expanding intra-cerebral hemorrhage (ICH) than that in ischemic stroke [61, 62]. Other studies even reported a close correlation between GFAP serum concentration and ICH volume [63, 64]. Even a multi-center clinical trial was conducted to use GFAP to differential ICH from ischemic stroke [63]. Instead of just ICH, our data demonstrated that all intracranial hemorrhage cases, including both extra-axial and parenchymal hemorrhage, have significantly elevated GFAP levels. This implies that GFAP level in blood serum has the potential to serve as a quick screening biomarker to triage mTBI patients for MRI confirmation of intracranial bleeding for an unfavorable outcome prediction.

The role of BBB. The elevated biomarker levels measured in our patients support the idea of a BBB breakdown that has often been documented in patients with TBI even after mild injuries [65]. Indeed, both UCH-L1 and GFAP are CNS-specific proteins with very low concentrations in blood in healthy people, almost below the threshold of detection by using current biomarker technology [40, 46]. The elevated level of either one requires the same pathway to leak into the blood pool: the breakdown of or compromised BBB. Given the much smaller size of UHCL-1 and GFAP than red blood cells, these proteins could more easily get into the blood stream through BBB temporal opening. Consequently, the elevated biomarker levels seem to detect a BBB compromise more relevant than the MRI-detectable bleeding. At micro level, the BBB damage may not be severe enough or the temporal opening of BBB may not be long enough to allow enough red blood cells to pass through or cause sufficient amount of leakage that makes it visible as bleeding on neuroimaging at the macro-level [40]. However, this BBB compromise may be already big enough for sufficient amount of small protein biomarkers leaking into the blood stream and make it detectable in modern biomarker technique. Compared with detectable bleeding, which consists of only a small fraction of mTBI patients, the elevation of CNS-specific proteins in the blood pool might be able to serve as a more sensitive biomarker for the compromise of BBB in mTBI at the acute stage.

Correlation with patients' neurocognitive performance. Our data showed that, DTI lesion loads, both TBSS FA and VBA FA lesion loads, are correlated with their SAC score and delayed recall. More evidence reported that DTI FA values are correlated with mTBI patients' neurocognitive outcome [14, 66]. Particularly, certain regions of DTI WM tract are correlated with patients' specific neurocognitive outcome [14, 66]. As an example, Muhkerjee et al reported that DTI findings are correlated with patients'

neurocognitive performance, but not hemorrhage [67, 68]. Our DTI finding at the acute stage is in the same line as the published result at the sub-acute or chronic stage. This further confirms the hypothesis that there might be microstructural damages or changes in WM tracts that account for patients' neurocognitive deficits. However, this small-scale damage may not reach to the degree of vessel rupture yet that causes bleeding or hemorrhage.

DTI FA increase or decrease. Two more DTI findings in this study are new to the field: a) the co-existence of both increased and decreased FA values in mTBI patients within 24 hours after injury, and b) the dominance of increased FA lesions. All DTI studies of moderate to severe TBI patients [23, 69-71] and subacute/chronic mTBI patients [22, 67, 72-74] report FA *decreases* which are correlated with clinical or neuropsychological measures. However, there are seemingly contradictory findings in mild TBI in the acute stage (within one week after injury) in the literature: Inglese [22] and Arfanakis[21] both reported FA *decreases*, while Wilde [75], Bazarian [76], and Mayer [77] reported FA *increases* and decreased radial diffusivity. Furthermore, Michael Lipton et al [78] reported bi-directional changes (both increase and decrease) of FA in chronic mTBI patients. Of particular note, the terminology "acute stage" could mean quite different timing frames across the studies: some defined it as within 24 hours after injury and some even as within 7 days after injury. To date, only two studies reported MRI scan of mTBI patients within 24 hours after injury and they all have only a handful of patients [21, 75]. The co-existence of both FA decrease and increase within 24 hours after injury is a new finding in the field. It further demonstrates the heterogeneity of mTBI pathology at this stage. Meanwhile, lesion load with increased FA is significantly higher than that with decreased FA. Increased FA lesion load, but not decreased FA lesion load, is correlated with patients' SAC and delayed recall scores in our data. It has been

1 suggested that increased FA *acutely* may reflect cytotoxic oedema [75], which would
2 shunt extracellular fluid into swollen cells. This could have the effect of reducing inter-
3 axonal free water and therefore increasing anisotropy. This demonstrated that cytotoxic
4 edema might be the major pathology that accounts for patients' neurocognitive
5 symptoms at hyper-acute stage (within 24 hours after injury).

6
7 **The need for an axonal injury biomarker.** Our findings confirm that a panel of
8 biomarkers rather than a single analyte seem to have the most utility for the diagnosis of
9 mTBI patients, and improved characterization of the injury. Importantly, in the current
10 study neither UCH-L1 nor GFAP was associated with WM injury identified by DTI. Since
11 the traumatic axonal injury is believed to be a major determinant of functional and
12 neurocognitive symptoms following TBI as demonstrated by the correlation between DTI
13 and patients' neurocognitive deficits, there might be a need for specific axonal injury
14 biomarkers. Further work is needed to develop additional biomarker platforms, including
15 axonal injury markers, in addition to the neuronal and glial damage proteins examined
16 here, and to identify the relationships with advanced MRI techniques and patient
17 outcomes that will help validate and confirm their clinical utilities in the acute setting [12].

18
19 **Limitations and future work.** Despite its encouraging finding, this preliminary work has
20 limitations, including a small sample size and the lack of long-term outcome data.
21 Additional research will be required to validate our current findings in a large cohort of
22 patients with longitudinal follow up and to further determine the relationships between
23 neuroimaging and biomarker findings in the prediction of mTBI outcome.

24
25 **CONCLUSIONS**

1 To summarize, this work represents the first effort of combining both blood protein
2 biomarkers and advanced MRI to improve the detection and characterization of brain
3 injuries after mild TBI in the acute stage (within 24 hours after injury). Our data
4 demonstrate elevated GFAP and UCH-L1 levels in mTBI patients at the acute stage in
5 comparison with controls. Particularly, all cases with intra-cranial hemorrhage had
6 significantly higher GFAP levels than those without hemorrhage. Patients' DTI measures
7 were correlated with their neurocognitive status at this stage. This overlapping and
8 complementary role of blood biomarkers and imaging to brain injury detection offers the
9 promise that they might be used in conjunction in the management of patients with
10 mTBI. Further studies with larger numbers of patients will be required to assess the
11 reproducibility of these findings and to confirm the potential clinical utilities as diagnostic
12 adjuncts in the acute setting.

13
14

1 **Disclosure**

2 Drs. Mondello and Kobeissy were employees and received salaries from Banyan
3 Biomarkers, Inc.; and Dr. Hayes owns stock, receives royalties from, and is an officer of
4 Banyan Biomarkers Inc.

5

6 **Acknowledgement**

7 This work is supported by a Seed Grant awarded to Dr. Zhifeng Kou from the
8 International Society for Magnetic Resonance in Medicine (ISMRM) and a research
9 grant awarded to Dr. E Mark Haacke from the Department of Defense. The authors also
10 acknowledge and appreciate the following members for their contributions: a) the
11 research team (Patrick Medado, Talal Derani and others) of Emergency Medicine of
12 Wayne State University for their screening and recruitment of patients, b) MRI research
13 team (Zahid Latif, R.T., Yang Xuan, B.S., and Bo Wu, B.S.) for their assistance in MRI
14 data acquisition, and c) Banyan Biomarkers Inc., including Dr. Zhiqun Zhang, for their
15 assistance in bioassay analysis.

16

REFERENCES

1. Kay T, *Neuropsychological treatment of mild traumatic brain injury*. Journal of Head Trauma Rehabilitation, 1993. **8**: p. 74-85.
2. National Institutes of Health, *NIH consensus development panel on rehabilitation of persons with traumatic brain injury*. Journal of the American Medical Association (JAMA), 1999. **282**: p. 974-83.
3. CDC, *Report to Congress on Mild Traumatic brain injury in the United States: Steps to Prevent a Serious Public Health Problem*, 2003, Centers for Disease Control and Prevention, National Center for Injury Prevention and Control: Atlanta (GA).
4. Bazarian JJ, McClung J, Cheng YT, Flesher W, Schneider SM, *Emergency department management of mild traumatic brain injury in the USA*. Emergency Medicine Journal, 2005. **22**: p. 473-477.
5. Bazarian JJ, McClung J, Shah MN, Cheng YT, Flesher W, and Kraus J, *Mild traumatic brain injury in the United States, 1998-2000*. Brain Injury, 2005. **19**(2): p. 85-91.
6. Ruff R, *Two decades of advances in understanding of mild traumatic brain injury*. Journal of Head Trauma Rehabilitation, 2005. **20**(1): p. 5-18.
7. Alves W, Macciocchi SN, Barth JT, *Postconcussive symptoms after uncomplicated mild head injury*. J Head Trauma Rehabil, 1993. **8**(3): p. 48-59.
8. Bazarian JJ, Wong T, Harris M, et al, *Epidemiology and predictors of post-concussive syndrome after minor head injury in an emergency population*. Brain Injury, 1999. **13**: p. 173-89.
9. Rimel RW, Giordani B, Barth JT, Boll TJ, Jane JA, *Disability caused by minor head injury*. Neurosurgery, 1981. **9**: p. 221-8.

- 1 10. Belanger HG, Vanderploeg RD, Curtiss G, Warden DL, *Recent neuroimaging*
2 *techniques in mild traumatic brain injury*. J Neuropsychiatry Clin Neurosci., 2007.
3 **19**(1): p. 5-20.
- 4 11. National Academy of Neuropsychology, *Mild Traumatic Brain Injury-An Online*
5 *Course*. 2002, Denver, Co: National Academy of Neuropsychology.
- 6 12. Jagoda AS, Bazarian JJ, Bruns JJ Jr, Cantrill SV, Gean AD, Howard PK, Ghajar
7 J, Riggio S, Wright DW, Wears RL, Bakshy A, Burgess P, Wald MM, Whitson
8 RR; American College of Emergency Physicians; Centers for Disease Control
9 and Prevention, *Clinical policy: neuroimaging and decisionmaking in adult mild*
10 *traumatic brain injury in the acute setting*. Ann Emerg Med, 2008. **52**(6): p. 714-
11 48.
- 12 13. Kou Z, Wu Z, Tong KA, Holshouser B, Benson RR, Hu J, Haacke EM, *The role of*
13 *advanced MR imaging findings as biomarkers of traumatic brain injury*. J Head
14 Trauma Rehabil, 2010. **25**(4): p. 267-82.
- 15 14. Kou Z, B.R., Haacke EM, *Magnetic Resonance Imaging Biomarkers of Mild*
16 *Traumatic Brain Injury*, in *Biomarkers for Traumatic Brain Injury*, e.a. Dambinova
17 S, Editor. 2012, Royal Society of Chemistry.
- 18 15. Shimony JS, McKinstry RC, Akbudak E, Aronovitz JA, Snyder AZ, Lori NF, Cull
19 TS, Conturo TE, *Quantitative diffusion-tensor anisotropy brain MR imaging:*
20 *normative human data and anatomic analysis*. Radiology, 1999. **212**: p. 770-784.
- 21 16. Conturo TE, McKinstry RC, Akbudak E, Robinson BH, *Encoding of anisotropic*
22 *diffusion with tetrahedral gradients: a general mathematical diffusion formalism*
23 *and experimental results*. Magnetic Resonance in Medicine, 1996. **35**: p. 399-
24 412.
- 25 17. Mac Donald CL, Dikranian K, Song SK, Bayly PV, Holtzman DM, Brody DL,
26 *Detection of traumatic axonal injury with diffusion tensor imaging in a mouse*

- 1 *model of traumatic brain injury*. Experimental Neurology, 2007. **205**(2007): p.
2 116–131.
- 3 18. Kou Z, Shen Y, Zakaria N, Kallakuri S, Cavanaugh JM, Yu Y, Hu J, Haacke EM,
4 *Correlation of Fractional Anisotropy with Histology for Diffuse Axonal Injury in a*
5 *Rat Model*, in *Joint Annual Meeting ISMRM-ESMRMB2007*: Berlin, Germany.
- 6 19. Ptak T, Sheridan RL, Rhea JT, Gervasini AA, Yun JH, Curran MA, Borszuk P,
7 Petrovick L, Novelline RA, *Cerebral fractional anisotropy score in trauma*
8 *patients: a new indicator of white matter injury after trauma*. AJR Am J
9 Roentgenol, 2003. **181**: p. 1401-1407.
- 10 20. Huisman TA, Schwamm LH, Schaefer PW, Koroshetz WJ, Shetty-Alva N,
11 Ozsunar Y, Wu O, Sorenson AG, *Diffusion Tensor Imaging as potential*
12 *biomarker of white matter injury in diffuse axonal injury*. AJNR: American Journal
13 of Neuroradiology, 2004. **25**: p. 370-376.
- 14 21. Arfanakis K, Haughton VM, Carew JD, Rogers BP, Dempsey RJ, Meyerand ME,
15 *Diffusion tensor MR imaging in diffuse axonal injury*. Am J Neuroradiol, 2002. **23**:
16 p. 794-802.
- 17 22. Inglese M, Makani S, Johnson G, Cohen BA, Silver JA, Gonen O, Grossman RI,
18 *Diffuse axonal injury in mild traumatic brain injury: a diffusion tensor imaging*
19 *study*. Journal of Neurosurgery, 2005. **103**: p. 298-303.
- 20 23. Benson RR, Meda SA, Vasudevan S, Kou Z, Govindarajan KA, Hanks RA, Millis
21 SR, Makki M, Latif Z, Coplin W, Meythaler J, Haacke EM, *Global white matter*
22 *analysis of diffusion tensor images is predictive of injury severity in TBI*. J
23 Neurotrauma, 2007. **24**(3): p. 446-459.
- 24 24. Mac Donald CL, Johnson AM, Cooper D, Nelson EC, Werner NJ, Shimony JS,
25 Snyder AZ, Raichle ME, Witherow JR, Fang R, Flaherty SF, Brody DL, *Detection*

- 1 *of blast-related traumatic brain injury in U.S. military personnel*. N Engl J Med,
2 2011. **364**(22): p. 2091-100.
- 3 25. Kou Z, Benson RR, Haacke EM, *Susceptibility weighted imaging in traumatic*
4 *brain injury*, in *Clinical MR Neuroimaging, 2nd Edition*, Gillard J, Waldman A,
5 Barker P, Editor. 2010, Cambridge University: Cambridge.
- 6 26. Paterakis K, Karantanas AH, Komnos A, Volikas Z, *Outcome of patients with*
7 *diffuse axonal injury: the significance and prognostic value of MRI in the acute*
8 *phase*. J Trauma, 2000. **49**: p. 1071-1075.
- 9 27. Reichenbach JR, Venkatesan R, Schillinger DJ, Kido DK, Haacke EM, *Small*
10 *vessels in the human brain: MR venography with deoxyhemoglobin as an*
11 *intrinsic contrast agent*. Radiology, 1997. **204**: p. 272–277.
- 12 28. Dash PK, Zhao J, Hergenroeder G, and Moore AN, *Biomarkers for the diagnosis,*
13 *prognosis, and evaluation of treatment efficacy for traumatic brain injury.*
14 *neurotherapeutics*, 2010. **7**: p. 100-114.
- 15 29. Kochanek PM, Berger RP, Bayir H, Wagner AK, Jenkins LW, Clark RS,
16 *Biomarkers of primary and evolving damage in traumatic and ischemic brain*
17 *injury: diagnosis, prognosis, probing mechanisms, and therapeutic decision*
18 *making*. Curr Opin Crit Care, 2008. **14**(2): p. 135-41.
- 19 30. Mondello S, Muller U, Jeromin A, Streeter J, Hayes RL, Wang KK, *Blood-based*
20 *diagnostics of traumatic brain injuries*. Expert Rev Mol Diagn., 2011. **11**(1): p. 65-
21 78.
- 22 31. Mondello S, Akinyi L, Buki A, Robicsek S, Gabrielli A, Tepas J, Papa L, Brophy
23 GM, Tortella F, Hayes RL, Wang KK, *Clinical utility of serum levels of ubiquitin c-*
24 *terminal hydrolase as a biomarker for severe traumatic brain injury*.
25 Neurosurgery, 2011. **Sept 20 [Epub ahead of print]**.

- 1 32. Papa L, Akinyi L, Liu MC, Pineda JA, Tepas JJ 3rd, Oli MW, Zheng W, Robinson
2 G, Robicsek SA, Gabrielli A, Heaton SC, Hannay HJ, Demery JA, Brophy GM,
3 Layon J, Robertson CS, Hayes RL, Wang KK., *Ubiquitin C-terminal hydrolase is*
4 *a novel biomarker in humans for severe traumatic brain injury*. Crit Care Med,
5 2010. **38**(1): p. 138-44.
- 6 33. Mondello S, Papa L, Buki A, Bullock MR, Czeiter E, Tortella FC, Wang KK,
7 Hayes RL, *Neuronal and glial markers are differently associated with computed*
8 *tomography findings and outcome in patients with severe traumatic brain injury: a*
9 *case control study*. Crit Care, 2011. **15**(3): p. R156.
- 10 34. Papa L, Lewis LM, Falk JL, Zhang Z, Silvestri S, Giordano P, Brophy GM,
11 Demery JA, Dixit NK, Ferguson I, Liu MC, Mo J, Akinyi L, Schmid K, Mondello S,
12 Robertson CS, Tortella FC, Hayes RL, Wang KK, *Elevated Levels of Serum Glial*
13 *Fibrillary Acidic Protein Breakdown Products in Mild and Moderate Traumatic*
14 *Brain Injury Are Associated With Intracranial Lesions and Neurosurgical*
15 *Intervention*. Ann Emer Med, 2011. **Nov 8**.
- 16 35. Brophy GM, et al., *alphaII-Spectrin Breakdown Product Cerebrospinal Fluid*
17 *Exposure Metrics Suggest Differences in Cellular Injury Mechanisms after*
18 *Severe Traumatic Brain Injury*. J Neurotrauma, 2009. **26**: p. 471-479.
- 19 36. Mondello S, Robicsek S, Gabrielli A, et al, *all-spectrin breakdown products*
20 *(SBDPs): diagnosis and outcome in severe traumatic brain injury patients*. J
21 Neurotrauma, 2010. **27**(7): p. 1203-13.
- 22 37. Jackson, P. and R.J. Thompson, *The demonstration of new human brain-specific*
23 *proteins by high-resolution two-dimensional polyacrylamide gel electrophoresis*. J
24 Neurol Sci, 1981. **49**(3): p. 429-38.
- 25 38. Saigoh, K., et al., *Intragenic deletion in the gene encoding ubiquitin carboxy-*
26 *terminal hydrolase in gad mice*. Nat Genet, 1999. **23**(1): p. 47-51.

- 1 39. Lincoln, S., et al., *Low frequency of pathogenic mutations in the ubiquitin*
2 *carboxy-terminal hydrolase gene in familial Parkinson's disease*. Neuroreport,
3 1999. **10**(2): p. 427-9.
- 4 40. Papa, L., et al., *Serum levels of ubiquitin C-terminal hydrolase distinguish mild*
5 *traumatic brain injury from trauma controls and are elevated in mild and*
6 *moderate traumatic brain injury patients with intracranial lesions and*
7 *neurosurgical intervention*. J Trauma Acute Care Surg, 2012. **72**(5): p. 1335-
8 1344.
- 9 41. Eng, L.F., et al., *An acidic protein isolated from fibrous astrocytes*. Brain Res,
10 1971. **28**(2): p. 351-4.
- 11 42. Missler, U., et al., *Measurement of glial fibrillary acidic protein in human blood:*
12 *Analytical method and preliminary clinical results*. Clinical Chemistry, 1999.
13 **45**(1): p. 138-141.
- 14 43. Mondello, S., et al., *Glial neuronal ratio: a novel index for differentiating injury*
15 *type in patients with severe traumatic brain injury*. J Neurotrauma, 2012. **29**(6): p.
16 1096-104.
- 17 44. Mondello, S., et al., *Neuronal and glial markers are differently associated with*
18 *computed tomography findings and outcome in patients with severe traumatic*
19 *brain injury: a case control study*. Critical Care, 2011. **15**(3).
- 20 45. Vos, P.E., et al., *GFAP and S100B are biomarkers of traumatic brain injury: an*
21 *observational cohort study*. Neurology, 2010. **75**(20): p. 1786-93.
- 22 46. Papa, L., et al., *Elevated levels of serum glial fibrillary acidic protein breakdown*
23 *products in mild and moderate traumatic brain injury are associated with*
24 *intracranial lesions and neurosurgical intervention*. Ann Emerg Med, 2012. **59**(6):
25 p. 471-83.

- 1 47. American Congress of Rehabilitation Medicine, *Definition of mild traumatic brain*
2 *injury*. J Head Trauma Rehabil, 1993. **8**: p. 86–8.
- 3 48. McCrea M, Randolph C, Kelly JP, *Standardized Assessment of Concussion*
4 *(SAC): Mannual for Administration, Scoring and Interpretation, 2nd ed.* 2000,
5 Waukesha, WI: CNS Inc.
- 6 49. McCrea M, Guskiewicz KM, Marshall SW, Barr W, Randolph C, Cantu RC, et al,
7 *Acute effects and recovery time following concussion in collegiate football*
8 *players: the NCAA Concussion Study*. JAMA, 2003. **290**(19): p. 2556-2563.
- 9 50. Naunheim RS, Matero D, Fucetola R, *Assessment of Patients with Mild*
10 *Concussion in the Emergency Department*. J Head Trauma Rehabil, 2008. **23**(2):
11 p. 116-122.
- 12 51. Haacke, E.M., et al., *Susceptibility weighted imaging (SWI)*. Magnetic Resonance
13 in Medicine, 2004. **52**(3): p. 612-8.
- 14 52. McCrea M, Kelly JP, Randolph C, Kluge J, Bartolic E, Finn G, Baxter B,
15 *Standardized assessment of concussion (SAC): on-site mental status evaluation*
16 *of the athlete*. J Head Trauma Rehabil., 1998. **13**(2): p. 27-35.
- 17 53. Mondello, S., et al., *Neuronal and glial markers are differently associated with*
18 *computed tomography findings and outcome in patients with severe traumatic*
19 *brain injury: a case control study*. Crit Care, 2011. **15**(3): p. R156.
- 20 54. Saatman KE, Duhaime AC, Bullock Ross, Maas AIR, Valadka A, Manley GT, and
21 workshop scientific team and advisory panel members, *Classification of traumatic*
22 *brain injury for targeted therapies*. Journal of Neurotrauma, 2008. **25**: p. 719-738.
- 23 55. Mondello, S., et al., *Clinical utility of serum levels of ubiquitin C-terminal*
24 *hydrolase as a biomarker for severe traumatic brain injury*. Neurosurgery, 2012.
25 **70**(3): p. 666-75.

- 1 56. Vos, P.E., et al., *Glial and neuronal proteins in serum predict outcome after*
2 *severe traumatic brain injury*. Neurology, 2004. **62**(8): p. 1303-10.
- 3 57. Williams DH, Levin HS, Eisenberg HM, *Mild head injury classification*.
4 Neurosurgery, 1990. **217**(3): p. 442–8.
- 5 58. Yuh EL, M.P., Lingsma HF, Yue JK, Ferguson AR, Gordon WA, Valadka AB,
6 Schnyer DM, Okonkwo DO, Maas AI, Manley GT; TRACK-TBI Investigators,
7 *Magnetic resonance imaging improves 3-month outcome prediction in mild*
8 *traumatic brain injury*. Ann Neurol, 2013. **73**(2): p. 224-35.
- 9 59. C, F., *Astroglial proteins as biomarkers of intracerebral hemorrhage*, in
10 *Biomarkers for traumatic brain injury*, e.a. Dambinova S, Editor. 2012, Royal
11 Society of Chemistry: Cambridge, UK.
- 12 60. Neuwelt EA, Bauer B, Fahlke C, Fricker G, Iadecola C, Janigro D, Leybaert L,
13 Molnár Z, O'Donnell ME, Povlishock JT, Saunders NR, Sharp F, Stanimirovic D,
14 Watts RJ, Drewes LR, *Engaging neuroscience to advance translational research*
15 *in brain barrier biology*. Nat Rev Neurosci, 2011. **12**(3): p. 169-82.
- 16 61. Foerch, C., et al., *Serum glial fibrillary acidic protein as a biomarker for*
17 *intracerebral haemorrhage in patients with acute stroke*. J Neurol Neurosurg
18 Psychiatry, 2006. **77**(2): p. 181-4.
- 19 62. Undén J, S.K., Malm J, Campbell E, Rosengren L, Stenflo J, Norrving B, Romner
20 B, Lindgren A, Andsberg G, *Explorative investigation of biomarkers of brain*
21 *damage and coagulation system activation in clinical stroke differentiation*. J
22 Neurol, 2009. **256**(1): p. 72-7.
- 23 63. Foerch C, Niessner M, Back T, Bauerle M, De Marchis GM, Ferbert A, Grehl H,
24 Hamann GF, Jacobs A, Kastrup A, Klimpe S, Palm F, Thomalla G, Worthmann
25 H, Sitzer M; BE FAST Study Group., *Diagnostic accuracy of plasma glial fibrillary*

- 1 *acidic protein for differentiating intracerebral hemorrhage and cerebral ischemia*
2 *in patients with symptoms of acute stroke.* Clin Chem, 2012. **58**(1): p. 237-45.
- 3 64. Foerch C, C.I., Yan B, Dvorak F, Hermans M, Berkefeld J, Raabe A, Neumann-
4 Haefelin T, Steinmetz H, Sitzler M, *Serum glial fibrillary acidic protein as a*
5 *biomarker for intracerebral haemorrhage in patients with acute stroke.* J Neurol
6 Neurosurg Psychiatry, 2006. **77**(2): p. 181-4.
- 7 65. Korn, A., et al., *Focal cortical dysfunction and blood-brain barrier disruption in*
8 *patients with Postconcussion syndrome.* J Clin Neurophysiol, 2005. **22**(1): p. 1-9.
- 9 66. Niogi SN, Mukherjee P, *Diffusion Tensor Imaging of Mild Traumatic Brain Injury.*
10 Journal of Head Trauma Rehabilitation, 2010. **25**(4): p. 241-255.
- 11 67. Niogi SN, Mukherjee P, Ghajar J, Johnson C, Kolster RA, Sarkar R, Lee H,
12 Meeker M, Zimmerman RD, Manley GT, McCandliss BD, *Extent of*
13 *microstructural white matter injury in postconcussive syndrome correlates with*
14 *impaired cognitive reaction time: a 3T diffusion tensor imaging study of mild*
15 *traumatic brain injury.* AJNR Am J Neuroradiol, 2008. **29**(5): p. 967-73.
- 16 68. Niogi SN, Mukherjee P, Ghajar J, Johnson CE, Kolster R, Lee H, Suh M,
17 Zimmerman RD, Manley GT, McCandliss BD., *Structural dissociation of*
18 *attentional control and memory in adults with and without mild traumatic brain*
19 *injury.* Brain, 2008. **131**(12): p. 3209-21.
- 20 69. Newcombe VF, Williams GB, Nortje J, Bradley PG, Harding SG, Smielewski P,
21 Coles JP, Maiya B, Gillard JH, Hutchinson PJ, Pickard JD, Carpenter TA, Menon
22 DK, *Analysis of acute traumatic axonal injury using diffusion tensor imaging.*
23 British Journal of Neurosurgery, 2007. **21**(4): p. 340-8.
- 24 70. Levin HS, Wilde EA, Chu Z, Yallampalli R, Hanten GR, Li X, Chia J, Vasquez
25 AC, Hunter JV, *Diffusion tensor imaging in relation to cognitive and functional*

- 1 *outcome of traumatic brain injury in children*. Journal of Head Trauma
2 Rehabilitation, 2008. **23**(4): p. 197-208.
- 3 71. Kou Z, Gattu R, Benson RR, Raz N, Haacke EM. *Region of Interest Analysis of*
4 *DTI FA Histogram Differentiates Mild Traumatic Brain Injury from Controls*. in
5 *Proceedings of International Society for Magnetic Resonance in Medicine*. 2008.
6 Toronto, Canada.
- 7 72. Wozniak JR, Krach L, Ward E, Mueller BA, Muetzel R, Schnoebelen S, Kiragu A,
8 Lim KO, *Neurocognitive and neuroimaging correlates of pediatric traumatic brain*
9 *injury: a diffusion tensor imaging(DTI) study*. Arch Clin Neuropsychol, 2007.
10 **22**(5): p. 555-68.
- 11 73. Rutgers DR, Fillard P, Paradot G, Tadié M, Lasjaunias P, Ducreux D, *Diffusion*
12 *tensor imaging characteristics of the corpus callosum in mild, moderate, and*
13 *severe traumatic brain injury*. AJNR Am J Neuroradiol, 2008. **29**(9): p. 1730-5.
- 14 74. Kraus MF, Susmaras T, Caughlin BP, Walker CJ, Sweeney JA, Little DM, *White*
15 *matter integrity and cognition in chronic traumatic brain injury: A diffusion tensor*
16 *imaging study*. Brain, 2007. **130**: p. 2508-2519.
- 17 75. Wilde EA, McCauley SR, Hunter JV, Bigler ED, Chu Z, Wang ZJ, Hanten GR,
18 Troyanskaya M, Yallampalli R, Li X, Chia J, Levin HS, *Diffusion tensor imaging of*
19 *acute mild traumatic brain injury in adolescents*. Neurology, 2008. **70**(12): p. 948-
20 55.
- 21 76. Bazarian JJ, Zhong J, Blyth B, Zhu T, Kavcic V, Peterson D, *Diffusion tensor*
22 *imaging detects clinically important axonal damage after mild traumatic brain*
23 *injury: a pilot study*. Journal of Neurotrauma, 2007. **24**(9): p. 1447-59.
- 24 77. Mayer AR, Ling J, Mannell MV, Gasparovic C, Phillips JP, Doezenia D, Reichard
25 R, Yeo RA., *A prospective diffusion tensor imaging study in mild traumatic brain*
26 *injury*. Neurology, 2010. **74**(8): p. 643-50.

- 1 78. Lipton ML, Kim N, Park YK, Hulkower MB, Gardin TM, Shifteh K, Kim M,
2 Zimmerman ME, Lipton RB, Branch CA, *Robust detection of traumatic axonal*
3 *injury in individual mild traumatic brain injury patients: intersubject variation,*
4 *change over time and bidirectional changes in anisotropy.* Brain Imaging Behav.,
5 2012. **6**(2): p. 329-42.

6

7

8

1 **FIGURE LEGENDS**

2 **Figure 1. Correlations between DTI lesion load and patients' neurocognitive data.**

3 As demonstrated in the figures, DTI lesion load (both TBSS and VBA data) are
4 significantly correlated with patients' overall SAC score and delayed recall. R squared
5 values are shown on each figure for linear regression.

6

7 **Figure 2. Dots plots demonstrating UCH-L1 and GFAP concentrations.** Serum

8 UCH-L1 (A) and GFAP (B) concentrations on admission in TBI patients and in controls.

9 Error bars represent median and range. Significant differences are indicated with ** ($P <$

10 0.01) or *** ($P < 0.001$) (Mann–Whitney U-test)

11

12 **Figure 3. Box-and-whisker plots demonstrating UCH-L1 and GFAP concentrations.**

13 (A) Serum UCH-L1 and GFAP concentrations in patients who were victims of assault

14 and in patients injured in a MVA. (B) Serum UCH-L1 and GFAP concentrations in

15 patients with ventricular hemorrhages and hemorrhagic contusions and in patients with

16 non-hemorrhagic lesions. The black horizontal line in each box represents the median,

17 with the boxes representing the interquartile range. Significant differences are indicated *

18 ($P < 0.05$) or ** ($P < 0.01$) (Mann–Whitney U-test).

Figure 4. Case 1. MRI and Biomarker Profile in a Patient with Intraventricular Hemorrhage but Missed by CT. Panels a) and b) are SWI images at different locations of the brain showing intra-ventricular blood and left lingual gyrus blood product (see arrows); panel c) is FLAIR image showing non-specific white matter hyper-intensities (see arrows); panel d) is DTI FA map showing the co-existence of voxels with increased and decreased FA measures (red color means FA decrease and blue color FA increase in comparison with controls, $t > 3$ for t-test); and panel e) is blood biomarker temporal profile, which exhibiting extraordinarily high GFAP levels over time in comparison with controls (median 0.004, interquartile range 0.004-0.015). Despite being missed by CT, the patient case was still detected by both blood biomarker and MRI.

Figure 5. Case 2. MRI and Biomarker Profile in a Patient with traumatic axonal injury but normal appearing structural MRI. Panels a-d) are MRI images at the corpus callosum and fornix level. Panels e-h) are MRI images at the level of superior coronal radiata. Panel i) is blood biomarker profile. FLAIR and SWI images both indicate the skull contusion at the parieto-occipital region (long arrows) but normal appearing brain structure. However, both DTI TBSS and VBA analyses detected significantly reduced FA values at the ipsilateral side (corticospinal tract) and contralateral side (superior corona radiata) of brain white matter (arrow heads), in suggestion of coup and contra coup injury at the microstructure of white matter. Cold color indicates reduced FA values in comparison with controls ($t > 3$ for t-test). Blood biomarkers indicate slightly increased GFAP levels over time but significantly increased UCH-L1 at the admission.

Figure S1. Serum biomarker levels over the first 24 hours after mTBI compared with controls. Serum UCH-L1 (A) levels are maximal early after injury (on admission)

1 (TE=0.24 [0.096-0.346]), while GFAP (B) concentrations peaked 12 hours after injury
2 (0.35 [0.036-2.56]). Error bars represent median and IQR.

3

4

Table 1. Individual demographic and clinical data of the 9 patients enrolled in the study

Patient no.	Age/ Gender	Race	GCS	Mechanism of Injury	SA C	CT	Structural MRI
P-001	56/M	Asian	15	MVA		Negative	Nonspecific WM hyperintensities, Small foci of intraventricular blood on the left. Small blood product in the left lingual gyrus
P-002	36/F	Black	15	MVA	23	Negative	Negative
P-003	19/M	Black	15	MVA	25	Negative	Nonspecific FLAIR hyperintensity in posterior cerebral WM
P-004	35/M	Arabic	15	Assault	26	Positive hemorrhagic contusion on left parieto-temporal lobe	Hemorrhagic contusion on left parieto-temporal lobe, left ventricular hemorrhage
P-005	52/M	Black	15	Assault	19	Negative	Non-specific, multiple scattered discrete foci in cerebral WM
P-006	53/M	Black	15	MVA	24	Negative	Non-specific: Two isolated punctate foci of blood in the right peritrial WM
P-007	39/M	Caucasian	15	assault	22	Small SAH in right Sylvian Fissure	SAH in right Sylvian Fissure
P-008	58/M	Caucasian	15	Assault	19	Negative	Non-specific, super sella lesion, congenital cistern lesion in posterior fossa
P-009	23/M	Caucasian	15	Assault	24	Negative	Negative

Table 2. Serum concentration of UCH-L1 and GFAP in patients with mTBI and in controls. Data are given as median (interquartile range).

		Serum UCH-L1 (ng/mL)	Serum GFAP (ng/mL)
TBI	Admission	0.242 (0.096-0.336)*	0.043 (0.015-0.375)*
	Hemorrhagic	0.164(0.098-0.314)*	0.517(0.239-4.610)** †
	Non-Hemorrhagic	0.171(0.107-0.248)**	0.015(0.015-0.06)**
Controls		0.05 (0.05-0.153)	0.004 (0.004-0.015)

* p <.01 and ** p<.001 (p values of the Mann-Whitney test for differences between the groups [TBI versus Controls])

† p<.01 (p values of the Mann-Whitney test for differences between the groups [Hemorrhagic versus Non-Hemorrhagic])

Figure 1
[Click here to download high resolution image](#)

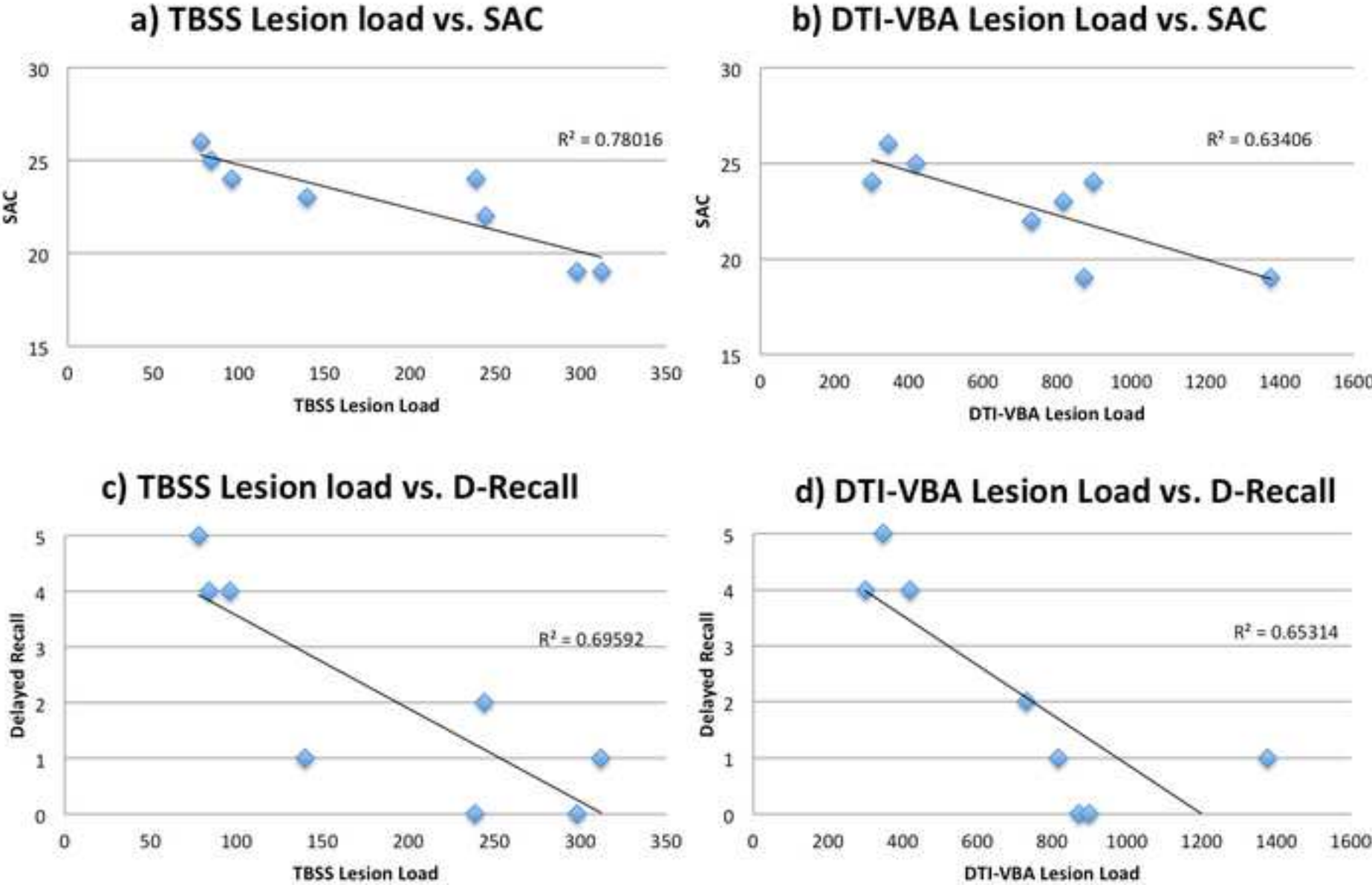


Figure 2
[Click here to download high resolution image](#)

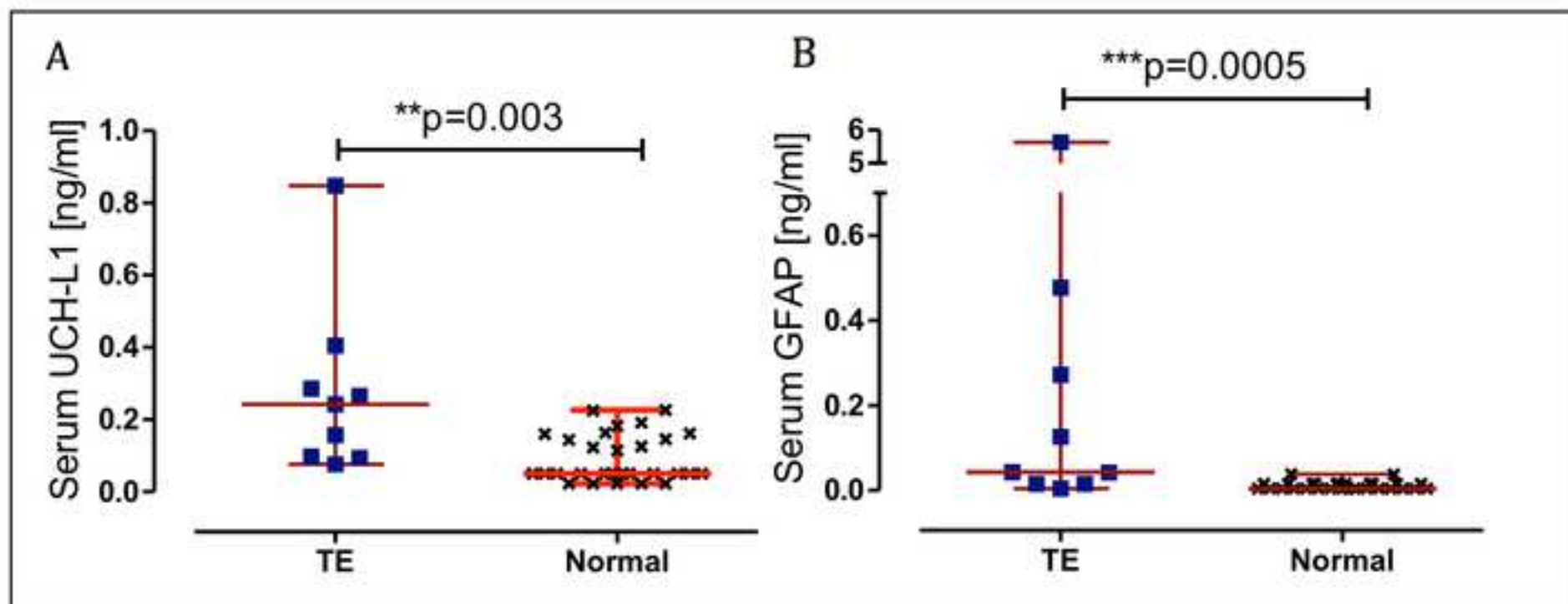


Figure 3
[Click here to download high resolution image](#)

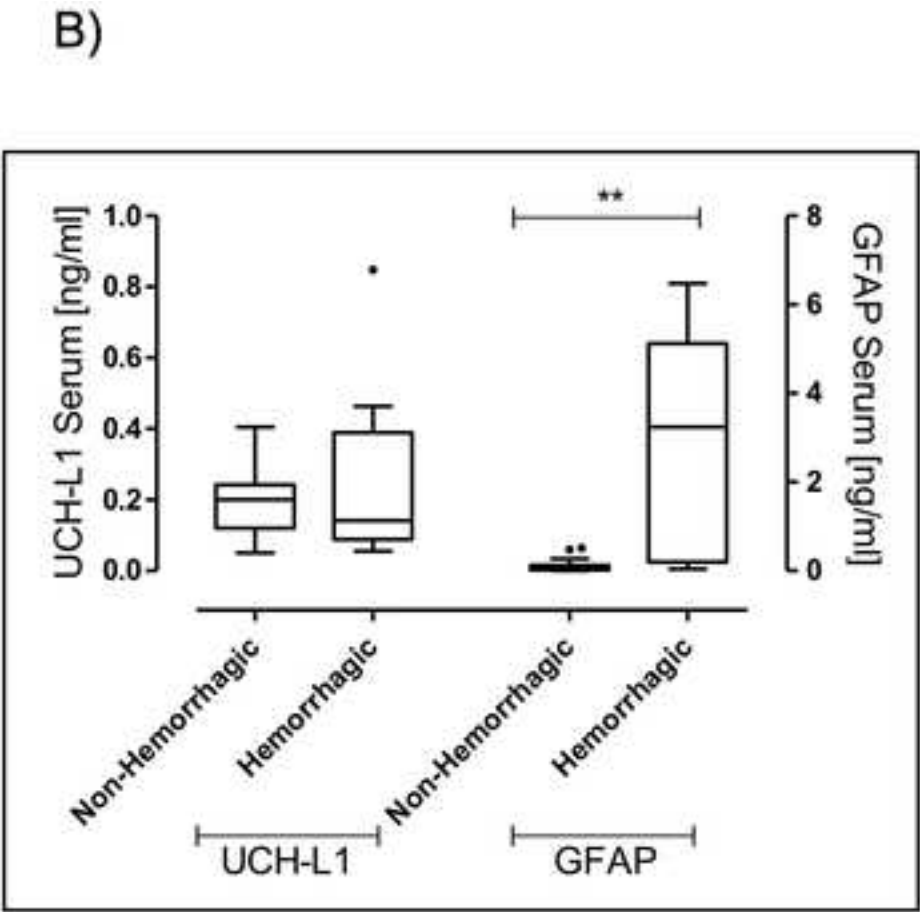
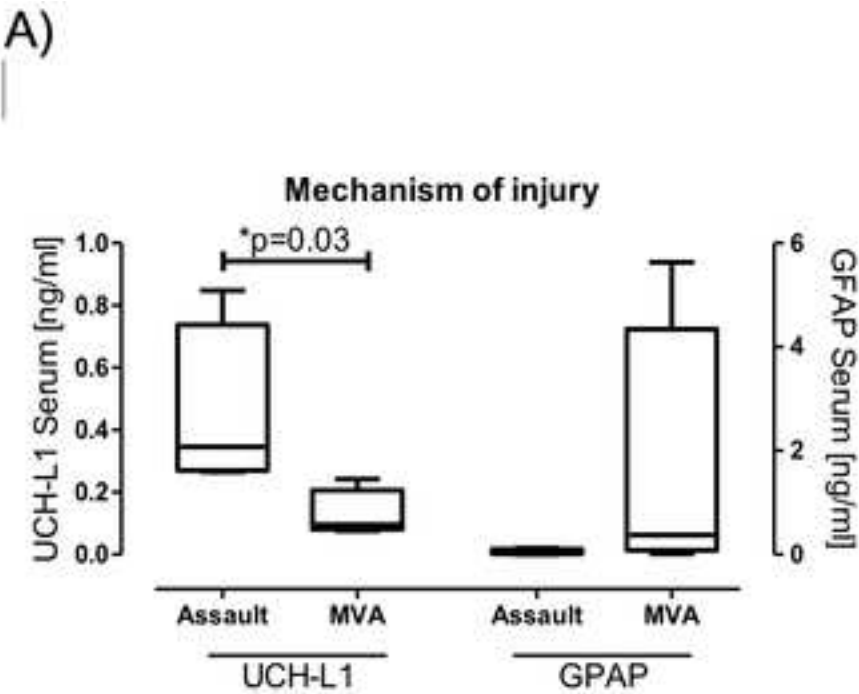


Figure 4
[Click here to download high resolution image](#)

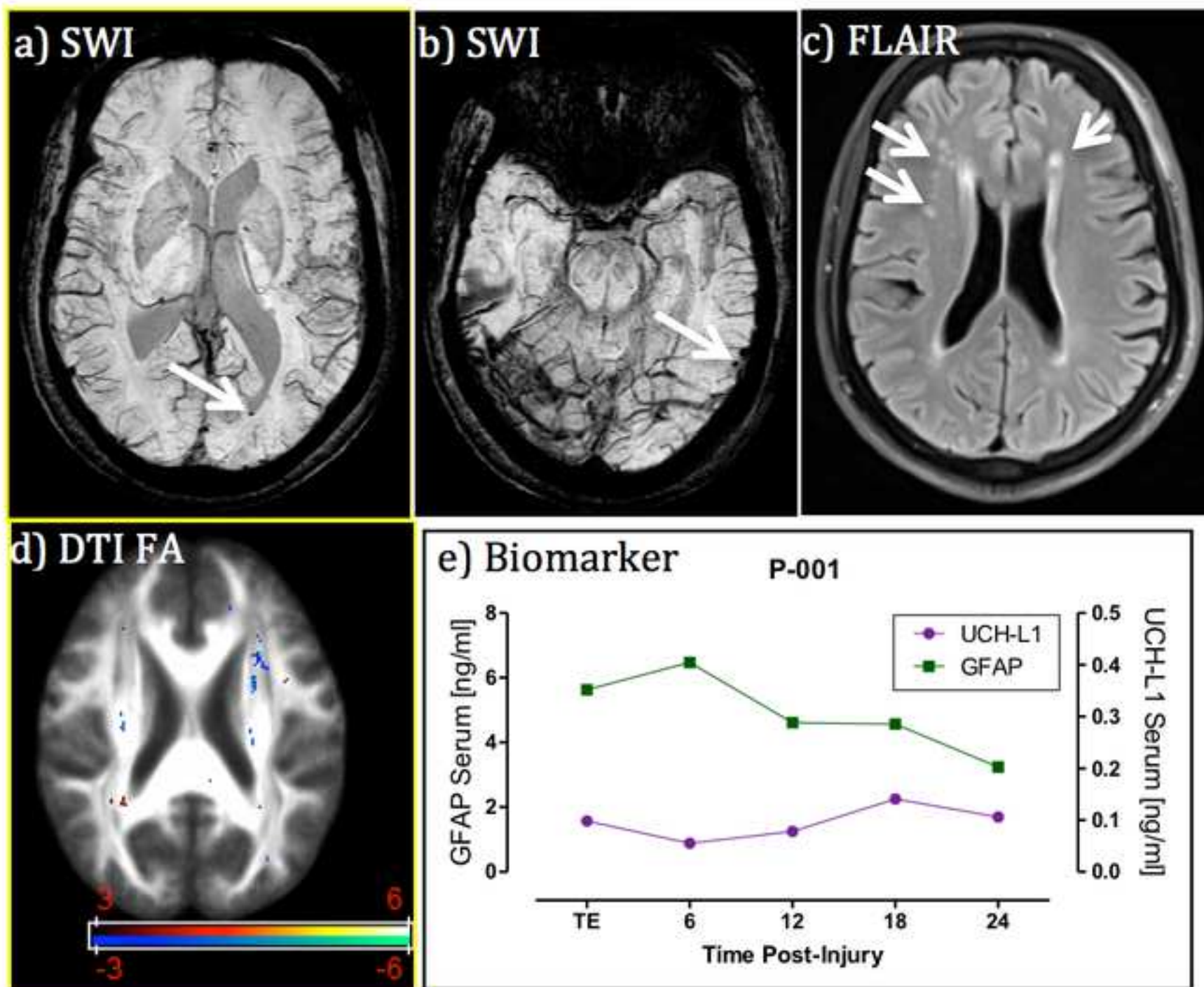


Figure 5
[Click here to download high resolution image](#)

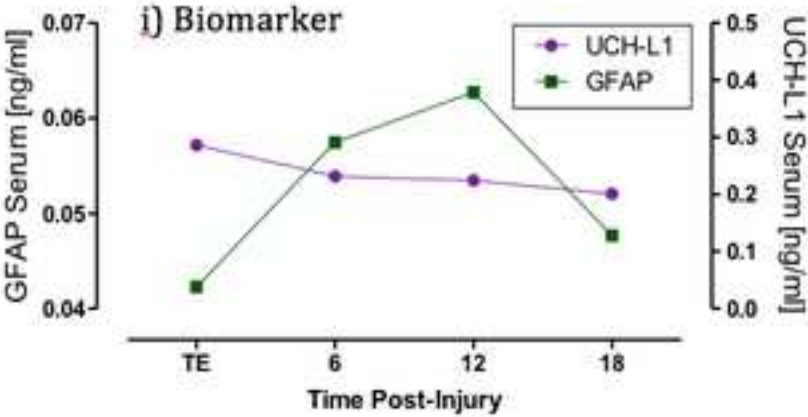
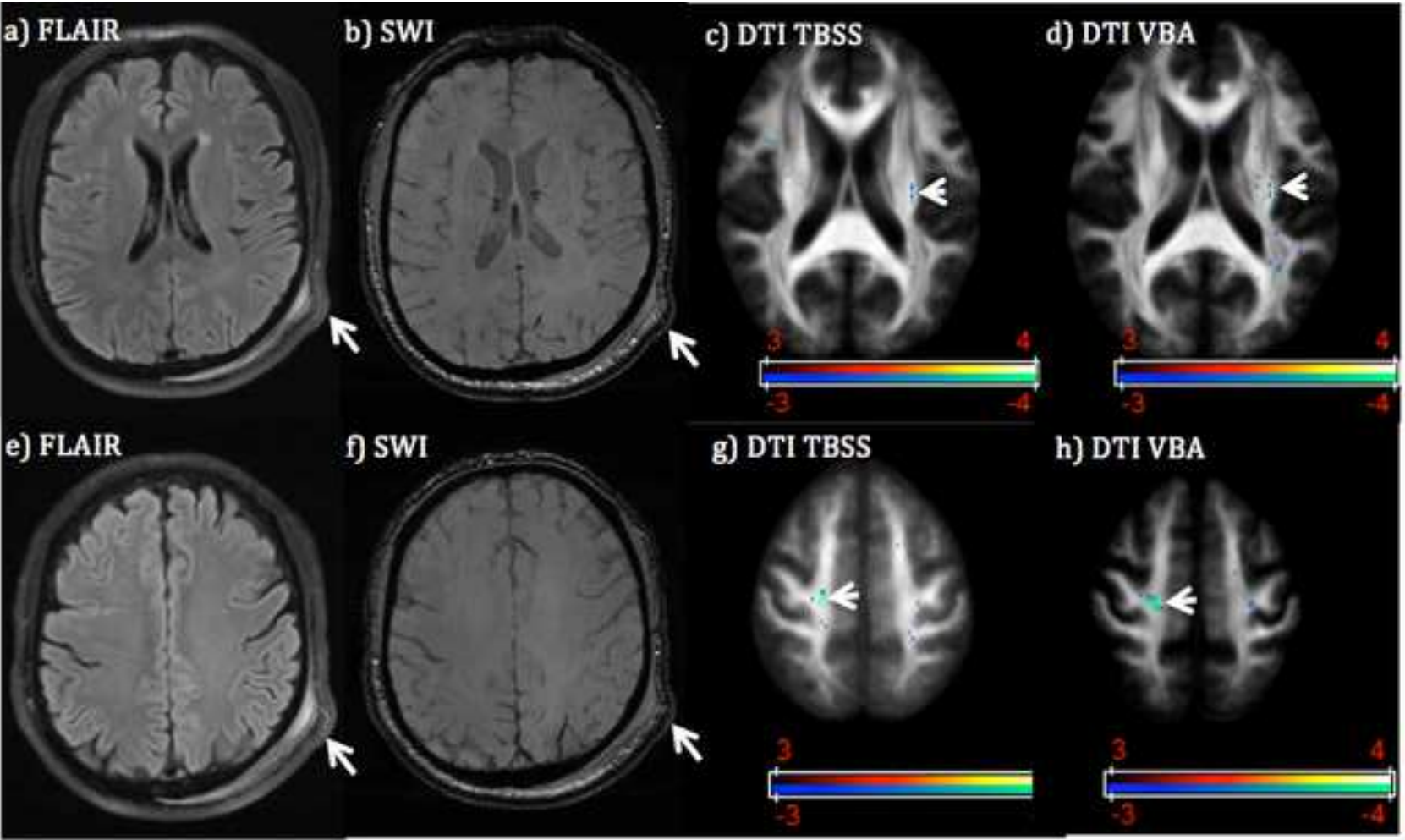
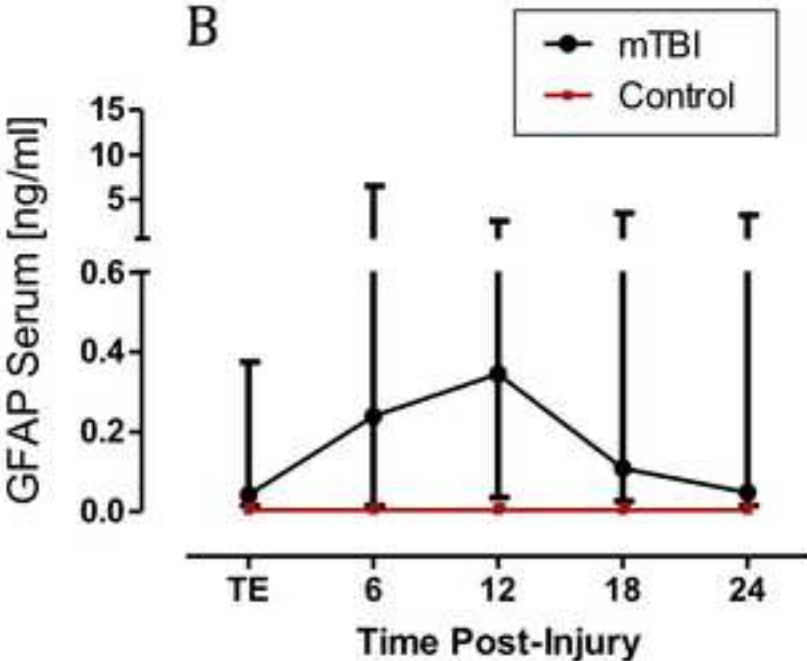
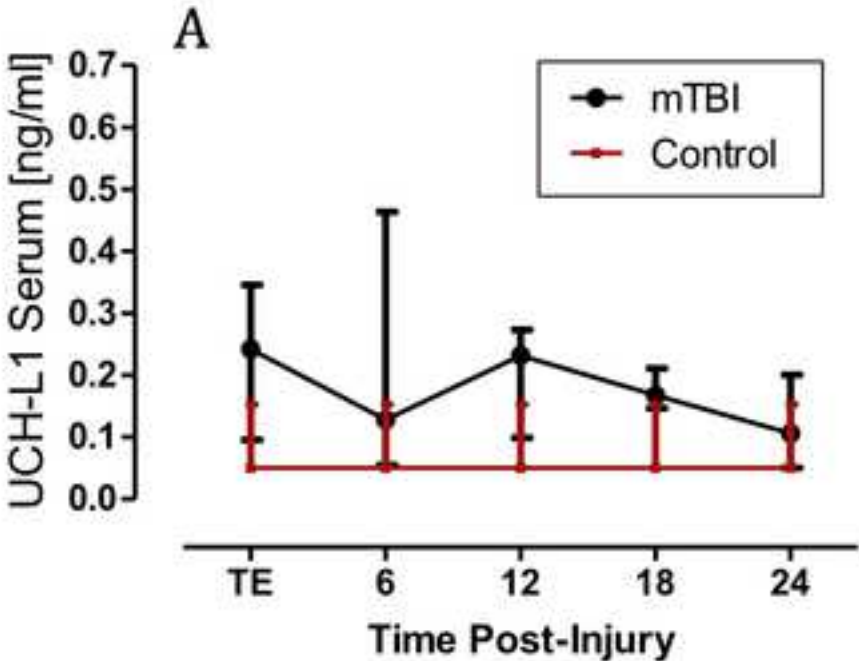


Figure S1
[Click here to download high resolution image](#)



Quantitative Susceptibility Mapping of Small Objects Using Volume Constraints

Saifeng Liu,¹ Jaladhar Neelavalli,^{2*} Yu-Chung N. Cheng,² Jin Tang,¹ and E. Mark Haacke^{1–3}

Microbleeds have been implicated to play a role in many neurovascular and neurodegenerative diseases. The diameter of each microbleed has been used previously as a possible quantitative measure for grading microbleeds. We propose that magnetic susceptibility provides a new quantitative measure of extravasated blood. Recently, a Fourier-based method has been used that allows susceptibility quantification from phase images for any arbitrarily shaped structures. However, when very small objects, such as microbleeds, are considered, the accuracy of this susceptibility mapping method still remains to be evaluated. In this article, air bubbles and glass beads are taken as microbleed surrogates to evaluate the quantitative accuracy of the susceptibility mapping method. We show that when an object occupies only a few voxels, an estimate of the true volume of the object is necessary for accurate susceptibility quantification. Remnant errors in the quantified susceptibilities and their sources are evaluated. We show that quantifying magnetic moment, rather than the susceptibility of these small structures, may be a better and more robust alternative. **Magn Reson Med 69:716–723, 2013. © 2012 Wiley Periodicals, Inc.**

Key words: susceptibility mapping; microbleeds; air bubbles; magnetic moment

The measurement of magnetic susceptibility offers an entirely new form of contrast in magnetic resonance imaging (1–6). More specifically, susceptibility quantification has already found applications in mapping out iron in the form of ferritin in brain tissues such as the basal ganglia (1,4,6) and in the form of deoxyhemoglobin for measuring the oxygen saturation in veins (1,4). This new form of imaging may provide a means for monitoring longitudinal changes in iron content in dementia, multiple sclerosis, traumatic brain injury, and Parkinson's disease. It may also be used to monitor microbleeds which have been implicated in the progression of vascular dementia (7), Alzheimer's, and other neurovascular disorders (8,9).

One of the most recent susceptibility mapping methods is a Fourier-based method (2,3,5,10) which utilizes phase images. The accuracy of such a method depends on the volume measurement of the object. For example, to quantify the susceptibility of a given microbleed, usually the center and the radius of the microbleed have to be determined (10–13). Alternate volume estimations of the microbleed from high-resolution spin echo images may overcome these limitations. With a gradient echo sequence, the apparent volume of the object is increased owing to what is commonly referred to as the “blooming” effect, a signal loss around the object caused by T_2^* dephasing. This increased apparent volume may be used to obtain an estimate of susceptibility while the product of the apparent volume and the estimated susceptibility is much more robust and should still provide a good estimate of the magnetic moment of the object.

The goal of this article is to evaluate the quantitative accuracy of a Fourier-based susceptibility mapping method when it is applied to small structures, and to show that: (1) an accurate estimate of the magnetic moment is possible using multiecho gradient echo imaging; and (2) the accuracy of the effective susceptibility can be improved using the magnetic moment when an estimate of the true volume is available. For validation, we used a gel phantom with air bubbles and glass beads to mimic the clinical situation of microbleeds. The method illustrated here does not depend on the susceptibility value or the size of the object.

THEORY

Current susceptibility mapping methods are based on the relationship between the susceptibility distribution and the magnetic field variation in the Fourier domain (1–6,10):

$$\Delta B(k) = G(k)\Delta\chi(k) \quad [1]$$

where $\Delta B(k)$ is the Fourier transform of the magnetic field variation $\Delta B(r)$, $\Delta\chi(k)$ is the Fourier transform of the susceptibility distribution $\Delta\chi(r)$, and $G(k)$ is the Green's function

$$G(k) = 1/3 - k_z^2/(k_x^2 + k_y^2 + k_z^2) \quad [2]$$

assuming that the main field direction is in the z -direction. Susceptibility quantification is an ill-posed inverse problem, owing to zeros in the Green's function $G(k)$ along the magic angle in the k -space domain. As a result, regularization is required, as $G(k)^{-1}$ is needed in the evaluation of susceptibility. In this study, we applied the regularization procedure described in a previous study (1) in which the intensity of $G(k)^{-1}$ is reasonably attenuated when the absolute value of $G(k)$ is below a

¹School of Biomedical Engineering, McMaster University, Hamilton, Ontario, Canada.

²Department of Radiology, Wayne State University, Detroit, Michigan, USA.

³The MRI Institute for Biomedical Research, Detroit, Michigan, USA.

Grant sponsor: National Institutes of Health; Grant numbers: DOD W81XWH-11-1-0493, NHLBI R21 HL 108230-A2; Grant sponsor: The Wayne State University Perinatal Research Initiative.

*Correspondence to: Jaladhar Neelavalli, Ph.D., Department of Radiology, Wayne State University, HUH-MR Research G030/Radiology, 3990 John R Street, Detroit, MI 48201. E-mail: jaladhar@wayne.edu

Received 25 November 2011; revised 29 March 2012; accepted 29 March 2012.

DOI 10.1002/mrm.24305

Published online 8 May 2012 in Wiley Online Library (wileyonlinelibrary.com).

threshold value. The selection of this threshold is a trade-off between the susceptibility-to-noise ratio of the reconstructed susceptibility map and the accuracy in susceptibility quantification (1,6). The threshold value was chosen to be 0.1 in this study.

Although ideally $\Delta\chi$ is the sought after parameter, when reduced resolution or T_2^* effects confound a clean measurement of the object's volume, it is more appropriate to investigate the associated magnetic moment (or, equivalently, the total or integrated susceptibility weighted by the voxel volume (12)). To see why this is the case, consider a sphere with a susceptibility difference $\Delta\chi$, the induced magnetic field at point $P(r, \theta)$ outside the sphere is given by (14):

$$\Delta B_{\text{out}}(r) = \frac{\Delta\chi r_0^3 (3\cos^2\theta - 1)B_0}{3r^3} \quad [3]$$

where $\Delta\chi = \chi_{\text{in}} - \chi_{\text{out}}$, χ_{in} is the susceptibility inside the object, χ_{out} is the susceptibility outside the object, r_0 is the radius of the sphere, r is the distance from the point $P(r, \theta)$ to the center of the sphere, and θ is the angle between the point P and the main field direction. For simplicity, the meaning of susceptibility in this article will be taken to be $\Delta\chi$ rather than χ_{in} or χ_{out} . Equation 3 also indicates that the product $\Delta\chi V$ is independent of echo time (TE), where $V = 4\pi r_0^3/3$ is the true volume of the sphere. The magnetic dipole moment of the spherical object is given as (14):

$$\mu = \frac{4\pi r_0^3 M}{3} \approx \frac{4\pi r_0^3 \Delta\chi B_0}{(3\mu_0)} \quad [4]$$

when $\Delta\chi$ is much smaller than 1. Here μ_0 is the permeability of free space and M is the induced magnetization. The product of $\Delta\chi$ and volume V is the effective magnetic moment term ($\Delta\chi V$) and is simply referred to as magnetic moment hereafter in this paper. The phase value at a particular TE is given in a right-handed system by:

$$\Delta\phi(r) = -\gamma\Delta B_{\text{out}}(r)TE \quad [5]$$

The susceptibility $\Delta\chi$ may be quantified using the phase information if the true volume (V) of the object is known. Otherwise, the magnetic moment ($\Delta\chi V$) may be found. As gradient echo images lead to a dephasing artifact and the object appears larger than its actual size, we defined an apparent volume V' and assuming that the susceptibility of this larger object can be accurately quantified, the magnetic moment could still be accurately calculated. An estimated susceptibility value $\Delta\chi'$ can be calculated from the Fourier-based method using Eqs. 1–5. The quantity $\Delta\chi'V'$ provides an estimate of the magnetic moment. Finally, the true susceptibility $\Delta\chi$ can be calculated using the following equation:

$$\Delta\chi = \Delta\chi'V'/V \quad [6]$$

In this study, we use three volume definitions. The first one is the true volume V . The second one is the apparent volume V' , which is used in estimating the

magnetic moment. The apparent volume is related to the signal loss owing to T_2^* dephasing and is determined from gradient echo magnitude images, as described later. The last one is the spin echo volume V_{se} , which is measured from the spin echo images. This volume is used as an MR-based estimate of the true volume. We used simulations and multiecho gradient echo images of a gel phantom containing air bubbles and glass beads of varying sizes to test Eq. 6. Although glass beads can be considered as almost perfect spheres, air bubbles are closer to the clinical situation of variable-shaped microbleeds.

METHODS

Simulations

To evaluate the validity of Eq. 6 for susceptibility calculation of small objects, we simulated magnitude and phase images of four spheres with different radii at 21 different TEs (from 0 to 20 ms, with a step size of 1 ms). In each simulation, the sphere was placed in the center of a 1024^3 matrix with complex elements. The radii of four spheres tested, within this 1024^3 matrix, were 32, 48, 64, and 96 pixels, respectively. The magnitude inside each sphere was set to 0, whereas the background magnitude was set to 300 to simulate intensities in the experimental data from the gel phantom. The phase images of the spheres were generated according to Eqs. 3 and 5 with $\Delta\chi = 9.4$ ppm. To simulate Gibbs ringing as well as partial volume effects seen in actual MR data, a process simulating the MR data sampling was used. Complex images generated in each 1024^3 matrix were Fourier transformed into k -space. The central 32^3 region was selected from k -space and was inverse Fourier transformed back to the imaging domain generating low-resolution data containing both Gibbs ringing and partial-volume effects. The radii of the four spheres became 1, 1.5, 2, and 3 pixels, respectively, in this final 32^3 volume. White gaussian noise was then added to the real and imaginary channels of the complex data in the image domain such that the signal-to-noise ratio in resultant magnitude images was 10:1. Susceptibility and the magnetic moment values were quantified for each of the spheres at all TEs and errors associated with these measurements were evaluated.

Phantom Experiments

A gel phantom, containing 14 small air bubbles and 9 glass beads of varying sizes, was imaged at 3T (Siemens VERIO, Erlangen, Germany) using a five-echo 3D gradient echo sequence. The TEs were 3.93, 9.60, 15.27, 20.94, and 26.61 ms, respectively. Other imaging parameters for the gradient echo sequence were repetition time 33 ms, flip angle 11° , read bandwidth 465 Hz/pixel, voxel size $0.5 \times 0.5 \times 0.5\text{mm}^3$, and matrix size $512 \times 304 \times 176$. A multislice 2D spin echo data set was also collected with flip angle of 90° , repetition time of 5000 ms, and TE = 15 ms and with the same field of view, bandwidth, resolution, and matrix size as in the gradient echo data set. This is to maintain a one-to-one correspondence of the spin echo with the gradient echo images of

the phantom. To ensure that the field perturbation measured in the phase images is the actual perturbation profile from the gel phantom, we first performed shimming using a spherical phantom immediately before performing the imaging experiment. Manual shimming was performed on the spherical phantom, to a spectral full-width at half-maximum of 13 Hz and the shim coefficients were noted. The same shim settings were used while imaging the gel phantom to ensure that field perturbation profile owing to the presence of the phantom in the magnet is not influenced by any additional shimming.

For the construction of the phantom, an agarose gel solution was prepared with an 8% concentration by weight and poured into a cylindrical container. In the lower portion of the container, the gel was first filled to one-third the height of the cylinder and nine glass beads of various sizes were embedded in the gel. The true diameter of the glass beads was roughly measured using calipers before the glass beads were put into the gel solution. Specifically, four glass beads were 2 mm in diameter, three glass beads were 3 mm in diameter, one glass bead was 5 mm in diameter, and the largest glass bead was 6 mm in diameter. The phantom was allowed to cool so that the gel solidified and properly engulfed the glass beads. The rest of the prepared gel solution was then poured into the cylindrical container and variable-sized bubbles were injected by pumping various amount of air into the gel using an empty syringe (two smallest air bubbles were excluded from this study, owing to the limitation in volume estimation of small objects; details are provided in later sections). The theoretical susceptibility difference between air and water is known to be 9.4 ppm and will be used to compare with the measurements from our method. For glass beads, the susceptibility values were measured independently in a former study to be -1.8 ± 0.3 ppm relative to water (15).

First, to identify air bubbles and glass beads in the collected MR data, binary masks from magnitude data were used. The intensity variation in the magnitude images caused by the RF field inhomogeneity was first removed using a 2D quadratic fitting, before the binary masks were created. A reasonably uniform magnitude intensity profile across the phantom was obtained after this intensity correction. The binary masks were created by local thresholding of the corrected magnitude images (11). First, a relatively strict threshold was used to pick only the voxels where the signal was $<50\%$ of the signal in the gel away from the air bubbles or glass beads, as both air bubbles and glass beads have much lower intensities than the intensity of the surrounding gel. Next, the mean ($\alpha_{\text{mag-gel}}$) and standard deviation ($\sigma_{\text{mag-gel}}$) were calculated for a cubic $21 \times 21 \times 21$ voxels volume of interest for each bubble or glass bead. A voxel roughly at the center of the bubble or glass bead was first chosen to center this 21^3 voxel window. The voxels picked up in the first step were excluded in the mean and standard deviation calculation. If a neighboring voxel has intensity lower than $\alpha_{\text{mag-gel}} - \beta\sigma_{\text{mag-gel}}$, it was regarded as a voxel belonging to air or glass bead. For the high signal-to-noise ratio data used here, β was empirically chosen to be 4 to separate air bubbles and glass beads from gel.

Susceptibility Quantification

To reduce the background field or phase variation, a forward modeling approach was used to estimate air/gel-phantom interface effects (16). The phase processing steps were as follows:

- i. The original phase images were first unwrapped using the phase unwrapping tool, PRELUDE, in FMRIB Software Library (FSL) (17). With the geometry of the gel phantom extracted from the magnitude images at the shortest TE (3.93 ms in this study), the background field effects were reduced by fitting the predicted phase to the unwrapped phase by a least squares method. An additional 2D quadratic fitting was added to remove the induced phase owing to eddy currents.
- ii. The phase value inside a particular air bubble/glass bead (where the binary mask is 1) was set to the mean phase (essentially 0) from the local $21 \times 21 \times 21$ window excluding the voxels which belong to the air bubble or glass bead. This is owing to the fact that the phase inside a sphere is theoretically zero and the nonzero phase is induced by the remnant background field variation as well as Gibbs ringing. This step also determines the apparent volume (V') from magnitude images.
- iii. At each TE, a $160 \times 160 \times 87$ voxel volume was cropped from the original phase images. This volume was selected because it covers most of the air bubbles and glass beads, whereas voxels near the edge of the gel phantom were excluded. The selected volume was then zero-filled to a $512 \times 512 \times 256$ matrix.
- iv. Susceptibility maps were generated using a threshold-based approach described previously in Ref. (1). The mean ($\alpha_{\chi\text{-air}}$ or $\alpha_{\chi\text{-glass}}$) and standard deviation ($\sigma_{\chi\text{-air}}$ or $\sigma_{\chi\text{-glass}}$) of the susceptibility values of air bubble (or glass bead) were measured, taking into account the background susceptibility of the gel. Measurements were obtained in the following manner: the background mean ($\alpha_{\chi\text{-gel}}$) and standard deviation ($\sigma_{\chi\text{-gel}}$) of the local gel susceptibility value around each bubble or glass bead was first calculated from the 21^3 voxel region centered around each of the bubble/bead. Within this 21^3 volume, the voxels belonging to the bubble or glass bead, as determined by the binary mask, were excluded for this background mean and standard deviation calculation. Once these measures were obtained, for susceptibility of air bubbles, only voxels with susceptibility values higher than $\alpha_{\chi\text{-gel}} + 3\sigma_{\chi\text{-gel}}$ were used for calculation purposes; whereas for glass beads, only voxels with a susceptibility value lower than $\alpha_{\chi\text{-gel}} - 3\sigma_{\chi\text{-gel}}$ were used. This process assumes that the noise in the susceptibility maps follows a gaussian distribution, and the susceptibility of a voxel consisting of air or glass is statistically different from a voxel consisting of gel. The change in sign is owing to the fact that the air bubbles are paramagnetic relative to the gel, whereas glass beads are diamagnetic. To account for the baseline shift caused by

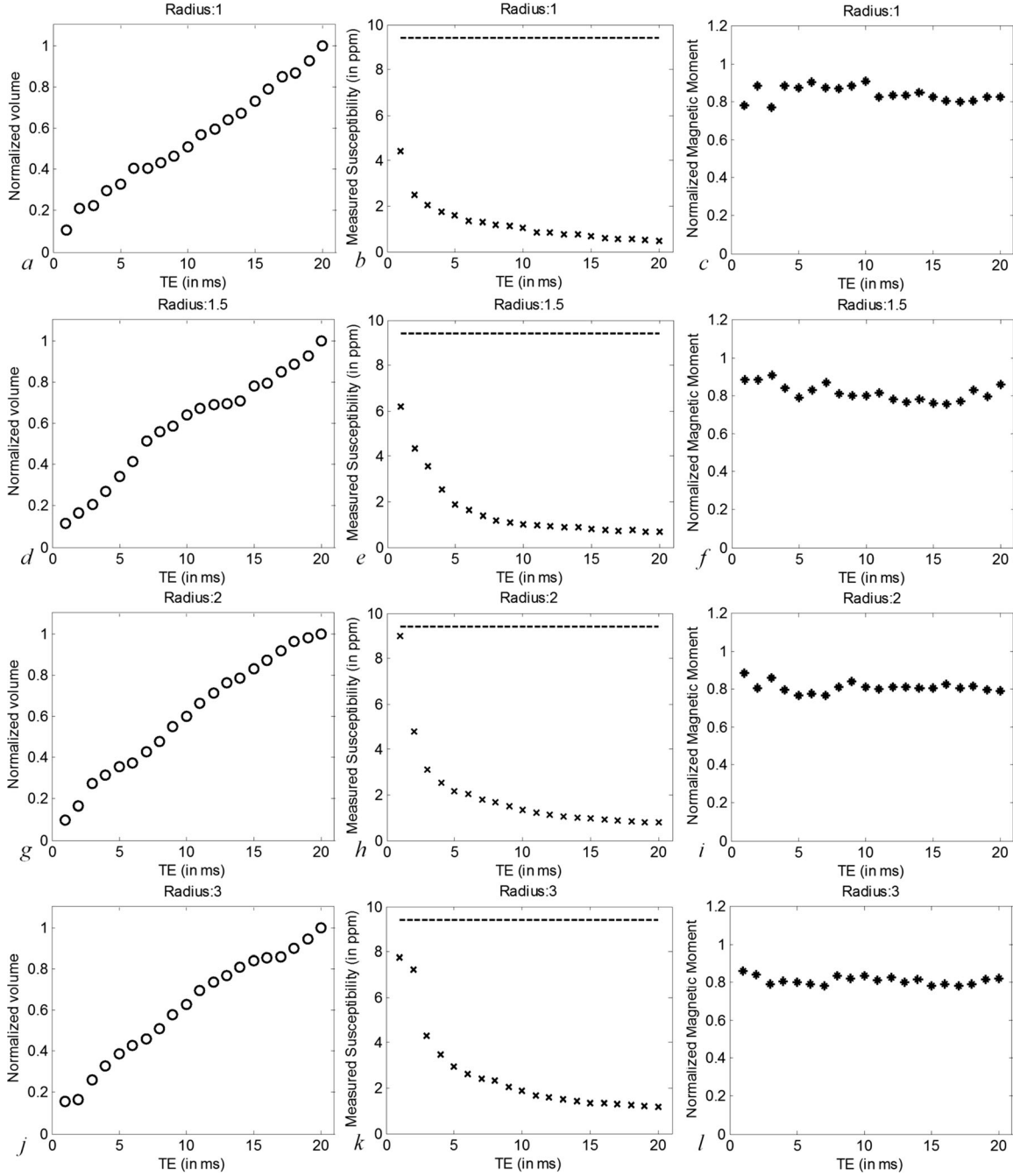


FIG. 1. Apparent volume normalized to the volume at TE = 20 ms (first column), measured susceptibility (second column), and normalized magnetic moments (third column) measured at different TEs of four different spheres. The dashed lines in the second column (**b**, **e**, **h**, and **k**) indicate the true susceptibility 9.4 ppm. For each sphere, the effective magnetic moments were normalized to the true effective magnetic moment.

remnant field variation, the susceptibility of the air bubble (or glass bead) was taken as $\alpha_{\chi\text{-air}}$ – $\alpha_{\chi\text{-gel}}$ (or $\alpha_{\chi\text{-glass}}$ – $\alpha_{\chi\text{-gel}}$).

Volume Measurement

The apparent volume of the air bubble or glass bead was determined from the binary masks directly, i.e., by counting the number of voxels inside the air bubble or glass bead. On the other hand, the spin echo volume is

measured utilizing the “object strength” notion proposed by Tofts et al. (18), in which the total intensity is measured for a particular volume of interest. For a volume composed of two types of tissues, a and b, the total intensity can be expressed as

$$I = I_a \cdot n_a + I_b \cdot (N - n_a) = (I_a - I_b) \cdot n_a + I_b \cdot N \quad [7]$$

where I is the total intensity, “ I_a ” and “ I_b ” are the intensities of the voxels containing purely tissue “a” or tissue “b,” respectively. The total number of voxels in this

Table 1
Spin Echo Volume (in Voxels) and the Diameter (in mm) Calculated from Spin Echo Volume for Each Glass Bead

Bead	1	2	3	4	5	6	7	8	9
Measure									
Spin echo volume	35.4	37.5	38.2	39.1	96.5	103.8	113.6	516.6	912.1
Spin echo diameter	2.0	2.1	2.1	2.1	2.9	2.9	3.0	5.0	6.0
Actual diameter	2.0	2.0	2.0	2.0	3.0	3.0	3.0	5.0	6.0

volume of interest is denoted by “ N ,” and the number of voxels occupied by tissue “a” is denoted by “ n_a .” Consequently, the number of voxels occupied by tissue “b” can be expressed as $N - n_a$.

By varying the size of the volume of interest, the total intensity is linearly dependent on the number of voxels in the volume of interest. Although “ I_b ” can be determined as the slope in the fit to Eq. 7, n_a can be calculated from the intercept if “ I_a ” is given (n_a may not be an integer as partial volume is included). In this study, “ I_b ” corresponds to the intensity of a voxel composed purely of gel, whereas “ I_a ” corresponds to the intensity of a voxel composed purely of air or glass. For a relatively large air bubble or glass bead, “ I_a ” is dominated by the thermal noise, which can be approximated as $1.25 \times \sigma_{\text{mag-gel}}$, where $\sigma_{\text{mag-gel}}$ is the measured standard deviation of the gel region in the magnitude images (19). For an air bubble or glass bead with a radius generally <3 pixels, “ I_a ” is a combination of thermal noise and Gibbs ringing. To best account for these fluctuations, “ I_a ” is calculated from:

$$I_a = \begin{cases} w_1 \cdot \alpha_{\text{mag-air}} + w_2 \cdot 1.25 \cdot \sigma_{\text{mag-gel}}, & \text{for air bubble} \\ w_1 \cdot \alpha_{\text{mag-glass}} + w_2 \cdot 1.25 \cdot \sigma_{\text{mag-gel}}, & \text{for glass bead} \end{cases} \quad [8]$$

where $\alpha_{\text{mag-air}}$ and $\alpha_{\text{mag-glass}}$ are the measured mean values inside the bubble and glass bead, respectively; w_1 and w_2 are two weighting factors. Based on our simulations (explained below), w_1 and w_2 were empirically determined from simulations to be 0.4 and 0.6, respectively, to minimize the error in estimation of the true volume.

Error in Volume Measurement

Although a regression method is used to measure the spin echo volume, it is still affected by partial volume effects, Gibbs ringing, as well as random noise. The simulated magnitude images at TE = 0 were used to mimic spin echo magnitude images and to study the error in spin echo volume estimation. In addition, to examine the stability of this method relative to thermal noise, the volume measurement evaluation was performed 10 times for each simulated sphere, with inde-

pendently generated random noise for each of these simulations. The errors were determined by comparing the measured volume with the true volume. Note that this error estimation does not apply for the apparent volume which is determined directly from the binary masks.

RESULTS

Simulations

Magnetic moments for simulated spheres were calculated with the measured susceptibilities and the apparent volume for each sphere at a given TE. The results across different TEs are shown in Fig. 1. The measured volumes at different TEs were normalized to the volume at the longest TE, whereas the measured magnetic moments were normalized to the true magnetic moment, which is the product of input volume (i.e., the true volume) of the sphere and the input susceptibility (true susceptibility) 9.4 ppm. The normalized magnetic moment is roughly a constant for all spheres. However, for the sphere with a radius <2 pixels, the magnetic moments measured in the short TE range have more fluctuations than those measured at longer TEs. In addition, the magnetic moments are under-estimated for all spheres. The mean normalized magnetic moments were measured as: 0.85 ± 0.04 (radius = 1 pixel), 0.82 ± 0.05 (radius = 1.5 pixels), 0.81 ± 0.03 (radius = 2 pixels), and 0.81 ± 0.02 (radius = 3 pixels).

After the magnetic moments were obtained, the susceptibility values were corrected using the actual known volume (i.e., true volume) using Eq. 6. Specifically, the corrected susceptibilities are 7.95 ± 0.38 ppm (radius = 1 pixel), 7.70 ± 0.43 ppm (radius = 1.5 pixels), 7.62 ± 0.27 ppm (radius = 2 pixels), and 7.63 ± 0.21 ppm (radius = 3 pixels). There is still a 15–19% underestimation in the averaged susceptibility after attempting to correct the volume of the sphere.

To evaluate the stability of the volume measuring method, we carried out 10 simulations for each sphere at TE = 0. The means and standard deviations of the percentage errors relative to true volume for each sphere are $18.02 \pm 27.26\%$ (radius = 1 pixel), $1.89 \pm 12.18\%$ (radius = 1.5 pixels), $3.67 \pm 8.91\%$ (radius = 2 pixels), and $2.09 \pm 2.54\%$ (radius = 3 pixels). The algorithm failed to

Table 2
Spin Echo Volume (in Voxel) of the 14 Air Bubbles

Bubble	1	2	3	4	5	6	7
Volume	3.3	15.1	28.7	42.2	43.9	82.8	87.7
Bubble	8	9	10	11	12	13	14
Volume	92.7	118.2	170.5	238.6	288.7	322.7	897.2

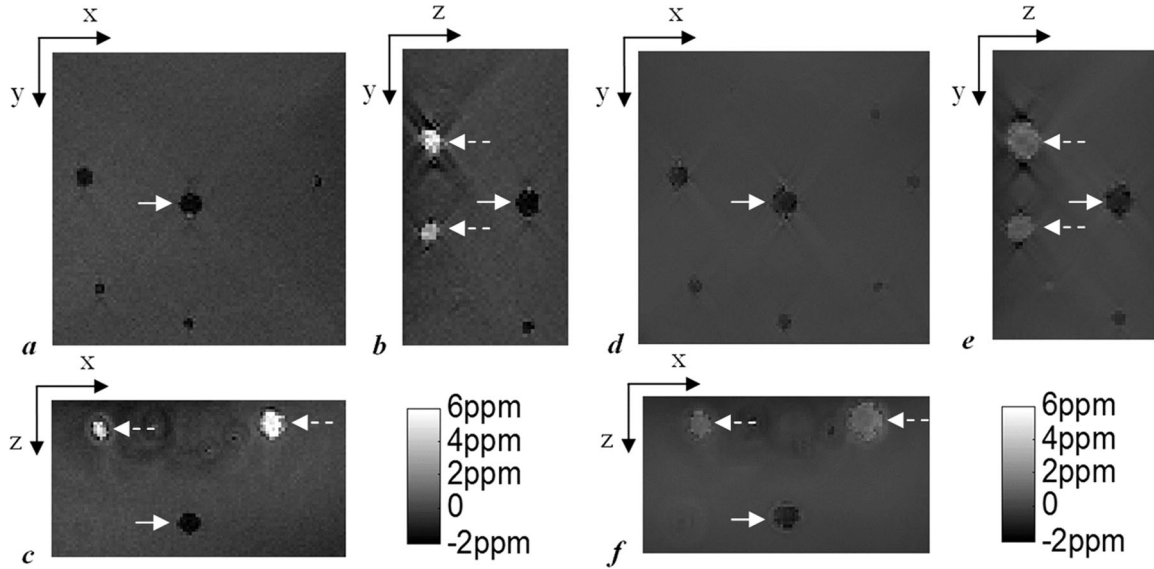


FIG. 2. Axial, sagittal, and coronal views of the susceptibility maps with TE = 3.93 ms (**a**, **b**, and **c**) and TE = 26.61 ms (**d**, **e**, and **f**). The main field direction is in “y” direction. Glass bead No. 9 in Table 1 is pointed by the white arrows. The air bubbles are indicated by the white dashed arrows.

quantify, in two of the 10 simulations for sphere with radius of 1 pixel. Larger errors and more variations of the volume measurements were seen in spheres with radii < 2 pixels. For the sphere with a radius of 3 pixels, the error in the volume estimation appears to be within 5% using the proposed method. As can be expected, when the object radius is only 1 pixel, the volume measurement becomes unstable.

Phantom Experiments

A total of 14 air bubbles and 9 glass beads were examined in the phantom data. The measured spin echo volumes of the glass beads and air bubbles are summarized in Tables 1 and 2. In these two tables, the glass beads as well as air bubbles are sorted based on their spin echo volumes, from small to large objects. The diameters of these glass beads calculated from their spin echo volumes agree reasonably well with their physically measured diameters, as summarized in Table 1. Also note that the error in volume measurement is unreliable for spherical objects with radii < 1.5 pixels (14.13 voxels for the volume). The error is generally larger than 20%, as shown in the simulations. Thus, the first two smallest air bubbles were excluded from the analysis.

Figure 2 shows three orthogonal views of the susceptibility map of the largest glass bead for the shortest TE

and the longest TE. Using Eq. 6, the measured susceptibilities can be corrected with the volume estimated from the spin echo images. These results are summarized in Table 3. The mean of the corrected susceptibility values of the glass beads averaged over all the TEs is -1.82 ± 0.17 ppm, which is within the range of the measured values in the previous study (15). The mean of the corrected susceptibility values of the air bubbles is 6.66 ± 0.85 ppm. This is to be compared to the actual susceptibility of 9.4 ppm.

DISCUSSION

The susceptibility mapping technique using the regularized Fourier-based method has certain advantages over other methods, especially in terms of time efficiency and simplicity. However, it suffers from problems caused by the intrinsic singularities in the inverse of the Green’s function, as well as partial volume effects which disrupt the true phase behavior. For small objects, susceptibility quantification using the inverse method (1) yields a significant underestimation of the susceptibility. The increased apparent volume at long TE can be utilized to create a larger virtual object for which the actual susceptibility can be more accurately measured and thus the Fourier-based susceptibility quantification gives a relatively smaller error for the magnetic moment. At this point, the

Table 3
Mean Measured and Corrected Susceptibilities (in ppm) of the Glass Beads and Air Bubbles at Different TEs

TE/ms	Glass Bead		Air bubble	
	Measured	Corrected	Measured	Corrected
3.93	-1.50 ± 0.07	-1.79 ± 0.13	3.15 ± 1.16	6.13 ± 0.77
9.60	-1.07 ± 0.32	-1.76 ± 0.13	1.70 ± 0.61	6.44 ± 0.90
15.27	-0.86 ± 0.32	-1.82 ± 0.19	1.30 ± 0.45	6.64 ± 0.76
20.94	-0.68 ± 0.28	-1.82 ± 0.18	1.07 ± 0.36	6.88 ± 0.77
26.61	-0.59 ± 0.25	-1.88 ± 0.21	0.93 ± 0.34	7.22 ± 0.74

susceptibility close to the actual value can be extracted from the estimated magnetic moment with an estimation of the true volume, either if it is known ahead of time, or it can be estimated from a high-resolution spin echo data set.

Based on the discussions above, the error $\delta\Delta\chi$ in the corrected susceptibility $\Delta\chi$ comes from the estimated magnetic moment $\mu_a = \Delta\chi'V'$ and estimated volume (V). Through error propagation, the error in the corrected susceptibility is given by:

$$\frac{\delta\Delta\chi}{|\Delta\chi|} = \sqrt{\left(\frac{\delta\mu_a}{\mu_a}\right)^2 + \left(\frac{\delta V}{V}\right)^2} \quad [9]$$

As we can see, the smaller the error in the estimated volume, the smaller the error in the corrected susceptibility. This equation explains the error seen in the corrected susceptibility of the air bubbles as well as glass beads.

In simulations, where the true volume is known, the remnant underestimation in the averaged corrected susceptibility ranges from 15 to 19%. As there is no error in the true volume, this error must be owing to the error in the apparent volume measurement and $\Delta\chi'$ quantification owing to the regularization process. The level of underestimation is related to the threshold value in the inverse of the Green's function. A smaller threshold leads to less underestimation, but more streaking artifacts in the susceptibility maps. The regularized Fourier-based method, with threshold value of 0.1, can lead to an underestimation of around 13% for objects with radii larger than 3 pixels and even worse for smaller objects (1,6). This can be viewed as a systematic error.

In phantom studies, after using the volume estimated from the spin echo data, the corrected susceptibility values of the air bubbles have a maximum underestimation close to 44%, compared to the theoretical value 9.4 ppm. This is essentially a consequence of error in the spin echo volume measurement and the underestimation of $\Delta\chi'$ quantified using the Fourier-based method. To overcome these limitations, one has to go to high-resolution images that can minimize volume quantification error and to relatively longer TEs that can improve accuracy in the magnetic moment quantification. However, the decreased signal-to-noise ratio in high-resolution spin echo images may introduce additional variation/noise in the final volume results.

There are a number of limitations to this study. Although a forward calculation was carried out to reduce the geometry induced field variation, remnant background field variation still exists. To best account for it, the phase inside the spherical objects was set to the local average phase. This also helps to reduce the large variation in susceptibility estimate induced by Gibbs ringing and thermal noise. However, this phase correction process is based on the assumption that the object of interest is a sphere. For nonspherical objects, this phase correction process may lead to variations of magnetic moment at different TEs. In addition, phase correction also creates a virtually larger object. It is possible that the center of the created object deviates from the true center of the original object of interest. This leads to additional errors even for spherical objects, as

seen from simulations. Thus, the phase inside the spherical object has significant effects to this method. Theoretically, only when the center of a simulated large sphere coincides with the original center of the sphere, and when the background phase value is 0, we can obtain a constant magnetic moment across different TEs. Hence, slight variations in object definition from a binary mask, which is used for phase substitution, can introduce variations in magnetic moment values. This is the essential source of shape dependence of the proposed method.

Although the estimated magnetic moments of the glass beads are almost a constant over different TEs, as indicated by the corrected susceptibilities, the estimated magnetic moments of the air bubbles are usually larger at a longer TE than at a shorter TE. This can be understood by the fact that the air bubbles are not perfect spherical objects compared to the glass beads. In fact, most of the air bubbles have ellipsoidal shapes, and any attempt of phase correction inside the bubble based on the assumption of the spherical shape will cause errors in the susceptibility measurement and thus lead to errors in the measurement of the magnetic moments.

Generally speaking, for small objects which can be well approximated as spheres, the theoretically expected errors in the estimated magnetic moment measurements are within 20% of the expected values and can be further reduced by adjusting the regularization thresholds in the susceptibility mapping method. Practically, the errors might be larger owing to the limited knowledge of the true volume. Although most small microbleeds can be well approximated as spheres, the use of more accurate volume estimation methods has the potential to reduce the error in susceptibility quantification of microbleeds.

CONCLUSIONS

In conclusion, we have shown that for very small structures, obtaining accurate magnetic susceptibility values is limited by the errors in the volume estimations of these structures and in the Fourier-based method itself. Despite this inability to estimate the actual volume of a small object accurately (whether it is an air bubble or microbleed), the estimated magnetic moment is almost a constant over different TEs. This demonstrates that it is possible to measure the magnetic moment at a longer TE when the apparent volume is increased owing to T_2^* dephasing. By measuring or knowing *a priori* the actual volume of an object, it is possible to obtain a reasonable estimate of the susceptibility.

REFERENCES

1. Haacke EM, Tang J, Neelavalli J, Cheng YC. Susceptibility mapping as a means to visualize veins and quantify oxygen saturation. *J Magn Reson Imaging* 2010;32:663–676.
2. Liu T, Spincemaille P, de Rochefort L, Kressler B, Wang Y. Calculation of susceptibility through multiple orientation sampling (COSMOS): a method for conditioning the inverse problem from measured magnetic field map to susceptibility source image in MRI. *Magn Reson Med* 2009;61:196–204.
3. de Rochefort L, Brown R, Prince MR, Wang Y. Quantitative MR susceptibility mapping using piece-wise constant regularized inversion of the magnetic field. *Magn Reson Med* 2008;60:1003–1009.

4. Schweser F, Deistung A, Lehr BW, Reichenbach JR. Quantitative imaging of intrinsic magnetic tissue properties using MRI signal phase: an approach to in vivo brain iron metabolism? *NeuroImage* 2011;54:2789–2807.
5. Wharton S, Schäfer A, Bowtell R. Susceptibility mapping in the human brain using threshold-based k-space division. *Magn Reson Med* 2010;63:1292–1304.
6. Shmueli K, de Zwart JA, van Gelderen P, Li T, Dodd SJ, Duyn JH. Magnetic susceptibility mapping of brain tissue in vivo using MRI phase data. *Magn Reson Med* 2009;62:1510–1522.
7. Ayaz M, Boikov AS, Haacke EM, Kido DK, Kirsch WM. Imaging cerebral microbleeds using susceptibility weighted imaging: one step toward detecting vascular dementia. *J Magn Reson Imaging* 2010;31:142–148.
8. Greenberg SM, Vernooij MW, Cordonnier C, Viswanathan A, Al-Shahi Salman R, Warach S, Launer LJ, Van Buchem MA, Breteler MM. Cerebral microbleeds: a guide to detection and interpretation. *Lancet Neurol* 2009;8:165–174.
9. Yates PA, Sirisiri R, Villemagne VL, Farquharson S, Masters CL, Rowe CC, For the AIBL Research Group. Cerebral microhemorrhage and brain β -amyloid in aging and Alzheimer disease. *Neurology* 2011;77:48–54.
10. Cheng Y-CN, Neelavalli J, Haacke EM. Limitations of calculating field distributions and magnetic susceptibilities in MRI using a Fourier based method. *Phys Med Biol* 2009;54:1169–1189.
11. McAuley G, Schrag M, Barnes S, Obenaus A, Dickson A, Holshouser B, Kirsch W. Iron quantification of microbleeds in postmortem brain. *Magn Reson Med* 2011;65:1592–1601.
12. Liu T, Surapaneni K, Lou M, Cheng L, Spincemaille P, Wang Y. Cerebral microbleeds: burden assessment by using quantitative susceptibility mapping. *Radiology* 2012;262:269–278.
13. Cheng Y-C, Hsieh C-Y, Neelavalli J, Haacke EM. Quantifying effective magnetic moments of narrow cylindrical objects in MRI. *Phys Med Biol* 2009;54:7025–7044.
14. Haacke EM, Brown RW, Thompson MR, Venkatesan R. *Magnetic resonance imaging: physical principles and sequence design*, 1st ed. New York: Wiley-Liss; 1999.
15. Hsieh C, Cheng Y, Tackett R, Kumar R, Lawes G, Haacke E. TH-D-304A-02: quantifying magnetic moments and susceptibilities of small spherical objects in MRI. *Med Phys* 2009;36:2816.
16. Neelavalli J, Cheng YN, Jiang J, Haacke EM. Removing background phase variations in susceptibility-weighted imaging using a fast, forward-field calculation. *J Magn Reson Imaging* 2009;29:937–948.
17. Jenkinson M. Fast, automated, N-dimensional phase-unwrapping algorithm. *Magn Reson Med* 2003;49:193–197.
18. Tofts PS, Silver NC, Barker GJ, Gass A. Object strength—an accurate measure for small objects that is insensitive to partial volume effects. *MAGMA* 2005;18:162–169.
19. Gudbjartsson H, Patz S. The Rician distribution of noisy MRI data. *Magn Reson Med* 1995;34:910–914.

Improving Susceptibility Mapping Using a Threshold-Based K-Space/Image Domain Iterative Reconstruction Approach

J. Tang,¹ S. Liu,¹ J. Neelavalli,² Y. C. N. Cheng,² S. Buch,¹ and E. M. Haacke^{1–3*}

To improve susceptibility quantification, a threshold-based k-space/image domain iterative approach that uses geometric information from the susceptibility map itself as a constraint to overcome the ill-posed nature of the inverse filter is introduced. Simulations were used to study the accuracy of the method and its robustness in the presence of noise. In vivo data were processed and analyzed using this method. Both simulations and in vivo results show that most streaking artifacts inside the susceptibility map caused by the ill-defined inverse filter were suppressed by the iterative approach. In simulated data, the bias toward lower mean susceptibility values inside vessels has been shown to decrease from around 10% to 2% when choosing an appropriate threshold value for the proposed iterative method. Typically, three iterations are sufficient for this approach to converge and this process takes less than 30 s to process a $512 \times 512 \times 256$ dataset. This iterative method improves quantification of susceptibility inside vessels and reduces streaking artifacts throughout the brain for data collected from a single-orientation acquisition. This approach has been applied to vessels alone as well as to vessels and other structures with lower susceptibility to generate whole brain susceptibility maps with significantly reduced streaking artifacts. **Magn Reson Med** 69:1396–1407, 2013. © 2012 Wiley Periodicals, Inc.

Key words: oxygen saturation; susceptibility mapping; susceptibility weighted imaging

Susceptibility weighted imaging (SWI) using phase information has become an important clinical tool (1–3). However, the use of phase information itself has stimulated great interest both as a source of contrast (4–6) and a source for producing susceptibility maps (SM) (7–24). The impetus for solving the inverse problem from magnetic field perturbation came from the work described by Deville et al. (25). This was noted by Marques and Bowtell in 2005 (26). Salomir et al. (27) were the first group

to utilize this concept in MRI. Unfortunately, this inverse process is ill-posed and requires a regularization procedure to estimate the SM. There are a variety of approaches to tackle this problem (7–24). One unique method uses a multiple orientation data acquisition to remove the singularities (17). Constrained regularizations (14,20,22,23) have shown good overall results, but they require longer reconstruction times and assumptions about the contrast in or near the object to be detected. Threshold-based, single-orientation regularization methods (TBSO) (11,15,18,24) provide the least acquisition time and the shortest computational time to calculate SM. However, their calculated SMs lead to underestimated susceptibility values ($\Delta\chi$) and display severe streaking artifacts especially around structures with large $\Delta\chi$, such as veins or parts of the basal ganglia.

Based on TBSO approaches, we propose an iterative method to overcome the singularities in the inverse filter and produce improved accuracy for susceptibility mapping. In this approach, we iteratively replace k-space values associated with the SM, $\chi(k)$, near the singularities to obtain an almost artifact free SM, $\chi(r)$. The k-space values used for substitutions are estimated using structural information from the masked version of $\chi(r)$. Simulations using 2D cylinders and full brain 3D models were performed to examine the efficacy of this iterative approach. High resolution human data are also evaluated.

METHODS

Briefly, the expression for the susceptibility distribution (26,27) derived from the phase data can be written as (for a right handed system (28)):

$$\chi(r) = \text{FT}^{-1} \left[\frac{1}{g(k)} \times \text{FT} \left[\frac{\Phi(r)}{-\gamma B_0 T_E} \right] \right] \quad [1]$$

where,

$$g(k) = \frac{1}{3} - \frac{k_z^2}{k_x^2 + k_y^2 + k_z^2} \quad [2]$$

and $\Phi(r)$ is the phase distribution, T_E is the echo time, γ is the gyromagnetic ratio for hydrogen protons, B_0 is the main field strength, k_x , k_y , and k_z are coordinates in k-space, and $g(k)$ is the Green's function or filter. Clearly, the analytic inverse filter $g^{-1}(k) = 1/g(k)$, is ill-posed when $g(k)$ is equal or close to zero, i.e., points on or near two conical surfaces in k-space at the magic angles of 54.7° and 125.3° from the B_0 axis. This ill-posedness leads to severe artifacts (including severe streaking) in

¹School of Biomedical Engineering, McMaster University, Hamilton, Canada.

²Department of Radiology, Wayne State University, Detroit, Michigan, USA.

³The MRI Institute for Biomedical Research, Detroit, Michigan, USA.

Grant sponsor: National Institutes of Health; Grant numbers: NHLBI R01HL062983-A4, NHLBI R21 HL 108230-A2; Grant sponsor: DoD grant; Grant number: W81XWH-11-1-0493.

*Correspondence to: E. Mark Haacke, Ph.D., Department of Radiology, Wayne State University, 3990 John R Street, Detroit MI 48201, USA. E-mail: nmrimaging@aol.com

Received 13 September 2011; revised 29 May 2012; accepted 30 May 2012.

DOI 10.1002/mrm.24384

Published online 26 June 2012 in Wiley Online Library (wileyonlinelibrary.com).

© 2012 Wiley Periodicals, Inc.

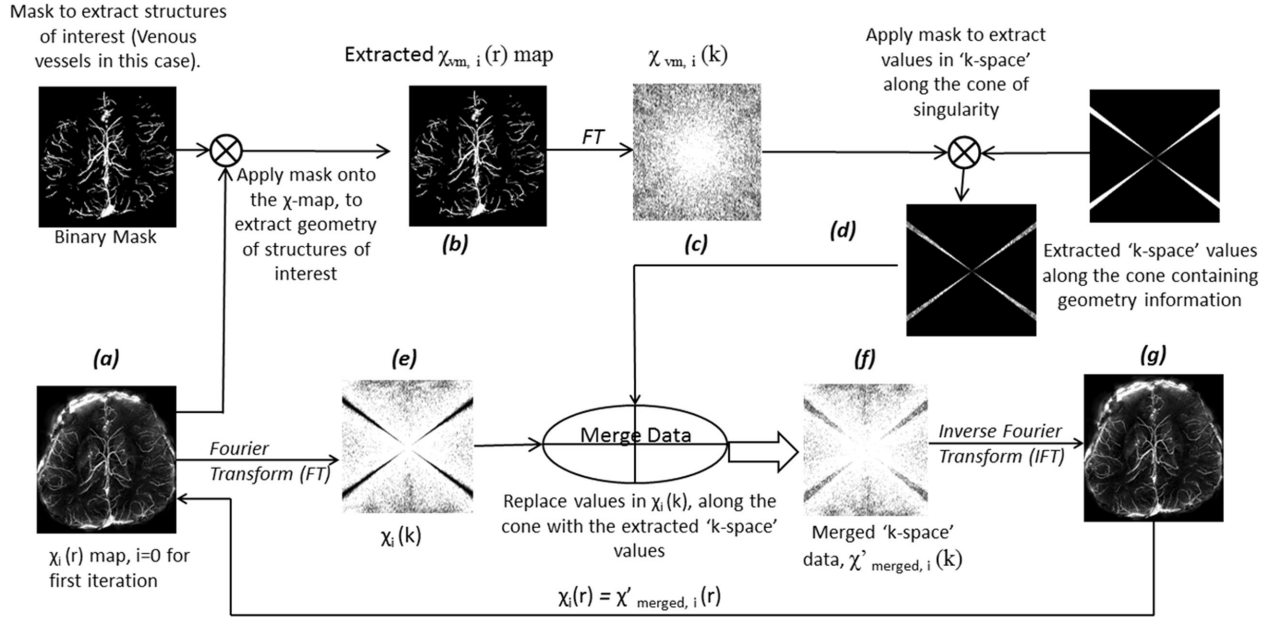


FIG. 1. Illustration of the iterative reconstruction algorithm to obtain artifact free $\chi(r)$ maps.

$\chi(k)$ and noise amplification (29). Thus, for a proper pixel-by-pixel reconstruction of $\chi(r)$, recovering the correct values of $\chi(k)$ near the region of singularities is critical.

K-space Iterative Approach

If the shapes of the structures of interest are known, then one can use this information in the SM to create a more accurate k-space of said SM in the conical region. The structure of the vessels is obtained directly from the first pass SM $\chi_{i=0}(r)$. The detailed steps of the iterative method are discussed below and shown in Fig. 1.

- **Step-1:** An initial estimate of the SM, $\chi_{i=0}(r)$, is obtained by applying a regularized version of the threshold-based inverse filter, $g_{reg}^{-1}(k)$ (18), in Eq. 1 using the suggested threshold value, $thr = 0.1$. The subscript “ i ” denotes the SM after the i th iteration (“ $i = 0$ ” denotes the initial step before doing the iterative method and $i = 1$ for the first iteration).
- **Step-2:** The geometry of the structures of interest is extracted from $\chi_{i=0}(r)$ using a binary vessel mask, i.e. outside the veins, the signal in the mask is set to zero, and inside it is set to unity. Since streaking artifacts associated with veins in the SM are usually outside the vessels, after multiplying the $\chi_i(r)$ map by the mask, little streaking remains in the SM. This leads to $\chi_{vm,i}(r)$ as shown in Fig. 1b. Vessel mask generation will be addressed in the next section.
- **Step-3:** $\chi_{vm,i}(k)$ is obtained by Fourier transformation of $\chi_{vm,i}(r)$ (Fig. 1c).
- **Step-4:** The predefined ill-posed region of k-space in $\chi_{vm,i}(k)$ is extracted (Fig. 1d). These extracted k-space data are denoted by $\chi_{vm,cone,i}(k)$. The size of $\chi_{vm,cone,i}(k)$ is decided by a threshold value, a , which is assigned to $g(k)$. For the matrix size 512×512 , the percentages of the cone region in

k-space for a given a , are 2.4% ($a = 0.01$), 24.1% ($a = 0.1$), 47.1% ($a = 0.2$), and 70.6% ($a = 0.3$), respectively. When a increases, the size of $\chi_{vm,cone,i}(k)$ increases too. If a is increased too much then most of the original information will be lost.

- **Step-5:** Data from $\chi_{vm,cone,i}(k)$ and $\chi_{i=0}(k)$ (Fig. 1e) are merged. This means part of $\chi_{i=0}(k)$ has been replaced by $\chi_{vm,cone,i}(k)$. The merged data are denoted by $\chi'_{merged,i}(k)$ (Fig. 1f).
- **Step-6:** Inverse Fourier transformation of $\chi'_{merged,i}(k)$ gives the improved SM, $\chi_{i+1}(r)$ (Fig. 1g).
- **Step-7:** $\chi_i(r)$ in step-1 is replaced by $\chi_{i+1}(r)$ from step-6 and the algorithm is repeated until

$$\sqrt{\sum [(\chi_i(r) - \chi_{i+1}(r))^2] / N} < \epsilon \quad [3]$$

where N is the number of pixels in $\chi_i(r)$ and ϵ is the tolerance value (chosen here to be 0.004 ppm).

Binary Vessel Mask Generation

The binary vessel mask was generated using thresholding from the $\chi(r)$ map itself. The detailed steps are discussed below and shown in Fig. 2.

- **Step-1:** A threshold, th_1 , is applied to $\chi_{i=0}(r)$ to create an initial binary vessel mask, M_0 . The pixels whose susceptibility values are lower than th_1 will be set to zero while those greater than or equal to th_1 will be set to unity. In this study, a relatively low susceptibility of 0.07 ppm is used for th_1 to capture most vessels. However, this choice of threshold inevitably includes other brain structures in M_0 that have high susceptibility.
- **Step-2:** A morphological closing operation is performed to fill in holes in M_0 to generate an updated mask M_1 .

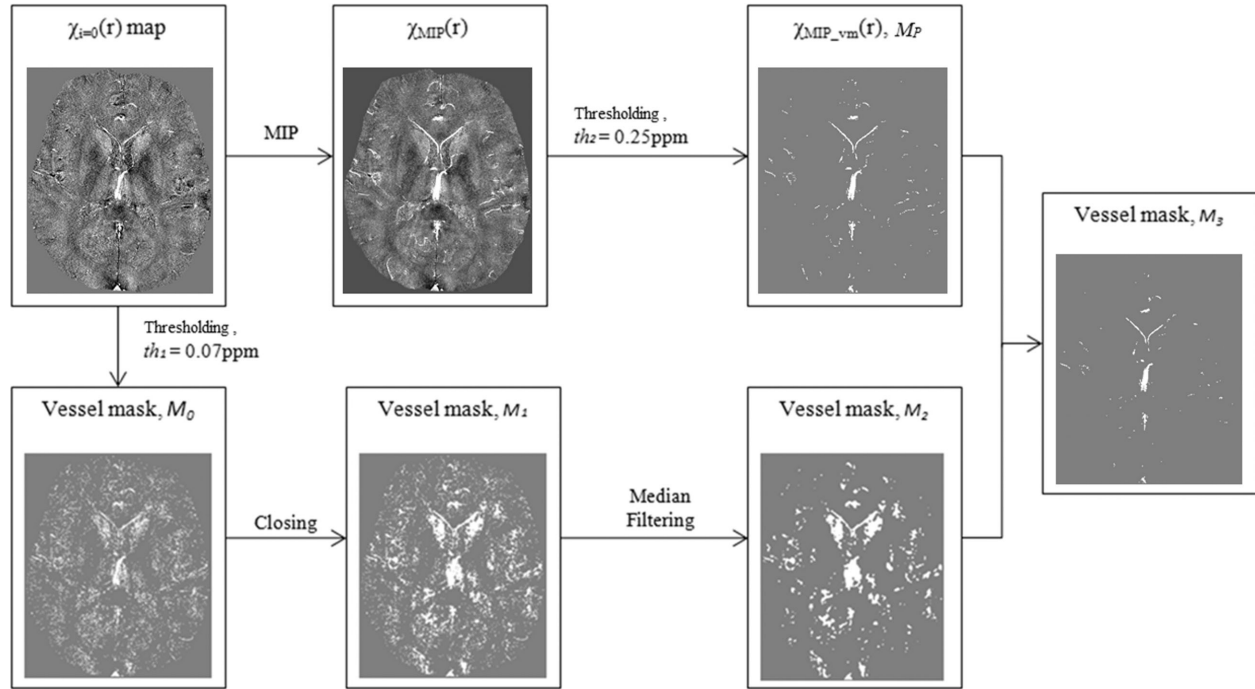


FIG. 2. Illustration of the binary vessel mask generation process.

- **Step-3:** A median filter is applied to remove noise in M_1 and create M_2 .
- **Step-4:** False positive data points from M_2 are removed as follows: First, the $\chi(r)$ map is Mipped over five slices centered about the slice of interest to better obtain contiguous vessel information, as seen in $\chi_{MIP}(r)$. Second, another threshold, $th_2 = 0.25$ ppm, is performed on $\chi_{MIP}(r)$ to create a new $\chi_{MIP_vm}(r)$ and binary mask M_P , which only contains predominantly vessels. Here, 0.25 ppm was chosen to isolate the major vessels in the MIP image. Third, each slice from M_2 is compared with M_P on a pixel-by-pixel basis to create M_3 . If a data point from M_2 does not appear on M_P , this data point will be treated as a false positive and removed from M_2 , otherwise this point is retained. This process can be equally well applied to extract other tissues by choosing appropriate values for th_1 and th_2 .

2D Cylinder Simulations

Simulation of a two dimensional cylinder and its induced phase was first performed using a 8192×8192 matrix. A lower resolution complex image was then obtained by taking the Fourier transform of this matrix and applying an inverse Fourier transform of the central 512×512 matrix in k-space. This procedure is to simulate Gibbs ringing effects caused by finite sampling which we usually see in conventionally required MR data sets. Gibbs ringing comes from discontinuities in both the magnitude and phase images. To avoid Gibbs ringing from magnitude discontinuities, we used a magnitude image with a uniform signal of unity. Cylinders with diameters 32, 64, 128, 256, 512, and 1024 were simulated on 8192×8192 matrices and their effective

diameters were 2, 4, 8, 16, 32, and 64 on 512×512 matrices. All phase simulations were performed using a forward method (8,26,27,30) with $B_0 = 3$ T, $\Delta\chi = 0.45$ ppm in SI units, $T_E = 5$ ms, and the cylinder perpendicular to the main magnetic field. The susceptibility value of 0.45 ppm represents venous blood when the hematocrit (Hct) = 0.44, $\Delta\chi_{do} = 4\pi \cdot 0.27$ ppm (31) and the oxygen saturation level = 70%, where $\Delta\chi_{do}$ is the susceptibility difference between fully deoxygenated and fully oxygenated blood (32). A relatively short echo time was chosen to avoid phase aliasing that can affect the estimated susceptibility values.

Selection of a TBSO Method to Generate the $\chi_{i=0}(r)$ Map

TBSO methods (11,15,18,24) use a truncated $g(k)$ to solve the singularity problem in the inverse filter $g^{-1}(k)$ when $g(k)$ is less than a predetermined threshold value, thr . When $g(k) < thr$, $g^{-1}(k)$ is either set to zero (11,24); or to $1/thr$ (15); or set to $g^{-1}(k) = 1/thr$ first and then $g^{-1}(k)$ is brought smoothly to zero as k approaches k_{zo} . This smoothing is accomplished by multiplying $g^{-1}(k)$ by $\alpha^2(k_z)$ with $\alpha(k_z) = (k_z - k_{zo})/|k_{zthr} - k_{zo}|$ where k_z is the z component of that particular point in k-space, k_{zo} is the point at which the function $g^{-1}(k)$ becomes undefined, and k_{zthr} is the k_z coordinate value where $|g(k)| = thr$ (18).

SMs using the methods in Refs. 11,15,18 were calculated based on Eq. 1 using the 2D cylindrical model. Equation 1 can be used to calculate the SM for the simulated 2D cylinder model perpendicular to the main field since the 2D perpendicular model is a special case of the 3D model with 1 slice [10]. Streaking artifacts are obvious in all three SMs (figures are not shown). The calculated mean susceptibility values inside the cylinder

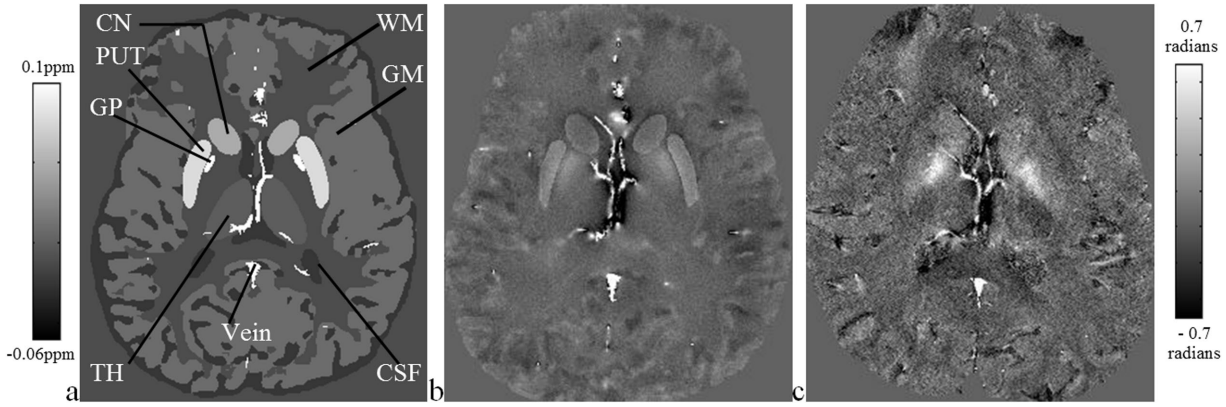


FIG. 3. **a:** A transverse view of the 3D brain model. **b:** The simulated phase map from the model using parameters: $B_0 = 3$ T and $T_E = 18$ ms which are consistent with imaging parameters in the real data (**c**). Images (**b**) and (**c**) have the same window level setting.

are around 0.40 ± 0.01 ppm for all SMs. The background noise levels, (i.e., standard deviation of the susceptibility values) measured from a region outside the streaking artifact in SM using Ref. 18 are around 1/2 to 2/3 of the background noise levels in SMs using Refs. 11,15 with $\text{thr} = 0.06, 0.07$, and 0.1 , which are the optimal threshold values suggested in Refs. 11,12,18. Given this result, the method in (18) was chosen to generate a $\chi_{i=0}(r)$ map.

Finding an Optimal Threshold Value

To find the optimal threshold, a series of $\chi(r)$ maps were reconstructed by the iterative method using threshold values a of $0.01, 0.03, 0.07, 0.1, 0.15, 0.2, 0.25$, and 0.3 . The larger this threshold, the closer the final estimate for $\chi(r)$ will be to $\chi_{\text{vm}}(r)$. The optimal threshold value was found by comparing the accuracy of the estimated susceptibility values as well as the effects on reducing streaking artifacts in the reconstructed $\chi(r)$ maps. To study the effect of noise in $\chi(r)$ maps due to the noise in phase images, complex datasets for cylinders of diameter 2, 4, 8, 32 voxels, respectively, were simulated with Gaussian noise added to both real and imaginary channels. Noise was added in the complex images to simulate a $\text{SNR}_{\text{magnitude}}$ of 40:1, 20:1, 10:1, and 5:1 in the magnitude images. Since $\sigma_{\text{phase}} = 1/\text{SNR}_{\text{magnitude}}$, this corresponds to $\sigma_{\text{phase}} = 0.025, 0.05, 0.1$, and 0.2 radian.

To estimate the improvement in the SM by the iterative method, we used a root mean squared error (RMSE) to measure streaking artifacts outside the cylinder. Background noise in the SM is measured in a region away from all major sources of streaking artifacts to compare the noise measured in the phase image (i.e., so we can correlate noise in the phase with the expected noise enhancement from the inversion process).

Effect of High-Pass Filter

The effect of high-pass (HP) filtering the phase data on the $\chi(r)$ map generated by the iterative method was also studied. Phase images of a cylindrical geometry with diameters of 2, 4, 8, 16, 32, and 64 voxels were simulated. Homodyne HP filters (33) with a 2D hanning filter (full width at half-maximum, FWHM = 4, 8, 16, and 32 pixels) were applied on these phase images in both in-

plane directions. SM reconstructions were stopped based on the criteria in step 7 of the iterative process.

Three Dimensional Brain Model Simulations

To address the potential of the iterative technique to improve the SM of general structures such as the basal ganglia, a 3D model of the brain was created including the: red nucleus (RN), substantia nigra (SN), crus cerebri (CC), thalamus (TH), caudate nucleus (CN), putamen (PUT), globus pallidus (GP), gray matter (GM), white matter (WM), cerebrospinal fluid (CSF), and the major vessels (34). The structures in the 3D brain model were extracted from two human 3D T_1 weighted and T_2 weighted data sets. Basal ganglia and vessels are from one person; GM and WM are from the other person's data set. Since all structures are from in vivo human data sets, this brain model represents realistic shapes and positions of the structures in the brain. Susceptibility values in parts per million (ppm) for the structures SN, RN, PUT, and GP, were taken from Ref. 12 and others were from measuring the mean susceptibility value in a particular region from SMs using Ref. 18 from in vivo human data: RN = 0.13, SN = 0.16, CC = -0.03, TH = 0.01, CN = 0.06, PUT = 0.09, GP = 0.18, vessels = 0.45, GM = 0.02, CSF = -0.014, and WM = 0. All structures were set inside a $512 \times 512 \times 256$ matrix of zeros. The phase of the 3D brain model was created by applying the forward method (8,26,27,30) to the 3D brain model with different susceptibility distributions using the imaging parameters: $T_E = 5$ ms and $B_0 = 3$ T. A comparison between the phase maps from this brain model and a real data set is shown in Fig. 3. To match the imaging parameters of the real data set, $B_0 = 3$ T and $T_E = 18$ ms were applied for the results presented in Fig. 3. Except for Fig. 3, all other figures in the paper associated with the 3D brain were simulated by using $T_E = 5$ ms.

In Vivo MR Data Collection and Processing

A standard high-resolution 3D gradient echo SWI sequence was used for data acquisition. A transverse 0.5 mm isotropic resolution brain dataset was collected at 3 T from a 23-year-old healthy volunteer. The sequence parameters were: TR = 26 ms, flip angle = 15° , read

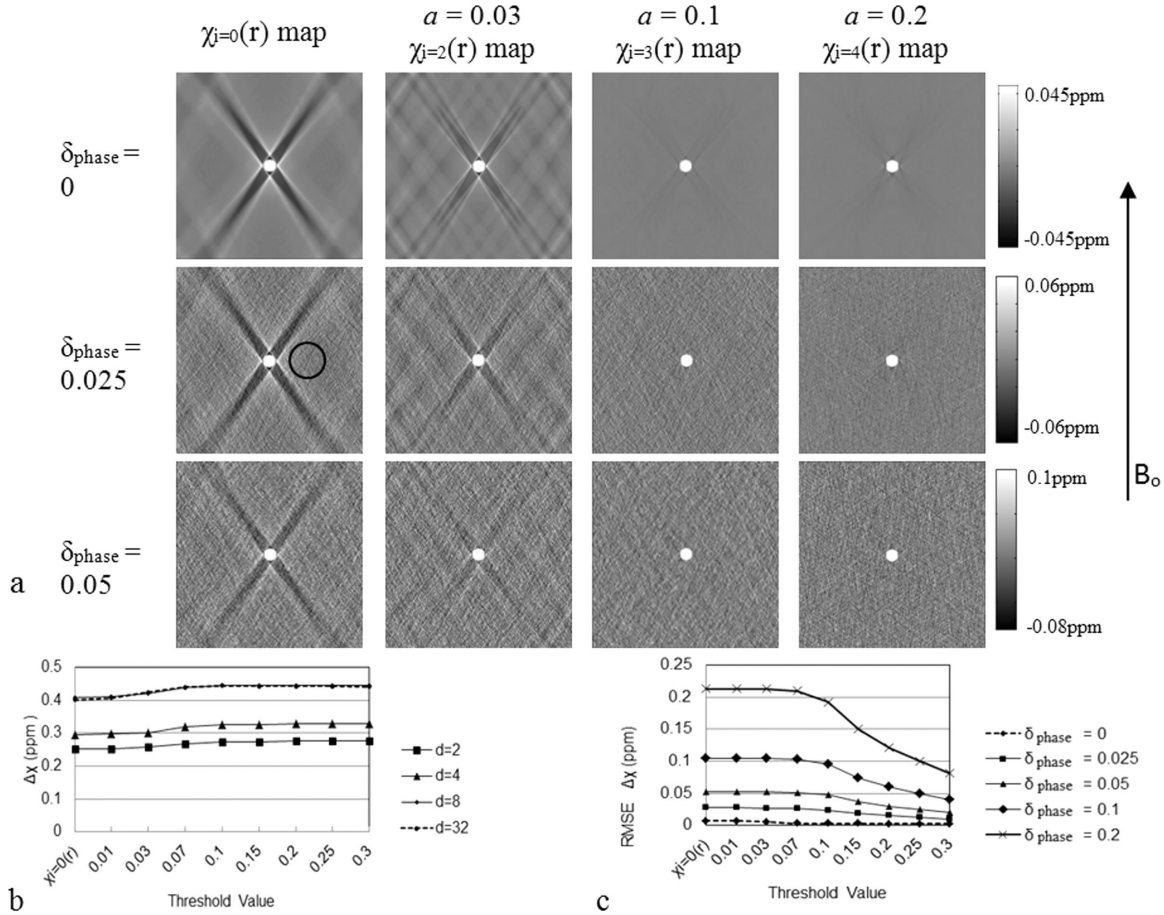


FIG. 4. Simulations showing the comparison of the calculated susceptibility distributions for a cylinder perpendicular to B_0 at different threshold values (a) applied to $g(k)$ as well as the initial $\chi_{i=0}(r)$ map. The direction of B_0 is indicated by a black long arrow. The susceptibility, $\Delta\chi$, inside the cylinder is 0.45 ppm. **a:** The comparison of the converged $\chi_{i=b}(r)$ map with the $\chi_{i=0}(r)$ map for a diameter of 32-pixel cylinder, where b is the iterative step required to reach convergence. In this data, $b = 2$ when $a = 0.03$, $b = 3$ when $a = 0.1$ and $b = 4$ when $a = 0.2$ when $\sigma_{\text{phase}} = 0$. The top row of images shows simulations with no phase noise. The second and the third row show simulations with added phase noises $\sigma_{\text{phase}} = 0.025$ and 0.05 radian, respectively. The first column of images show initial $\chi_{i=0}(r)$ maps for reference. **b:** The variation of the mean calculated susceptibility inside the cylinder with different threshold value, a , for diameter (d) = 2, 4, 8, and 32 pixels cylinders. The mean susceptibility value is independent of the noise level; therefore, only mean values from $\sigma_{\text{phase}} = 0$ were provided. **c:** The variation of the RMSE of the susceptibility values outside the cylinder as a function of the threshold value, a , and the noise level. The $d = 32$ pixels cylinder was used to generate (c). The range of the gray-scale bars is chosen to highlight the artifacts in the images. It does not reflect the quantified higher susceptibility values inside cylinders.

bandwidth = 121 Hz/pixel, $T_E = 14.3$ ms, 192 slices, and a matrix size of 512×368 . To reconstruct $\chi_{i=0}(r)$ with minimal artifacts, the following steps were carried out:

1. The unwanted background phase variations were removed using either: (a) a homodyne HP filter (FWHM = 16 pixels) (33) or (b) Prelude in FMRIB Software Library (FSL) (35) to unwrap the phase, followed by the process of Sophisticated Harmonic Artifact Reduction for Phase data (SHARP) (36) with a filter radius of 6 pixels. To reduce artifacts in the calculated SMs, regions with the highest phase deviations due to air/tissue interfaces were removed manually from the HP filtered phase images and the phase in those regions were set to zero.
2. A complex threshold approach (37) was used to separate the brain from the skull.
3. The phase image with an original matrix size of $512 \times 368 \times 192$ was zero filled to $512 \times 512 \times 256$ to

increase the field-of-view and to avoid streaking artifacts caused by the edge of brain to alias back to the reconstructed SM.

4. The regularized inverse filter, $g_{\text{reg}}^{-1}(k)$ (18) was applied to obtain $\chi_{i=0}(r)$, followed by the iterative process using $a = 0.1$. For in vivo data, the iterative program was terminated at the third iterative step.

RESULTS

Selection of Threshold Level Based on Simulations

To find the optimal threshold value, SMs were reconstructed using $a = 0.01, 0.03, 0.07, 0.1, 0.15, 0.2, 0.25$, and 0.3 , respectively, with different noise levels (Fig. 4). The streaking artifacts shown in $\chi_{i=0}(r)$ (the first column in Fig. 4a) have been significantly reduced by the iterative method and fall below the noise level when $a \geq 0.1$. Also, when $a \geq 0.1$, the mean susceptibility value

inside the cylinder was found to increase to 0.44 ppm when the diameter of the cylinder was larger than 8 pixels (Fig. 4b) and this trend is independent of the object size and the noise in the phase image. The optimal result in terms of obtaining the true susceptibility value was with a threshold of 0.1. Figure 4c shows a plot of RMSE of the susceptibility values from the whole region outside the 32-pixel cylinder using different a . The RMSE of the susceptibility values decreases as a increases. Therefore, for vessels, a value of $a = 0.3$ would be the optimal value. However, a large threshold value means replacing more original k-space with the k-space only consisting of vessel information which will reduce the signals from other brain structures and blur these structures. Since the SM using $a = 0.1$ already reveals the optimal susceptibility value for the vessels and an acceptable RMSE, it is appropriate to choose 0.1 for more general applications to study the entire brain.

Figure 4a compares the converged $\chi_{i=b}(r)$ map with the $\chi_{i=0}(r)$ map, where b is the iterative step required to reach convergence. In this data, $b = 2$ when $a = 0.01$ and 0.03 , $b = 3$ when $a = 0.07$, 0.1 , and 0.15 and $b = 4$ when $a = 0.2$, 0.25 , and 0.3 for $\sigma_{\text{phase}} = 0$. When σ_{phase} increases, more iterative steps were required to reach convergence. For instance, the maximum iterative step number is 9 when $\sigma_{\text{phase}} = 0.2$ radians. Using a noise level of 0.025 radian in the phase image as an example, $\sigma_{\text{reg}}^{-1}(k)$ (18) leads to a susceptibility noise of roughly 0.025 ppm in the $\chi_{i=0}(r)$ map. The iterative approach leads to a slight decrease in background noise, 0.021 ppm, in $\chi_{i=3}(r)$ map when $a = 0.1$. The background noise was measured in a region outside the streaking artifact indicated by the black circle in Fig. 4a. The overall decrease in RMSE in the background (Fig. 4c) is a consequence of both a decrease in streaking artifacts and a reduction in thermal noise contribution.

Selection of the Optimal Iterative Step

The inverse process (18) was applied to the dipole field in Fig. 5a to give the $\chi_{i=0}(r)$ map shown in Fig. 5b; prominent streaking artifacts are evident in this image. Streaking artifacts are significantly reduced at each step of the iterative method quickly reaching convergence (Fig. 5c–e). The largest improvement is seen in the first iterative step, which is verified by Fig. 5f, showing the difference between Fig. 5c ($\chi_{i=1}(r)$ map) and Fig. 5b ($\chi_{i=0}(r)$ map). After the second iteration, we can see some minor streaking reductions (Fig. 5g, the difference between the $\chi_{i=1}(r)$ map and $\chi_{i=2}(r)$ map). The mean susceptibility value approaches 0.44 ppm in a single step. Similar results (not shown) are also obtained when the iterative method is run with different aspect ratios between the in-plane resolution and the through plane resolution (such as 1:2 and 1:4). The iterative results always lead to higher final susceptibility values compared to the initial value in $\chi_{i=0}(r)$. Finally, even when an HP filter is applied, up to a 10% increase in the susceptibility is realized (Fig. 5i). The SMs of large vessels benefit from a low order HP filter (FWHM = 4 pixels) and small vessels up to 8 pixels benefit from a HP filter (FWHM = 16 pixels).

Effect of the Iterative Approach on Surrounding Brain Tissues in the 3D Brain Model

SM Reconstruction Using a Vessel Mask Only

Figure 6a,d represents $\chi_{i=0}(r)$, without noise and with 0.025 radians of noise in phase images. Figure 6f is the vessel map. Streaking artifacts (delineated by the black arrows) are obvious in Fig. 6a,d and significantly reduced in the $\chi_{i=3}(r)$ maps (Fig. 6b,e) using $a = 0.1$. Figure 6c is the $\chi_{i=3}(r)$ map using $a = 0.2$. As can be seen, when a increases, the iterative method still works for vessels, but brain tissues become more blurred. Figure 7a plots the mean susceptibility values inside the vessel (vein of Galen), GP, SN, RN, PUT, and CN from $\chi_{i=3}(r)$ maps generated by using $a = 0.1, 0.15, 0.2, 0.25$, and 0.3 , respectively. The susceptibility value in the brain model and $\chi_{i=0}(r)$ map are also provided in the plot as references. Generally, the susceptibility values of brain tissues except vessels decrease as a increases while, for vessels, the susceptibility value is 0.41 ppm in the $\chi_{i=0}(r)$ map and is increased to 0.45 ppm in the $\chi_{i=3}(r)$ maps.

SM Reconstruction Using a Mask Including Vessels and Brain Structures

The iterative method is not limited to improving SM from just vessels; it can also be applied to the entire brain. Figure 6g shows a coronal view of the $\chi_{i=0}(r)$ map for the brain model. The $\chi_{i=3}(r)$ map using a mask keeping all major structures (GP, SN, RN, PUT, CN) and vessels is shown in Fig. 6h. In practice, this is equivalent to setting thresholds in the $\chi_{i=0}(r)$ map to be greater than 0.09 ppm to extract all these high susceptibility structures from the $\chi_{i=0}(r)$ map to create the mask. Figure 6h reveals that streaking artifacts associated with veins as well as all major structures have been reduced. Figure 6i shows the difference between Fig. 6g, h. In addition, streaking artifacts sometimes cause the appearance of “false” structures. For instance, there is no internal capsule (IC) included in the model (Fig. 6l), yet we see an IC like structure in the $\chi_{i=0}(r)$ map (Fig. 6j) (indicated by a dashed white arrow in Fig. 6j). The iterative method removes the streaking artifacts and the “false” IC (Fig. 6k). Figure 7b shows susceptibility values in each structure in the brain model for $\chi_{i=0}(r)$ and $\chi_{i=3}(r)$ when the mask includes vessels and all major structures. The underestimated susceptibility values of all major structures and vessels in the $\chi_{i=0}(r)$ map have been recovered by the iterative method in the $\chi_{i=3}(r)$ map.

Effect of Errors in the Vessel Map

Accurately extracting vessels from $\chi_{i=0}(r)$ is critical for the iterative method. Figure 8b–d and the corresponding enlarged views (Fig. 8f–h) from the rectangular region indicated in Fig. 8a show the $\chi_{i=3}(r)$ maps using an accurate (Fig. 8j), a dilated (Fig. 8k), and an eroded (Fig. 8l) vessel map to show the effect of errors in the vessel mask on the $\chi_{i=3}(r)$ map. The dilated and eroded vessel maps were generated using Matlab functions based on a 3-by-3 square structuring element object. The susceptibility values measured from a vein indicated by the white arrow in Fig. 8e are 0.40 ± 0.03 ppm (Fig. 8e),

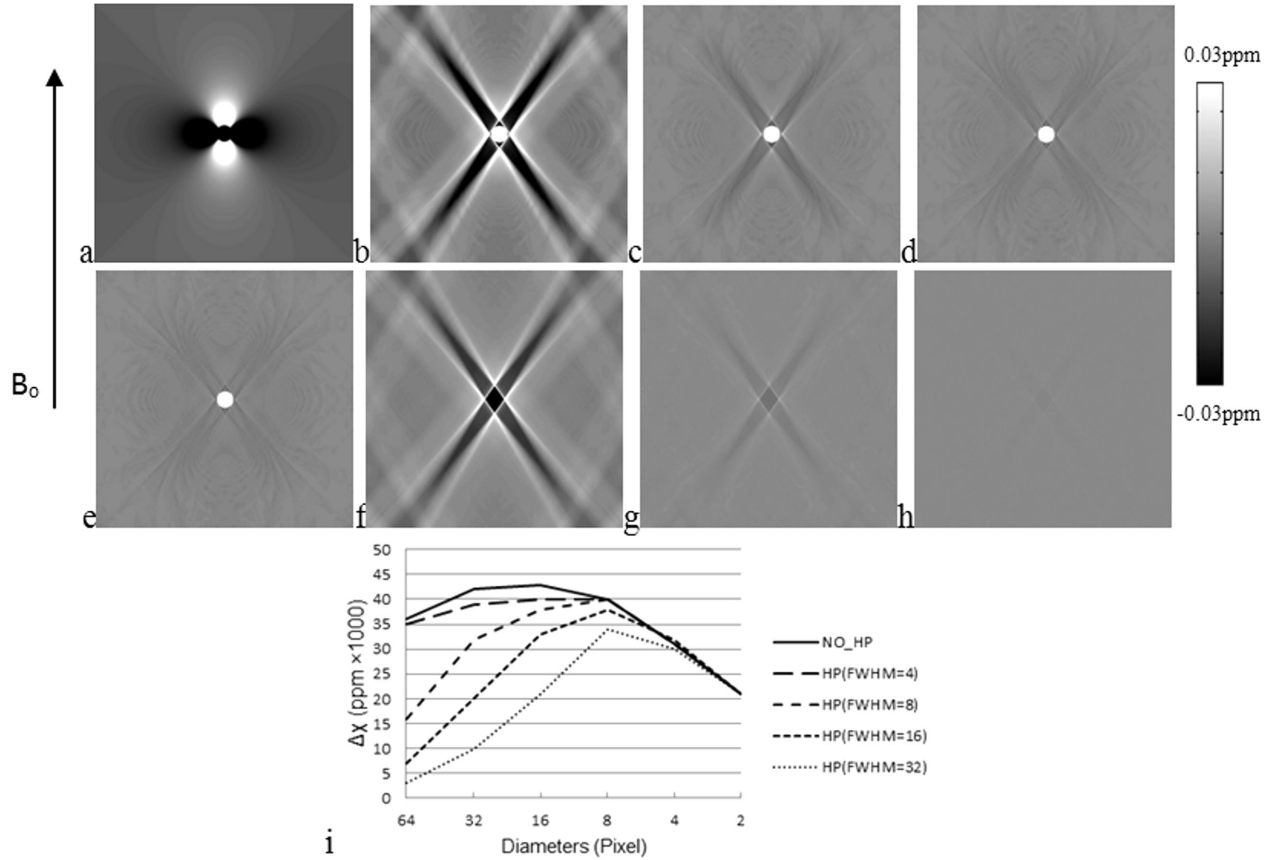


FIG. 5. **a**: Phase images from a cylinder with a diameter of 32 pixels are simulated with: $\Delta\chi = 0.45$ ppm, $B_0 = 3$ T, and $T_E = 5$ ms. The cylinder is perpendicular to the main field. No thermal noise was added in these images. **b**: The initial $\chi_{i=0}(r)$ map. **c**: The SM from the first iteration, $\chi_{i=1}(r)$ map, **(d)** $\chi_{i=2}(r)$ map and **(e)** $\chi_{i=3}(r)$ map using threshold value $\alpha = 0.1$. The SM has converged at $\chi_{i=3}(r)$ map. The streaking artifacts are reduced as the number of iterative steps increases. **f**: The difference image of (c) subtracted from (b) illustrates that the streaking artifacts were reduced by the iterative procedure and the largest improvement happens in this first iterative step. **g**: The difference image of the $\chi_{i=1}(r)$ map subtracted from the $\chi_{i=2}(r)$ map indicates that the streaking artifacts were further reduced by the second iterative step. **h**: The difference image of $\chi_{i=2}(r)$ map subtracted from $\chi_{i=3}(r)$ map shows much less improvement at the third iterative step. Thus it indicates a convergence of the iterative procedure. All images were set to the same window level setting for direct comparisons and for enhancing the presence of the streaking and the remnant error. **i**: The effect of the iterative approach on the changes in susceptibility values from HP filtered phase images. Differences between the values in iterative and non-iterative susceptibility map reconstruction (i.e., $\chi_{\text{converged}}(r) - \chi_{i=0}(r)$) from HP filtered phase images are plotted for different filter sizes. Results for four filter sizes (FWHM = 4, 8, 16, and 32 pixels) are shown here. Applying an HP filter leads to an underestimation of $\Delta\chi$ (18). The iterative approach helps to improve the accuracy of the estimated susceptibility values. The range of the gray-scale bars is chosen to highlight the artifacts in the images. It does not reflect the quantified higher susceptibility values inside cylinders.

0.45 ± 0.03 ppm (Fig. 8f), 0.45 ± 0.03 ppm (Fig. 8g), and 0.40 ± 0.07 ppm (Fig. 8h), respectively. The iterative method still works if the vessel is slightly enlarged but does little to change the original $\chi_{i=0}(r)$ map if the vessels are too small or absent in the mask. As we just discussed, streaking artifacts produced “false” vessels indicated by the dashed black arrow in Fig. 8e since these vessels are not in the model (Fig. 8i). These false vessels disappeared in Fig. 8f.

Results from the In Vivo Dataset

In the in vivo example, we compare the differences between SHARP (Fig. 9a–d) and a homodyne HP filter (FWHM = 16 pixels) (Fig. 9e–h). Compared to the transverse view, streaking artifacts are more obvious in the sagittal or coronal view. Figure 9a shows the $\chi_{i=0}(r)$ map with severe streaking artifacts. The streaking artifacts

were significantly reduced in the $\chi_{i=3}(r)$ map (Fig. 9b) using $\alpha = 0.1$. The streaking artifacts associated with the superior sagittal sinus vein (indicated by two black arrows in Fig. 9a) were significantly decreased in Fig. 9b,d. The subtracted image (Fig. 9c), Fig. 9a minus Fig. 9b, reveals the removed streaking artifacts. These streaking artifacts are one of the reasons why the $\chi_{i=0}(r)$ maps appear noisy. In the $\chi_{i=3}(r)$ map, the reduction in streaking artifacts from individual veins leads to a decrease of noise therefore an increased SNR of veins. If veins are the only interest, even a threshold of 0.2 can work reasonably well (Fig. 9d). Two relatively big veins, V1 and V2, indicated by the white dashed and white solid arrows, respectively, in Fig. 9b, were chosen to measure the susceptibility values. Results are provided in Table 1. The susceptibility values of these two veins have been improved by roughly 16% by the iterative method. The standard deviation of the susceptibility values measured

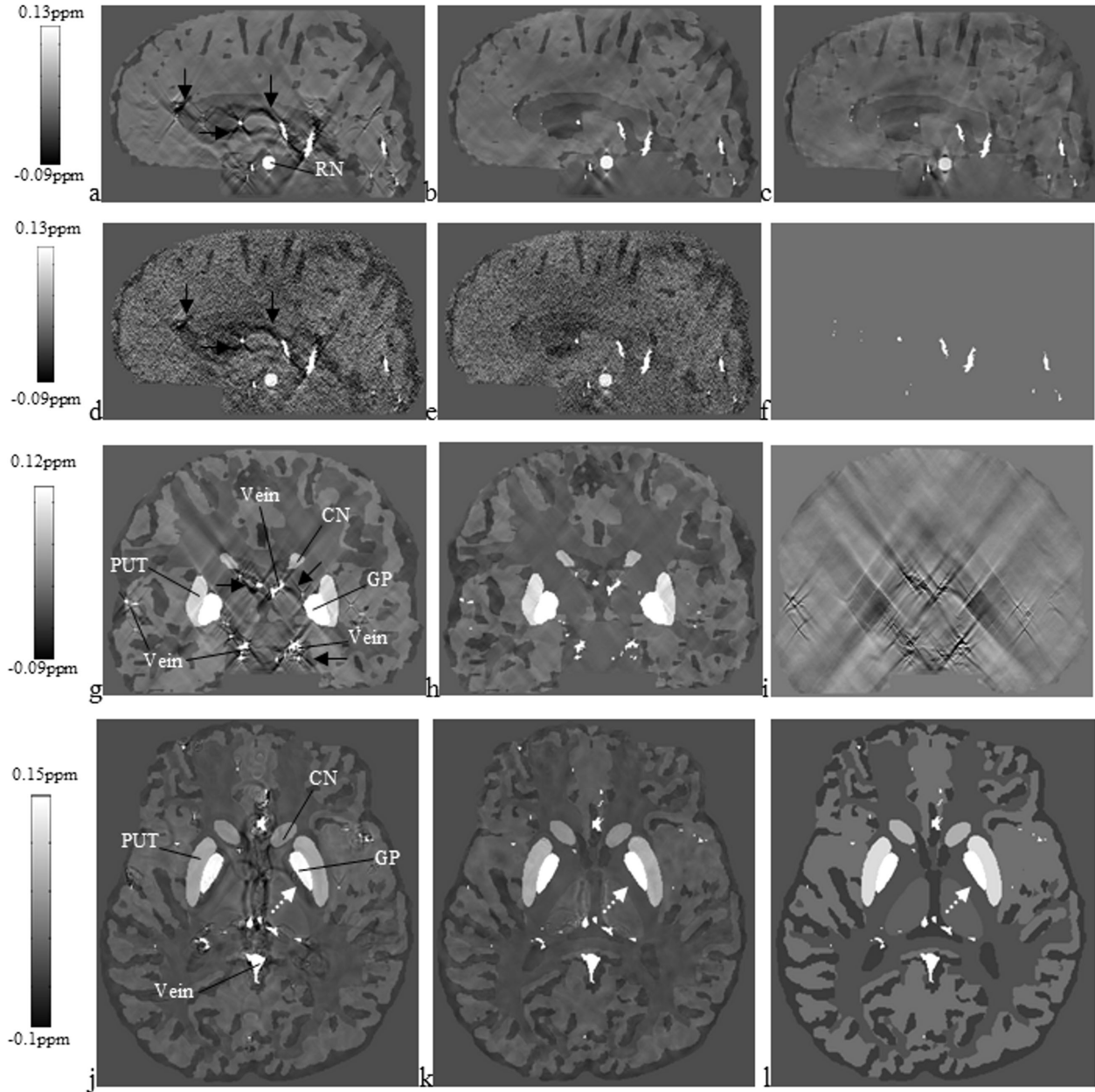


FIG. 6. Results before and after the iterative method using a region of interest map which consists of either only vessels or specific brain structures (in this case the basal ganglia) plus vessels. **a**: The initial $\chi_{i=0}(r)$ map without noise added in the original simulated images. **b**: $\chi_{i=3}(r)$ map of (a) using threshold value $\alpha = 0.1$. **c**: Similar to (b), $\alpha = 0.2$. **d**: The initial $\chi_{i=0}(r)$ map with noise added in original images, resulting a standard deviation of 0.025 radian in phase images. **e**: $\chi_{i=3}(r)$ map of (d) using $\alpha = 0.1$. **f**: The associated vessel map. **g**: The $\chi_{i=0}(r)$ map in the coronal plane as a reference. The streaking artifacts are clearly shown in every structure. **h**: The $\chi_{i=3}(r)$ maps created by using a region of interest map which consists of GP, SN, RN, PUT, CN, and vessels. **i**: The difference image of (g) and (h). **j**: The initial $\chi_{i=0}(r)$ map in the transverse plane has “false” internal capsule (IC) (pointed by an arrow) around GP; **k**: The $\chi_{i=3}(r)$ map shows no “IC.” This matches the originally simulated model (l). No noises were added to images from (g) to (l).

from a uniform region inside the WM decreased from 0.042 ppm in $\chi_{i=0}(r)$ map to 0.035 ppm and 0.023 ppm in the $\chi_{i=3}(r)$ map with $\alpha = 0.1$ and 0.2, respectively. The baseline susceptibilities of the major structures are higher with SHARP than with the HP filter. The iterative method works for brain structures too when the structure is included in the mask. For instance, the mean susceptibility values of the GP and SN have been increased from 0.155 ± 0.058 ppm and 0.162 ± 0.067 ppm in the $\chi_{i=0}(r)$

map to 0.163 ± 0.070 ppm and 0.186 ± 0.083 ppm in the $\chi_{i=3}(r)$ map, from the dataset processed using SHARP. The result after HP filtering (Fig. 9e) shows more edge artifacts indicated by the left arrow in Fig. 9e. Much of this error was reduced by the iterative method (Fig. 9f). It seems that the iterative method compensated for the worse first guess (Fig. 9e) and ended up with almost the same result (Fig. 9f,h) as having started with SHARP (Fig. 9b,d) from the image perspective. Since a

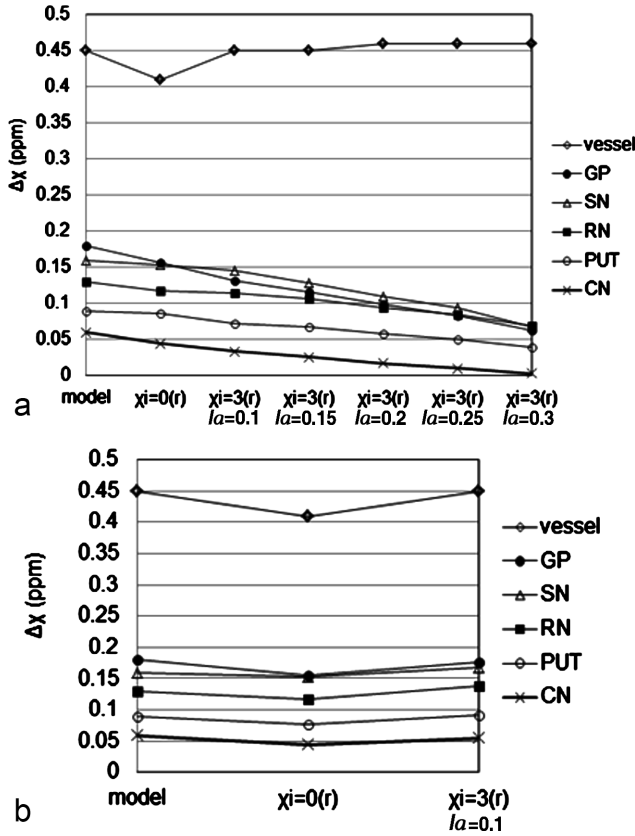


FIG. 7. The plots of mean susceptibility values inside the vessel (vein of Galen), GP, SN, RN, PUT, and CN from $\chi_{i=3}(r)$ maps. The first two data points of each curve is the value inside each structure from the brain model and the $\chi_{i=0}(r)$ map, respectively. **a:** $\chi_{i=3}(r)$ maps generated by applying a region of interest map which consists only vessels using $\alpha = 0.1, 0.15, 0.2, 0.25$, and 0.3 , respectively. **b:** $\chi_{i=3}(r)$ maps generated by applying a region of interest map which consists of the GP, SN, RN, PUT, CN, and vessels using $\alpha = 0.1$.

small sized HP filter cannot remove rapid phase wrapping at air-tissue interfaces; we had to cut out the region near the sinuses in the phase images.

DISCUSSION

In this article, a threshold-based k-space/image domain iterative approach has been presented. Simulations and in vivo results show that the ill-posed problems of streaking artifacts and biases in the estimates of susceptibilities can be significantly reduced. The replacement of the $\chi(k)$ values near the singularities by $\chi_{vm}(k)$, which is obtained from the geometric information from the $\chi(r)$ map itself, obviates many of the current problems seen in the TBSO methods. Since $\chi_{vm}(r)$ contains little streaking artifacts itself, the values used inside the thresholded regions in $\chi(k)$ now contain no artifact either. In this sense, we obtain an almost perfect k-space without bad data points in the region of singularities. This explains why this method converges quickly and the major improvement is in the first iterative step (Fig. 5).

The proposed iterative approach is different from the other threshold-based methods (11,15,18,19,24) which fill a predefined conical region using a constant, zero or 1/thr threshold (11,15,24) or the first-order derivative of $g^{-1}(k)$ (19). The iterative method uses full geometry information from the SM (vessels or predefined structures and not edge information) to iteratively change k-space values in the conical region using the forward model. This is also quite different than other currently proposed solutions (9,12,20,22). Even though spatial priors such as gradients of the magnitude are used (9,12,20,22), in those methods, the meaningful values of the singularity regions in k-space are obtained through solving the complex cost function problem. However, the iterative method uses priors not from the magnitude image but from the SM. The missing data in the singularity regions are obtained through iterating back and forth between

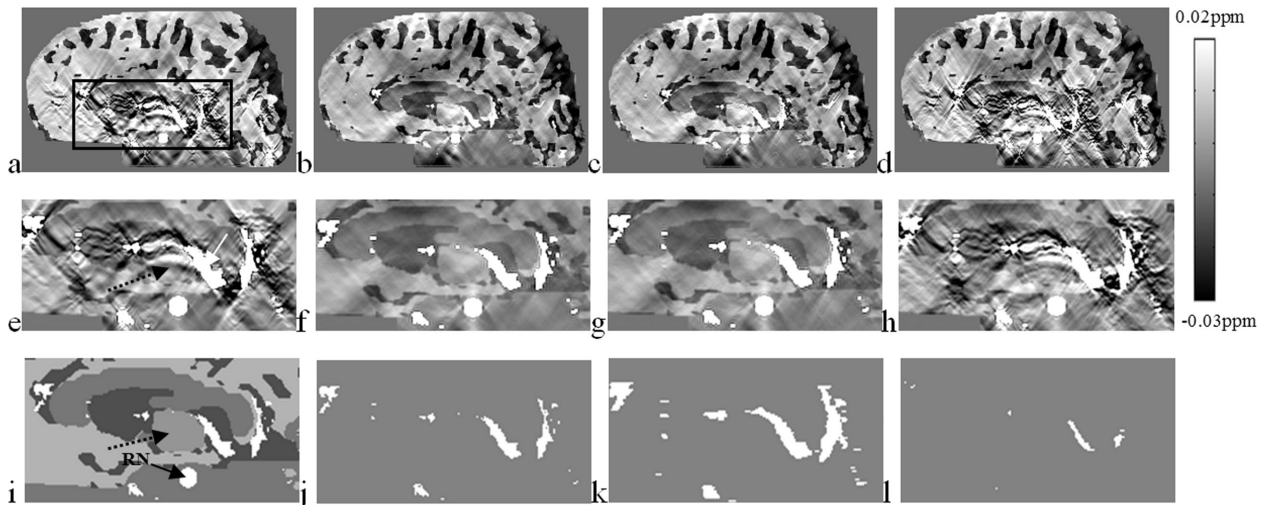


FIG. 8. Comparison of the reconstructed $\chi_{i=3}(r)$ maps using (j) accurate, (k) dilated, and (l) eroded vessel maps. Their corresponding vessel maps and the enlarged views from the rectangular regions are provided in (b)–(d) and (f)–(h). (a) and (e) The initial $\chi_{i=0}(r)$ maps and (i) the original brain model as references. The circle in the midbrain in the $\chi(r)$ maps represents the RN and is indicated by a black arrow in (i). Other hyper-intense regions in SMs are vessels.

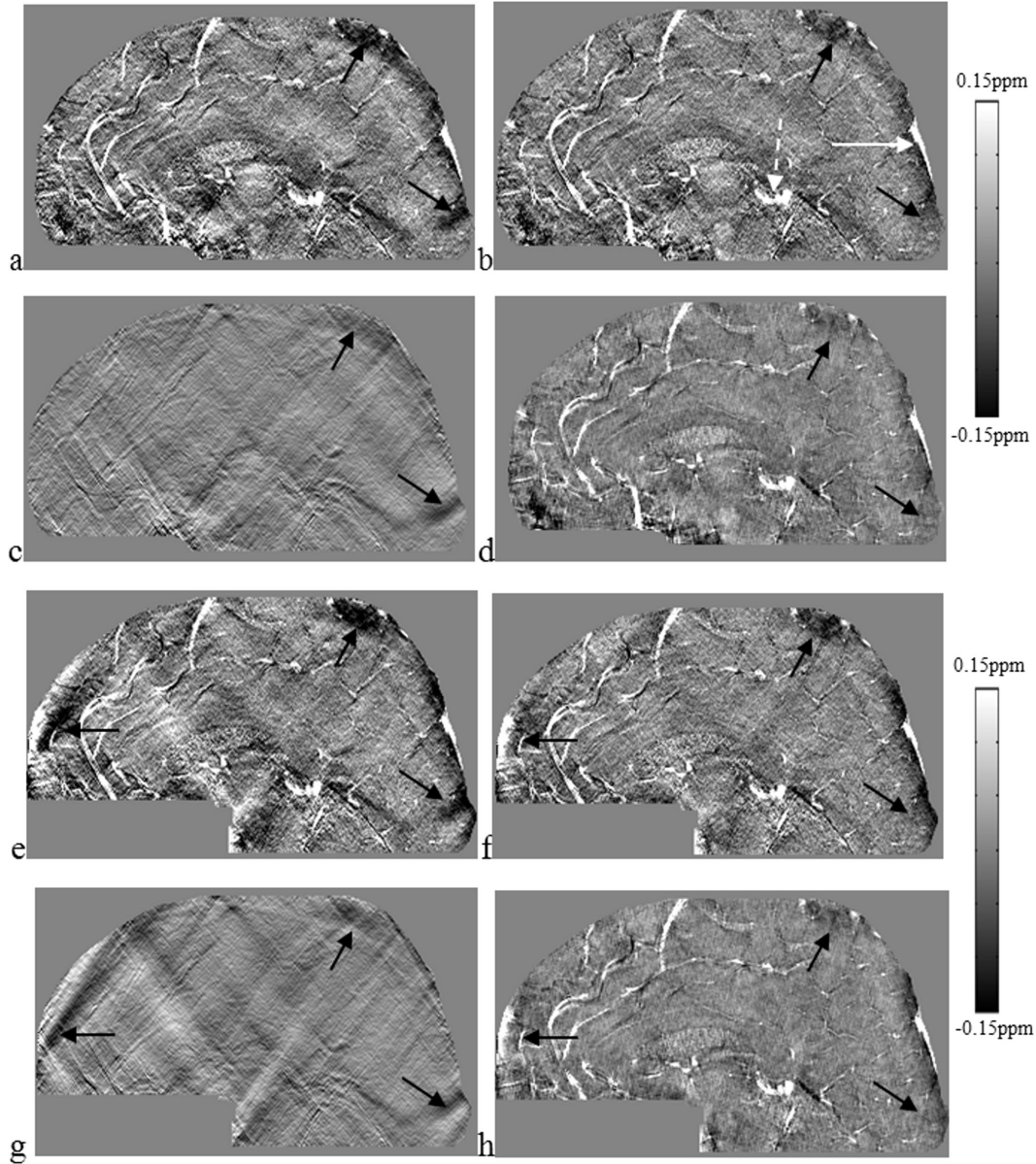


FIG. 9. Comparisons of SMs using SHARP or a HP filter (FWHM = 16 pixels) to remove the background field. The iterative method with $a = 0.1$ and 0.2 is applied after the background is removed. (a)–(d) and (e)–(h) are results after the application of SHARP and the HP filter, respectively. (a) and (e) the initial $\chi_{i=0}(r)$ maps. (b) and (f) the $\chi_{i=3}(r)$ maps generated from the iterative method with $a = 0.1$. (c) and (g) the differences of images between (a) and (b), and between (e) and (f), respectively. These two images show the successful reduction of the streaking artifacts. (d) and (h) the $\chi_{i=3}(r)$ maps generated from the iterative method with $a = 0.2$. The range of the gray-scale bars is chosen to highlight the artifacts in the images. It does not reflect the quantified susceptibility values inside veins.

the SMs and their k-space. The advantage of cost function approaches is that they do not need to predefine the singularity region in k-space which is solved by the optimization process automatically (although the optimization process itself is usually quite time-consuming). On the other hand, the iterative method is the most time-efficient. It is fast enough to reconstruct SMs for a $512 \times 512 \times 256$ data set using an Intel Core i7 CPU 3.4 GHz processor in less than 30 s, since in practice usually three iterations are good enough to generate decent results.

The threshold value also plays a key role. A threshold value of 0.1 is a reasonable choice since a lower threshold value leads to an increase in noise and a higher

threshold value leads to a blurring of the object (Figs. 6c, 9d, h).

It is known that the ill-posedness of the inverse filter will increase the noise level from the phase to the SM. Based on both simulations and real data, we find that there is a factor of 4 increase in noise in the SM relative to the original phase data. This result and the fact at $B_0 = 3$ T, $T_E = 5$ ms, and $\sigma_{\chi_{i=0}(r)} = 0.025$ ppm make it possible to write the total noise in the background region in $\chi_{i=0}(r)$ as $0.025 \cdot 4 \cdot (3/B_0) \cdot (5/T_E)$ in ppm. The noise in $\chi_{i=3}(r)$ will be less than this value since the iterative method will reduce streaking artifact in SM.

The iterative method can be used to remove streaking artifacts associated with not only vessels but also other

Table 1
 $\Delta\chi$ Measured *In Vivo* in Two Veins in $\chi_{i=0}$ (*r*) Maps and $\chi_{i=3}$ (*r*) Maps With Different Threshold Values

	$\chi_{i=0}$ (<i>r</i>) map	$\chi_{i=3}$ (<i>r</i>) map/ $a = 0.1$	$\chi_{i=3}$ (<i>r</i>) map/ $a = 0.2$
V1 (SHARP)	0.32 ± 0.07	0.37 ± 0.08	0.38 ± 0.09
V1 (HP)	0.24 ± 0.05	0.28 ± 0.06	0.28 ± 0.06
V2 (SHARP)	0.35 ± 0.04	0.40 ± 0.05	0.41 ± 0.05
V2 (HP)	0.25 ± 0.05	0.31 ± 0.06	0.30 ± 0.06

Mean and standard deviation for the susceptibility values (in ppm) of two veins processed using SHARP and a HP filter (FWHM = 16 pixels), respectively, were chosen from the 0.5 mm isotropic resolution data. V1 and V2 are shown in Fig. 9. The susceptibility values of these two veins have been increased by the iterative method. There is not much variation of the susceptibility value with different threshold values.

brain structures as well. Figure 6h shows a reduction in artifacts associated specifically with iron-rich regions such as the GP and CN.

Accurately extracting vessels from the $\chi_{i=0}$ (*r*) map is critical for the iterative method (Fig. 8). In this study, vessels were segmented directly from the SM (Fig. 2). It may also possible to segment veins from original magnitude images [9,12,20,22], phase images, and/or SWI images. Extraction of accurate anatomic information from phase data sometimes is difficult since phase is orientation dependent and phase changes are generally nonlocal. SWI images work better for an anisotropic dataset rather than an isotropic dataset since phase cancellation is needed to highlight vessel information. Therefore, we may consider combining SMs with magnitude images, phase images, and/or SWI images together to segment the veins, since different types of images can compensate for missing information.

The iterative method appears to help even in the presence of non-isotropic resolution with partial volume effects and to a minor degree when an HP filter is applied. A smaller sized HP filter would be better, since a larger HP filter will significantly underestimate the susceptibility value (Table 1). SHARP gave us better results compared with the HP filter (FWHM = 16 pixels) (Fig. 9), but SHARP requires phase unwrapping which can be time consuming and is noise dependent [19]. From this perspective, an HP filter has the advantage since it does not need unwrapped phase. If the forward modeling approach of Neelavalli et al. [38] can be used to reduce air/tissue interface fields, then it may be possible to use a small size HP filter (FWHM = 8 pixels) which may provide similar results to SHARP.

Severe streaking artifacts associated with structures having high susceptibility values such as veins can lead to major changes in the appearance of the brain structures with low susceptibility. Practically, the susceptibility of the veins is a factor of 2.5–20 times higher than other structures in the brain. Therefore, even a 10% streaking artifact can overwhelm the information in the rest of the brain and create false appearing structures as in (Fig. 6j) and in (Fig. 8e). The reduction of these artifacts makes a dramatic difference in the ability to properly extract the susceptibility of other tissues.

In conclusion, both simulations and human studies have demonstrated that the proposed iterative approach can dramatically reduce streaking artifacts and improve the accuracy of susceptibility quantification inside the structures of interest such as veins or other brain tissues. Given its relatively fast processing time, it should be possible to expand its use into more daily clinical practice. With the improved accuracy of the susceptibility values inside veins, this method could be used potentially to improve quantification of venous oxygen saturation [18].

REFERENCES

- Haacke EM, Mittal S, Wu Z, Neelavalli J, Cheng YC. Susceptibility-weighted imaging: technical aspects and clinical applications, part 1. *AJNR Am J Neuroradiol* 2009;30:19–30.
- Mittal S, Wu Z, Neelavalli J, Haacke EM. Susceptibility-weighted imaging: technical aspects and clinical applications, part 2. *AJNR Am J Neuroradiol* 2009;30:232–252.
- Haacke EM, Reichenbach JR. *Susceptibility weighted imaging in MRI: basic concepts and clinical applications*. Hoboken, NJ: Wiley; 2011.
- Duyn JH, van Gelderen P, Li TQ, de Zwart JA, Koretsky AP, Fukunaga M. High-field MRI of brain cortical substructure based on signal phase. *Proc Natl Acad Sci USA* 2007;104:11796–11801.
- Haacke EM, Lai S, Yablonskiy DA, Lin W. In-vivo validation of the BOLD mechanism: a review of signal changes in gradient-echo functional MRI in the presence of flow. *Int J Imaging Syst Technol* 1995; 6:153–163.
- Rauscher A, Sedlacik J, Barth M, Mentzel HJ, Reichenbach JR. Magnetic susceptibility-weighted MR phase imaging of the human brain. *AJNR Am J Neuroradiol* 2005;26:736–742.
- Haacke EM, Cheng NY, House MJ, Liu Q, Neelavalli J, Ogg RJ, Khan A, Ayaz M, Kirsch W, Obenaus A. Imaging iron stores in the brain using magnetic resonance imaging. *Magn Reson Imaging* 2005;23:1–25.
- Koch KM, Papademetris X, Rothman DL, de Graaf RA. Rapid calculations of susceptibility-induced magnetostatic field perturbations for in vivo magnetic resonance. *Phys Med Biol* 2006;51: 6381–6402.
- de Rochefort L, Brown R, Prince MR, Wang Y. Quantitative MR susceptibility mapping using piece-wise constant regularized inversion of the magnetic field. *Magn Reson Med* 2008;60:1003–1009.
- Cheng YC, Neelavalli J, Haacke EM. Limitations of calculating field distributions and magnetic susceptibilities in MRI using a Fourier based method. *Phys Med Biol* 2009;54:1169–1189.
- Wharton S, Schafer A, Bowtell R. Susceptibility mapping in the human brain using threshold-based k-space division. *Magn Reson Med* 2010;63:1292–1304.
- Wharton S, Bowtell R. Whole-brain susceptibility mapping at high field: a comparison of multiple- and single-orientation methods. *Neuroimage* 2010;53:515–525.
- Schweser F, Deistung A, Lehr BW, Reichenbach JR. Differentiation between diamagnetic and paramagnetic cerebral lesions based on magnetic susceptibility mapping. *Med Phys* 2010;37:5165–5178.
- Kressler B, de Rochefort L, Liu T, Spincemaille P, Jiang Q, Wang Y. Nonlinear regularization for per voxel estimation of magnetic susceptibility distributions from MRI field maps. *IEEE Trans Med Imaging* 2010;29:273–281.
- Shmueli K, de Zwart JA, van Gelderen P, Li TQ, Dodd SJ, Duyn JH. Magnetic susceptibility mapping of brain tissue in vivo using MRI phase data. *Magn Reson Med* 2009;62:1510–1522.
- Schafer A, Wharton S, Gowland P, Bowtell R. Using magnetic field simulation to study susceptibility-related phase contrast in gradient echo MRI. *Neuroimage* 2009;48:126–137.
- Liu T, Spincemaille P, de Rochefort L, Kressler B, Wang Y. Calculation of susceptibility through multiple orientation sampling (COSMOS): a method for conditioning the inverse problem from measured magnetic field map to susceptibility source image in MRI. *Magn Reson Med* 2009;61:196–204.
- Haacke EM, Tang J, Neelavalli J, Cheng YC. Susceptibility mapping as a means to visualize veins and quantify oxygen saturation. *J Magn Reson Imaging* 2010;32:663–676.

19. Li W, Wu B, Liu C. Quantitative susceptibility mapping of human brain reflects spatial variation in tissue composition. *NeuroImage* 2011;55:1645–1656.
20. Liu T, Liu J, de Rochefort L, Spincemaille P, Khalidov I, Ledoux JR, Wang Y. Morphology enabled dipole inversion (MEDI) from a single-angle acquisition: comparison with COSMOS in human brain imaging. *Magn Reson Med* 2011;66:777–783.
21. Li L, Leigh JS. Quantifying arbitrary magnetic susceptibility distributions with MR. *Magn Reson Med* 2004;51:1077–1082.
22. de Rochefort L, Liu T, Kressler B, Liu J, Spincemaille P, Lebon V, Wu J, Wang Y. Quantitative susceptibility map reconstruction from MR phase data using bayesian regularization: validation and application to brain imaging. *Magn Reson Med* 2010;63:194–206.
23. Li Y, Xu N, Fitzpatrick JM, Morgan VL, Pickens DR, Dawant BM. Accounting for signal loss due to dephasing in the correction of distortions in gradient-echo EPI via nonrigid registration. *IEEE Trans Med Imaging* 2007;12:1698–1707.
24. Grabner G, Trattnig S, Barth M. Filtered deconvolution of a simulated and an in vivo phase model of the human brain. *J Magn Reson Imaging* 2010;32:289–297.
25. Deville G, Bernier M, Delrieux J. NMR multiple echoes observed in solid ^3He . *Phys Rev B* 1979;19:5666–5688.
26. Marques JP, Bowtell R. Application of a Fourier-based method for rapid calculation of field inhomogeneity due to spatial variation of magnetic susceptibility. *Concepts Magn Reson B Magn Reson Eng* 2005;25:65–78.
27. Salomir R, De Senneville BD, Moonen CTW. A fast calculation method for magnetic field inhomogeneity due to an arbitrary distribution of bulk susceptibility. *Concepts Magn Reson B Magn Reson Eng* 2003;19:26–34.
28. Hagberg GE, Welch EB, Greiser A. The sign convention for phase values on different vendor systems: definition and implications for susceptibility weighted imaging. *Magn Reson Imaging* 2010;28:297–300.
29. Demmel JW. Perturbation theory for the least squares problem. *Applied numerical linear algebra*. Berkeley, CA: SIAM; 1997. pp 117–118.
30. Hoffman RE. Measurement of magnetic susceptibility and calculation of shape factor of NMR samples. *J Magn Reson* 2006;178:237–247.
31. Spees WM, Yablonskiy DA, Oswood MC, Ackerman JJ. Water proton MR properties of human blood at 1.5 Tesla: magnetic susceptibility, $T(1)$, $T(2)$, $T^*(2)$, and non-Lorentzian signal behavior. *Magn Reson Med* 2001;45:533–542.
32. Haacke EM, Brown RW, Thomson MR, Venkatesan R. Magnetic resonance imaging. Physical principles and sequence design. New York: Wiley; 1999. 766 p.
33. Reichenbach JR, Venkatesan R, Schillinger DJ, Kido DK, Haacke EM. Small vessels in the human brain: MR venography with deoxyhemoglobin as an intrinsic contrast agent. *Radiology* 1997;204:272–277.
34. Buch S, Liu S, Neelavalli J, Haacke EM. Simulated 3D brain model to study the phase behavior of brain structures. In *Proceedings of the 20th Annual Meeting of ISMRM*, Melbourne, Australia, 2012. p. 2332.
35. Smith SM. Fast robust automated brain extraction. *Hum Brain Mapp* 2002;17:143–155.
36. Schweser F, Deistung A, Lehr BW, Reichenbach JR. Quantitative imaging of intrinsic magnetic tissue properties using MRI signal phase: an approach to in vivo brain iron metabolism? *Neuroimage* 2011;54:2789–2807.
37. Pandian DS, Ciulla C, Haacke EM, Jiang J, Ayaz M. Complex threshold method for identifying pixels that contain predominantly noise in magnetic resonance images. *J Magn Reson Imaging* 2008;28:727–735.
38. Neelavalli J, Cheng YCN, Jiang J, Haacke EM. Removing background phase variations in susceptibility weighted imaging using a fast, forward-field calculation. *J Magn Reson Imaging* 2009;29:937–948.

Original Research

Noncontrast-Enhanced Magnetic Resonance Angiography and Venography Imaging With Enhanced Angiography

Yongquan Ye, PhD,^{1*} Jiani Hu, PhD,¹ Dongmei Wu, MS,² and E. Mark Haacke, PhD^{1,3}

Purpose: To achieve simultaneous high-resolution magnetic resonance angiography and venography (MRV) imaging in terms of enhanced time-of-flight (TOF) angiography and susceptibility-weighted imaging (SWI), with a clear separation of arteries and veins.

Materials and Methods: A new flow rephase/dephase interleaved double-echo sequence was introduced that facilitates multiple types of imaging contrast, i.e., TOF, SWI, and dark blood, in a single acquisition. A nonlinear subtraction (NLS) method is proposed and assessed to maximally enhance angiography contrast with minimum venous contamination.

Results: Fully flow rephased TOF MRA and SWI MRV data were acquired simultaneously, along with an extra flow dephased dark blood image for angiography enhancement calculation. Compared to linear subtraction methods, the proposed NLS method was able to enhance angiography contrast while effectively eliminating vein-tissue contrast. The NLS method even outperformed low-dose contrast-enhanced MRA for a clean, enhanced angiography map.

Conclusion: Using the proposed interleaved double-echo sequence along with the NLS postprocessing method, one can simultaneously obtain both high-quality SWI and significantly enhanced TOF MRA with clear separation of arterial and venous maps.

Key Words: TOF MRA; SWI; MRV; nonlinear processing
J. Magn. Reson. Imaging 2013; 000:000–000.
 © 2013 Wiley Periodicals, Inc.

UNDERSTANDING THE CEREBRAL vascular system morphologically and functionally is very important for both neuroscientific studies and clinical applications. Numerous clinical problems such as arteriovenous malformation (AVM) (1), tumor evaluation (2–3), and traumatic brain injury (TBI) (4,5) require detailed vascular information for best diagnostic interpretation. Due to the vast differences in hemodynamic characteristics, pathological behavior, and the underlying magnetic resonance imaging (MRI) principles of vessel-tissue contrast, arteries and veins are usually imaged with separate protocols, leading to increased scanning time and motion-related misregistrations. Recently, there has been a focus on single-scan magnetic resonance angiography and venography (MRV) imaging (6–9) in order to obtain a more complete perspective of the vasculature. Collecting MRA and MRV in a single acquisition gets rid of any potential registration problems and enables a precise review and a complete picture of the relationship between the two vasculature networks.

However, further applications of these MRV methods are hindered by two major, yet conflicting, objectives: enhancing vessel-tissue contrast and distinguishing arteries and veins. In MRA, bright-blood (BB) strategies such as time-of-flight (TOF) and contrast-enhanced MRA (CE MRA) are used to obtain high blood signal while reducing tissue signal as much as possible. MRV, on the other hand, can be most reliably done with dark-blood (DB) methods such as susceptibility-weighted imaging (SWI) (10–12) to selectively suppress venous signal while maintaining high tissue signal for better vein-tissue contrast or arterial saturation. Since the tissue signal is unwanted in MRA scan but is required for optimal venous contrast in SWI, obtaining both simultaneously is a challenge, regardless of whether using single-echo (7), double-echo (6), or multiecho (9) strategies. Gadolinium (Gd)-based contrast agents can be used as either a BB or DB (13) method that can enhance both arteries and veins at the same time due to the global vascular T_1 or T_2 shortening effects; thus, its use will make it more difficult to separate arteries and veins in CE MRA.

Currently the gold standard of angiography is intra-arterial digital subtraction angiography (IADSA) (14,15). The basic principle is to create two different levels of blood signal while keeping tissue signal the same by

¹Department of Radiology, Wayne State University, Detroit, Michigan, USA.

²Shanghai Key Laboratory of Magnetic Resonance, East China Normal University, Shanghai, China.

³Department of Biomedical Engineering, Wayne State University, Detroit, Michigan, USA.

Contract grant sponsor: Department of Defense; Contract grant number: DOD W81XWH-11-1-0493; Contract grant sponsor: Wayne State University; Contract grant number: WSU OVPR 177310.

*Address reprint requests to: Y.Y., MR Research Facility, Department of Radiology, Wayne State University, DRH 5E-13, 3990 John R Road, Detroit, MI 48201. E-mail: mqyeah@gmail.com

Received April 20, 2012; Accepted February 20, 2013.

DOI 10.1002/jmri.24128

View this article online at wileyonlinelibrary.com.

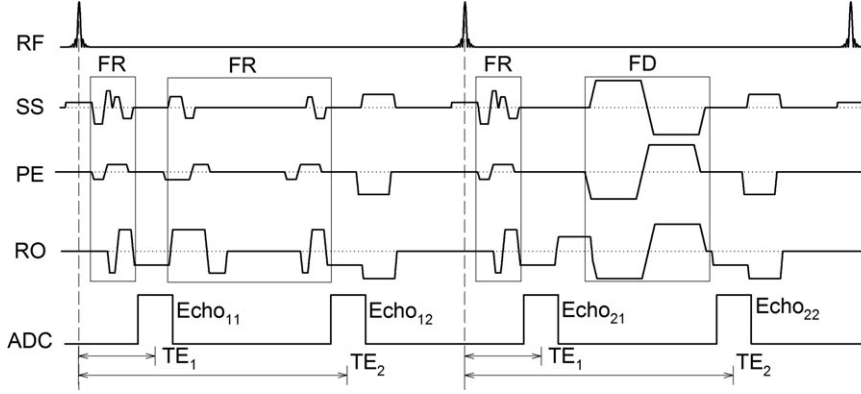


Figure 1. Diagram of the FR/FD interleaved double-echo sequence. Echo₁₁, Echo₁₂, and Echo₂₁ are flow rephased (FR) using first-order moment nulling gradients dynamically calculated with the phase encoding gradients and TEs taken into account, and Echo₁₂ is flow dephased (FD) by bipolar gradients with a low VENC value.

administrating an iodinated contrast agent into the intravascular space, and generate a pure vessel map simply using subtraction. Similar attempts have been made to enhance MRA contrast by using a rephase/dephase strategy to create high/low blood signals while maintaining the tissue signal (16–20). In the recent work by Kimura et al (16), a double-echo sequence collecting flow rephased/dephased images, called hybrid of opposite contrast MRA (HOP-MRA), was developed and a linearly weighted subtraction was proposed to increase the vessel-background contrast by minimizing the subtracted tissue signals. Although capable of enhancing arteries, the major issue of linear subtraction, weighted or not, is that it will introduce heavy venous contamination such that veins also appear bright in the subtracted images. As a result, it is difficult to distinguish between arteries and veins, especially for smaller vessels. The venous contamination can be possibly reduced if both flow rephased and dephased images are acquired with long (preferably equal) TEs, so that veins are already suppressed because of T_2^* decay. With equal TE, the rephase/dephase subtraction can reduce the tissue signal-to-noise level, and can better reveal the arteries after processing such as maximum intensity projection (MIP) or vessel tracking. However, flow compensation at long TE will be less efficient, especially for fast flows, leading to artifacts and signal non-uniformity in large arteries such as carotid arteries (21).

To tackle this challenge, we propose using a flow rephase/dephase interleaved double-echo gradient recalled echo (GRE) sequence capable of MRV imaging and at the same time acquiring both flow rephased and dephased images. A nonlinear subtraction processing method is then proposed for selective MRA enhancement utilizing the flow rephased and dephased images. The performance of both nonlinear and linear subtraction methods will be analyzed and compared for the artery-tissue contrast theoretically and experimentally.

MATERIALS AND METHODS

Sequence Design

In order to acquire MRV data as well as flow dephased data for MRA enhancement (16), we developed a flow rephase/dephase interleaved dual-echo GRE sequence as shown in Fig. 1. In the first TR,

both echoes were fully flow rephased (FR, or flow compensated) on all three axes, while in the second TR the second echo was flow dephased (FD) by a series of bipolar gradient pairs.

Unlike Du and Jin's (6) method in which flow rephasing for the second echo was achieved with a fly-back gradient in the readout direction, we implemented an active scheme for flow rephasing to the second echo on all three axes by dynamically calculating the gradients for first-order moment nulling on each axis, taking into account TE as well as phase encoding or readout gradients (22). In this way, one can independently set the two echoes for their TE, bandwidth, and asymmetry without affecting the flow rephasing performance. Flow dephasing for the second echo was done by using bipolar gradients of very low velocity encoding (VENC) value.

With this sequence, four images will be generated with a single scan: two FR images with a short TE₁ for normal TOF-MRA (Echo₁₁ and Echo₂₁), one FR image with a long TE₂ for SWI (Echo₁₂), and one FD image (Echo₂₂) also with TE₂. Since excellent SWI results can be reliably generated from the Echo₁₂ data (6,10), the following analysis will focus on enhancing MRA contrast and separating venous and arterial signal by assessing and comparing nonlinear subtraction and linear subtraction methods.

Linear Subtraction (LS) vs. Nonlinear Subtraction (NLS)

Since the contrast characteristics of linear subtraction have been extensively discussed in previous studies, interested readers are referred to Kimura *et al*'s article for details (16). Here, we will further assess the effect of different weighting factors in the subtraction and their effects on vessel-tissue contrast.

Denoting the signal intensity under two different imaging conditions (eg, FR and FD) as S and S' , and assuming the same noise standard deviation (SD) σ for both signal levels, one can calculate the signal-to-noise ratio (SNR) of the LS image as:

$$SNR_{LS} = \frac{\Delta S_{LS}}{\sigma\sqrt{1+\alpha^2}} = \frac{S - \alpha S'}{\sigma\sqrt{1+\alpha^2}} = \frac{S(1 - \alpha\beta)}{\sigma\sqrt{1+\alpha^2}} \quad [1]$$

where α is the weighting factor for the subtraction, and $\beta = S'/S$ is defined as the ratio between the two

Table 1
Estimated Signal Ranges of Arteries, Veins, and Tissue in FR and FD Images

	Artery	Vein	Tissue
S (FR)	High	Medium	Medium
S' (FD)	Low	Low	Medium but S' < S

signal levels. The CNR between artery and tissue, i.e., $CNR_{at,ls}$, can be written as:

$$CNR_{at,ls} = \frac{(S_a - S'_a) - \alpha(S_t - S'_t)}{\sigma\sqrt{1 + \alpha^2}} \quad [2]$$

The subscripts “a” and “t” denote artery and tissue, respectively. The vein-tissue $CNR_{vt,ls}$ can be written in the same form. On the other hand, if the signal is nonlinearly weighted in a self-weighted manner (i.e., squared on a voxelwise basis) prior to subtraction so that $\Delta S_{nls} = S^2 - \alpha S'^2$, the noise after NLS can be approximated by:

$$\sigma_{nls} = 2\sqrt{(S^2 + \alpha^2 S'^2)}\sigma \quad [3]$$

and SNR_{nls} can be written as:

$$SNR_{nls} = \frac{S^2 - \alpha S'^2}{\sigma_{nls}} = \frac{S(1 - \alpha\beta^2)}{2\sigma\sqrt{1 + \alpha^2\beta^2}} \quad [4]$$

Comparing with Eq. [1], the β factor now appearing in the denominator in Eq. [4] is the major difference between LS and NLS. The value of β depends on the type of tissue, i.e., whether they are arteries, veins, or parenchymal tissues, and it varies according to their respective rephase/dephase signals and partial volume effects.

The expression for CNR_{nls} between vessels and tissues is much more complicated than the LS version shown in Eq. [2]. From a qualitative point of view, S'_a and S'_v will be very low or even nulled as a combined result of low VENC gradients along with high flow velocity (for arteries) or T_2^* decay (for veins), while S_a will be higher than S_v thanks to greater TOF inflow. For static parenchymal tissues, on the other hand, the dephasing gradients will not significantly change the signal as its equivalent diffusion weighting effects are negligible (see next session). However, since in our sequence S' is collected with longer TE so that it will decay (relative to S collected at short TE) by $\sim 20\%$ with a typical ΔTE of 15 msec and a tissue T_2^* of 80 msec at 3T, so that $\beta < 1$ remains true for tissues. The summary of the above analysis is listed in Table 1. Generally speaking, β will be of low value for both arteries and veins (especially for arteries due to the high S_a), but is expected to be around 0.8 for tissues mainly due to T_2^* decay.

To confirm this, we performed Monte Carlo simulations according to Eqs. [1–4] to evaluate the signal change ΔS_{ls} and ΔS_{nls} , noise SD, and SNR for all $S > S'$ (i.e., $\beta < 1$) combinations. S and S' ranged from 1 to 300 and were added with Gaussian noise ($\sigma = 10$), yielding a maximum SNR of about 30 in the original

signals. Also, simulation on the effect of weighting factor α to ΔS_{ls} and ΔS_{nls} are also performed to estimate and predict its optimal value.

Data Acquisition and Processing

Six healthy volunteers (two males and four females, age 27 ± 4 years) were recruited for the study and written consents approved by the local Institutional Review Board were obtained from each volunteer prior to the scans. All scans were performed on a Siemens 3T Verio system (Siemens Healthcare, Erlangen, Germany) with a product 32-channel head coil. The scanning parameters of the FR/FD interleaved double-echo GRE sequence were: $TE_1/TE_2/TR = 6.2/22/28$ msec, flip angle (FA) = 15° , bandwidth = 260 Hz/pixel, voxel size = $0.5 \times 0.5 \times 1.0$ mm³, slice number = 48, and total scan time was 6 minutes 40 seconds. The bipolar gradients for flow dephasing were 4 msec in duration and 24 mT/m in amplitude, leading to a VENC value of about 1.46 cm/s. As a side note, previous literature on similar studies used the b value (16) rather than the VENC value for describing the dephasing effects. However, the b values are actually too small to introduce significant difference observed in the vessels (eg, $b = 2$ s/mm² reported previously (16) and $b = 1.8$ s/mm² in our case), thus the blood signal loss in the FD image is primarily due to flow dephasing effects. One of the subjects also additionally underwent low-dose contrast-enhanced MRA scans with an injection of 5 cc Magnevist (gadopentate dimeglumine), and single echo flow rephased GRE sequence was scanned using a matching protocol (with $TE/TR = 6.2/28$ msec and FA = 15°) to collect CE TOF MRA images as comparison to the subtraction results. GRAPPA with an acceleration factor of 2 was used for all scans.

SWI results were calculated from the flow rephased $Echo_{12}$ data, using a highpass filter of 64×64 on the phase image and a four-time phase mask multiplication (i.e., $m = 4$) (10). mIP images over a 12-mm slab were created to better visualize the veins as continuous structures.

For both LS and NLS calculations, the two identical short TE FR images (i.e., $Echo_{11}$ and $Echo_{21}$) were averaged to improve SNR especially for arteries, and the averaged image was used as S . Taking the FD image as S' , LS and NLS results were then calculated with $\alpha = 0.75, 1.00$, and 1.25 , respectively. MIP images over a 12-mm slab were also created for all final results to display the arteries. The skull signal was removed for better visualization using SPIN (Signal Processing In NMR, Detroit, Michigan), and a brain-only binary mask was obtained and applied to all processed data described above (but prior to intensity projections) to remove the skull.

The artery-tissue CNR of different artery sizes was also determined to evaluate the artery enhancing performance on various vessel sizes. The contrast was determined by subtracting the mean signal intensity of the surrounding tissue from the signal maxima of the artery segment, and noise was taken as the SD of the tissue signal. The artery diameter was estimated as the

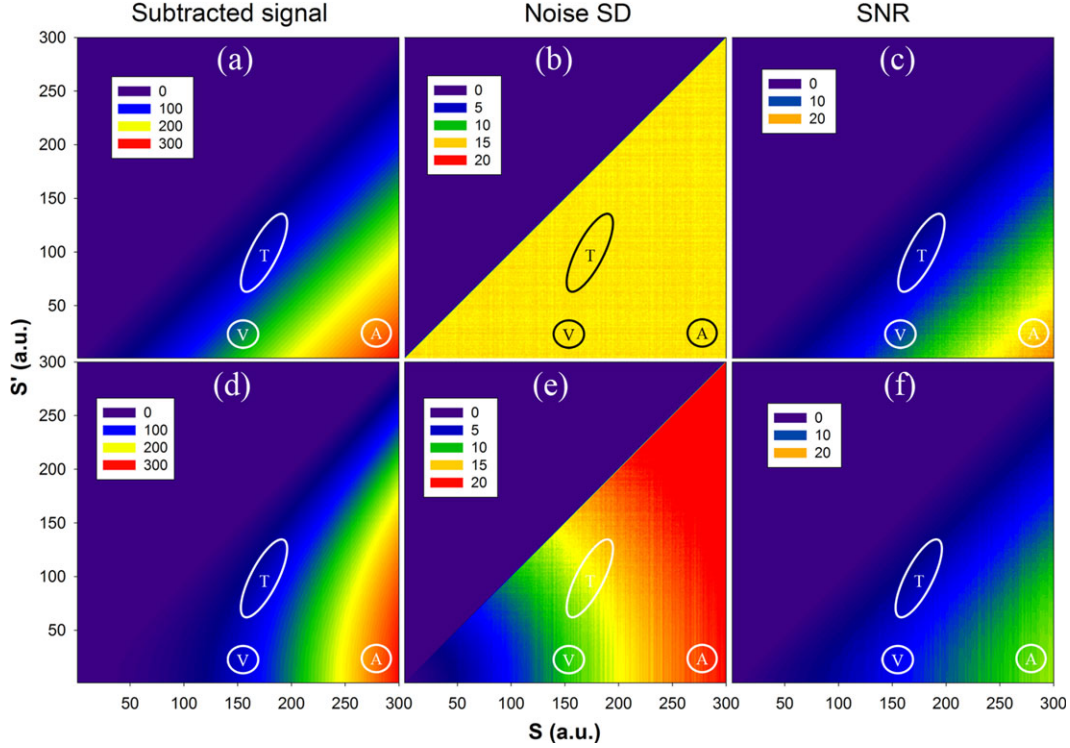


Figure 2. Simulation results of the subtraction signal (ΔS_{ls} in (a) and ΔS_{nls} in (d)), noise SD (b,e), and the resulting SNR (c,f) of LS (a-c) and NLS (d-f). The simulation was performed for all $S > S'$ (i.e., $\beta < 1$) combinations, and $\alpha = 1$ and $\sigma = 10$ was used for calculations here. Higher temperature color corresponds to higher subtraction signal (a,d), or higher noise SD (b,e), or higher SNR of the subtracted image (c,f). The three ROIs indicate the estimated regions for arteries ("A"), veins ("V") and tissues ("T") signals. The color scales of NLS were scaled to match the range of LS for the columns of subtracted signal and noise SD.

half-width-maximum-height of its profile and was sorted into several groups: less than 1 mm, 1–1.5 mm, 1.5–2 mm, and 2–2.5 mm. For each group, five vessels were selected and the mean and SD of CNR were evaluated.

RESULTS

The simulation comparing LS and NLS are shown in Fig. 2, where the estimated signal regions for arteries, veins, and tissues are indicated according to Table 1. The simulation confirmed that the introduction of factor β into the denominator in Eq. [4] modifies the nonlinear subtraction outcomes between rephased and dephased signals. Specifically, the gradient of ΔS_{nls} is shifted towards high S when S' values are low, but the shift is much less significant for medium to high S' values (Fig. 2d). For LS, ΔS_{ls} of the veins is higher than that of the tissues, thus showing a positive vein-tissue contrast (Fig. 2a). However, venous ΔS_{nls} is located at the same gradient level with the tissues, effectively reducing or even eliminating the vein-tissue contrast. Meanwhile, both ΔS_{ls} and ΔS_{nls} of the arteries remain very high (hot colors), maintaining a high contrast to the tissues (Fig. 2d). In light of the above results, it is predicted that both veins and arteries will be shown in the LS approach, while predominantly only arteries will be visible in the NLS approach.

The weighting factor α was introduced in order to best null the subtracted tissue signal (16). The effect

of α is to "tilt" the gradient of ΔS_{ls} or ΔS_{nls} , as demonstrated in Fig. 3, where simulations using $\alpha = 0.5$, 1.0, and 1.5 were compared. When a higher α value is used, ΔS_{ls} will reduce more at high S' values. For practical considerations, since S' of tissues is higher than both arteries and veins in the dephased images, one can expect to see a more decreased tissue signal in the LS images with higher α value. This is consistent with the suggested optimal value of 1.5 for α (16). However, the difference in ΔS_{ls} between veins and arteries will also become greater with high α value due to the reduced tissue signal (Fig. 3a-c), suggesting an even increased vein-tissue contrast in the LS results. For the nonlinear approach, ΔS_{nls} of both veins and tissues only vary slightly between α values, and the vein-tissue contrast in the NLS results is minimal and insensitive to the weighting factor (Fig. 3e,f).

The single slice images of the unprocessed FR and FD data along with the LS/NLS processed data of one representative subject are shown in Fig. 4, while the corresponding MIP or mIP results are shown in Fig. 5. These images show several representative arteries and veins that can be used as a demonstration of our approach. The profiles of a pair of neighboring artery and vein, normalized by the respective maximum signal, were extracted as indicated by the thin black line in Fig. 4a and shown in Fig. 6, and the vessel-tissue contrast and CNR value of these vessels are shown in Table 2. The contrast was calculated as the signal difference between vessel center and surrounding

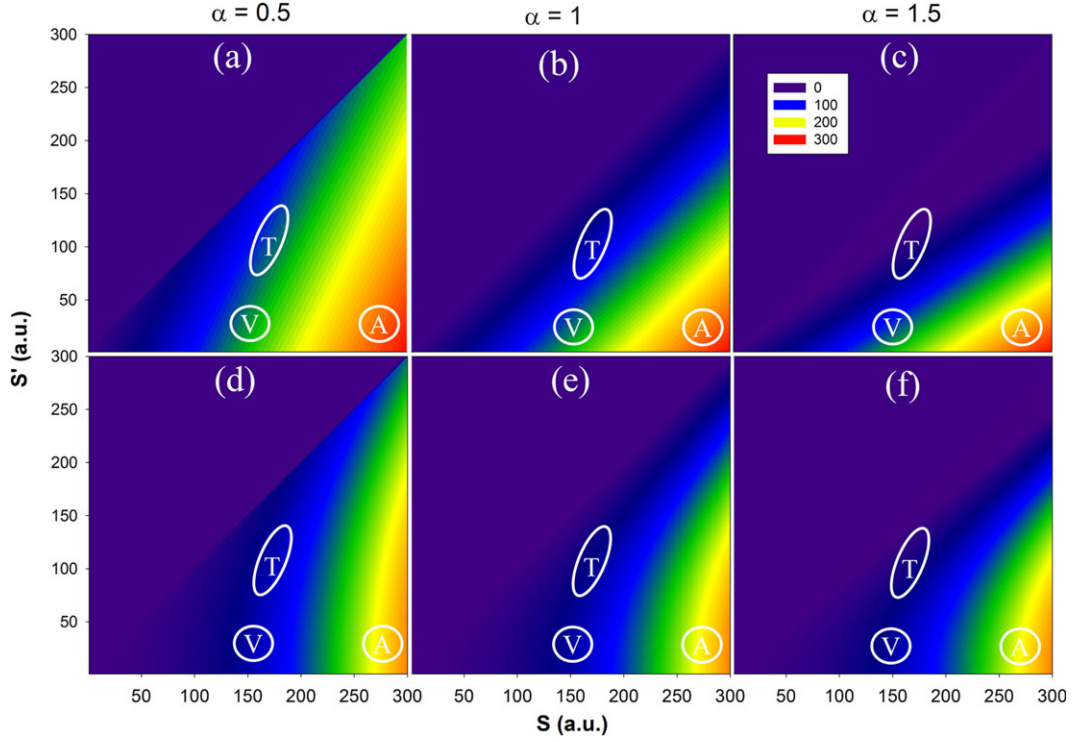


Figure 3. Simulation results of the subtraction signal ΔS_{ls} (a–c) and ΔS_{nls} (d–f), with $\alpha = 0.5$ (a,d), 1 (b,e), and 1.5 (c,f), respectively. The color gradients of NLS were scaled to match the range of LS.

tissues divided by the tissue signal mean, and the CNR was calculated as the signal difference between vessel center and surrounding tissues divided by the standard deviation of tissue signal. The β value was about 0.07 and 0.27 for the artery and the vein (calculated at the vessel profile center), respectively, and was about 0.79 for the surrounding tissues, which is in agreement with the above theoretical analysis. The comparison between LS, NLS, and low-dose CE TOF MRA are similarly shown in Fig. 7, and the artery-tissue CNR of different artery sizes are shown in Fig. 8.

DISCUSSION

In this study we proposed an MRAV imaging method with selective MRA enhancement. Specifically, we designed an FR/FD interleaved double-echo GRE sequence which, for the first time, offers the capacity of obtaining both fully flow rephased SWI data for venography and TOF MRA with selectively enhanced angiography and minimal venous contamination. Specifically, a dynamic full flow compensation scheme and a nonlinear subtraction method were proposed to achieve the above objectives.

For noncontrast-enhanced MRA, the 3D TOF method is most widely used for clinical exams for its potential to image small, tortuous arteries noninvasively. TOF MRA creates a positive artery-tissue contrast as a result of the in-flowing arterial blood being much less saturated than the static tissues. However, the in-flowing blood will gradually become saturated as it passes through the imaging slab, losing the

contrast especially for smaller vessels with slow flow. There are several means to increase the contrast for small arteries, including using magnetization transfer contrast (MTC) radiofrequency (RF) pulse to suppress tissue signal (23,24), multiple thinner slabs to reduce saturation effect (25), TONE pulse for spatially varying flip angle excitation (26), or acquiring an additional flow dephased image and then subtract it from the flow rephased image (16–20). The subtraction method is of particular interest as it can greatly reduce or even null the background tissue signal while retaining high vessel signal. Furthermore, a common dilemma for existing MRAV methods is the conflicting requirement on tissue signal, that TOF MRA requires low tissue signal while SWI-based MRV requires high tissue signal. This now can be perfectly addressed with our interleaved double-echo MRAV sequence, as one can have sufficient tissue signal for SWI using a proper flip angle and have reduced tissue signal for MRA after subtraction.

The major drawback of the LS method is that as the venous blood is also suppressed by the dephasing gradients, vein-tissue contrast will become positive and confounds the interpretation of the MRA results. Previous studies mainly focused on maximizing the artery-tissue contrast, but failed to address such venous contamination issue (16,17). Compared to LS methods, the proposed NLS method is proven to be able to enhance the artery-tissue contrast while suppressing the venous-tissue contrast (Figs. 4–7). Self-weighted NLS reduces the vein-tissue contrast by additionally taking into account the signal intensity of both rephased and dephased states, i.e., tissues have low

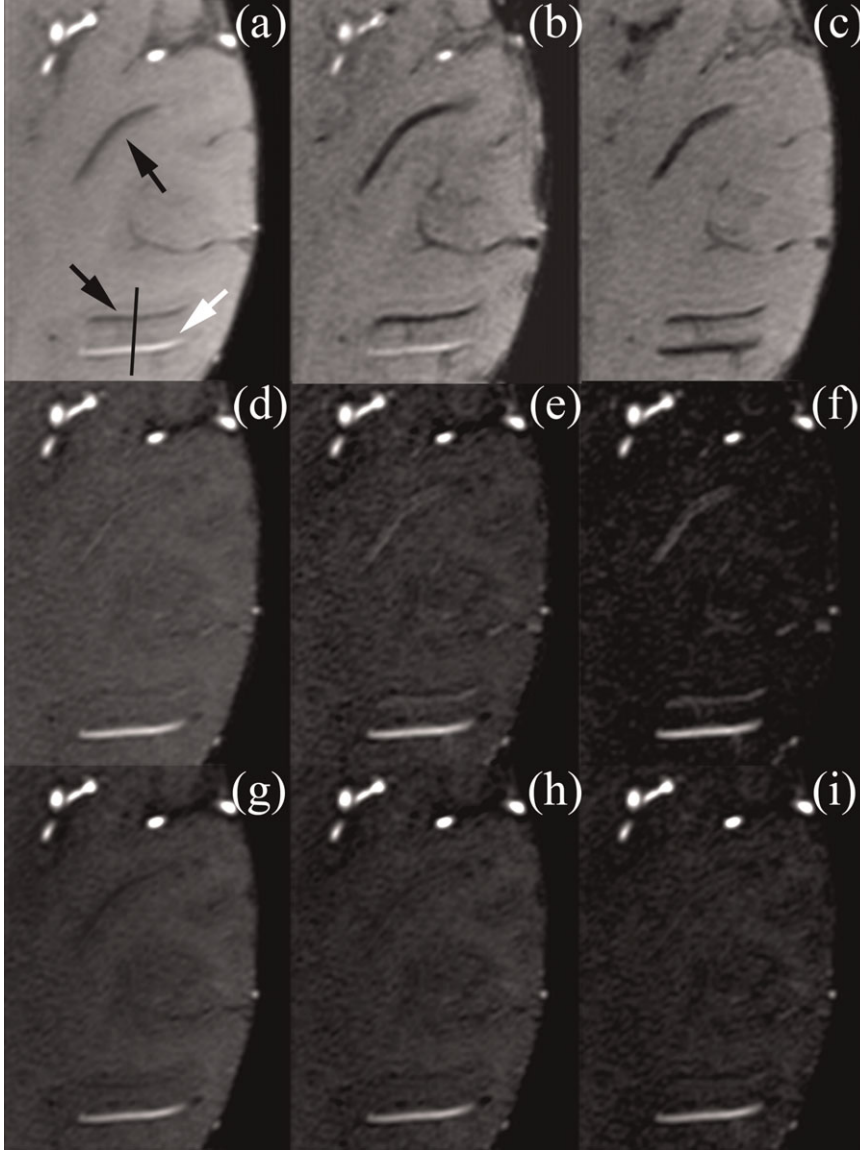


Figure 4. Top row: single slice images of (a) TOF images from the averaged FR echoes, (b) SWI from Echo₁₂, (c) FD dark blood data from Echo₂₂. Middle row: LS results using (d) $\alpha = 0.75$, (e) $\alpha = 1.00$, and (f) $\alpha = 1.25$. Bottom row: NLS results using (g) $\alpha = 0.75$, (h) $\alpha = 1.00$, and (i) $\alpha = 1.25$. Black and white arrows indicate two veins and one artery of interest; the thin black line indicates the location at which the vessel profiles are drawn for Fig. 6. The display window was the same among each row, except for the SWI image, which was individually adjusted.

$S - S'$ but high $S + S'$ while veins have high $S - S'$ but low $S + S'$, and therefore both have similar $S^2 - S'^2$.

Apart from the linearity or nonlinearity, the weighting factor α in the subtraction also alters the vessel-tissue contrast by changing the ΔS distribution, as demonstrated in Fig. 3. With a greater α factor, the LS method indeed was able to enhance artery-tissue contrast by reducing tissue signal, but also further enhanced the vein-tissue contrast (Fig. 6b). These enhanced veins may be misinterpreted as small arteries (Fig. 5) that have medium to low contrast due to partial volume effects or steady-state saturation effects. The vein-tissue contrast is minimized in NLS due to the fact that both veins and tissues are of similar ΔS_{NLS} level, and the slight variation of tissue signal between different α values does not significantly change their contrast. Although using $\alpha = 0.75$ in LS can also lead to minimal vein-tissue contrast, the artery-tissue CNR is reduced by over 23% compared to $\alpha = 1.25$ (Fig. 6b and Table 2). Note that there was a large increase in CNR of LS with $\alpha = 1.25$. This was because the tissue signal was completely subtracted

out since $\alpha\beta \approx 1$, thus the noise distribution changed from Gaussian to Raleigh and resulted in a smaller standard deviation. For NLS, in contrast, such variation in CNR is less than 3% between all α values, and α around 1 is seen to sufficiently eliminate the vein-tissue contrast (Fig. 6c and Table 2). We observed such insensitivity of α in NLS results in all subjects. This means that one simply needs to square the rephased/dephased images and subtract them in order to obtain clean, enhanced angiography.

To better demonstrate the MRA enhancing effects of LS and NLS, we also collected low-dose CE TOF MRA data for comparison. By using low-dose contrast agent (5 cc), low flip angle (15°), and long TR (28 msec), the T_1 shortening effect of the contrast agent is mainly utilized to minimize saturation of the blood signal so as to maximize TOF effects, rather than using the steady-state T_1 enhancement, as in full-dose CE MRA. Although T_1 weightings may still contribute more or less to the enhanced blood signal, such an effect is not strong, as evidenced by the lack of most slow-flowing veins in Fig. 7d and the identical

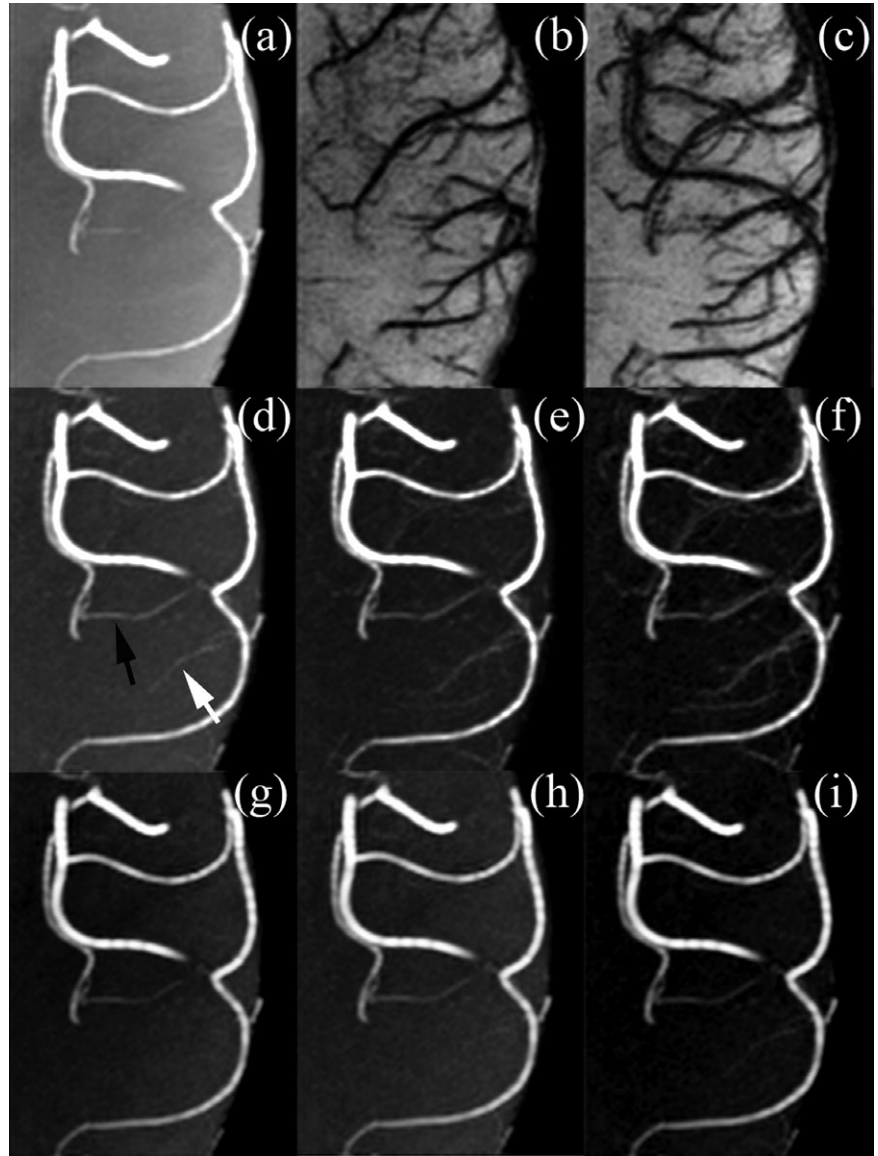


Figure 5. Corresponding MIP (or mIP) images of Fig. 4. The white and black arrows in (d) indicate an artery and a vein, respectively. All results shown were projected over a 1–2-mm slab.

artery-tissue contrast between normal TOF and 5 cc data in Fig. 7e. Were the T_1 shortening effect strong, veins would also have become visible and artery-tissue contrast would be higher. By this means, one can establish an upper baseline for maximal TOF effects in arteries to compare the performance of LS and NLS

with. As shown in Fig. 7, arteries are enhanced in all three results being compared. Most noticeably, NLS seems to even outperform the CE TOF data by its higher artery-tissue contrast (Figs. 7e, 8), extra revelation of some small arteries (e.g., near the frontal part), uniform background signal, and the lack of

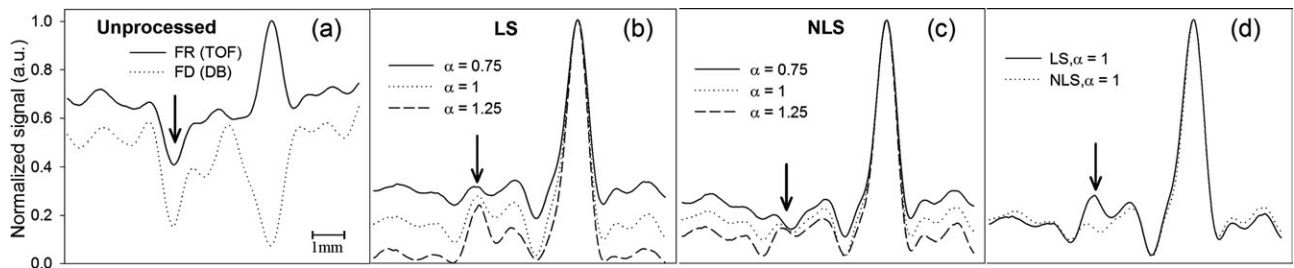


Figure 6. Normalized vessel profiles of a vein and an artery from (a) unprocessed FR (TOF) and FD (dark blood) data, (b) LS processed data, (c) NLS processed data, and (d) comparison between LS and NLS. The arrows indicate the center of the vein, which will not be seen in some cases due to reduced contrast with surrounding tissues. Quantification of contrast and CNR are shown in Table 2. The diameter of this artery was ~ 2 mm.

Table 2

Vessel-Tissue Contrast of the Artery and the Vein Whose Profile Was Indicated by the Black Line in Fig.4a

	Artery		Vein	
	Contrast (%)	CNR	Contrast (%)	CNR
TOF(FR)	28.3	5.5	-37.2	-7.2
LS ($\alpha=0.75/1.00/1.25$)	206.1/453.8/2493.3	17.8/17.8/23.2	-3.5/37.4/366.4	-0.3/1.5/3.4
NLS ($\alpha=0.75/1.00/1.25$)	255.4/389.4/680.8	15.5/15.6/15.2	-35.2/-20.0/12.6	-2.1/-0.8/0.3

veins or the contrast-enhanced choroid plexus. LS offers similar artery-tissue contrast with NLS but also lots of venous signal, making it very much like the routine full-dose CE MRA data (data not shown). The comparison confirms that the proposed self-weighted NLS method is potentially capable of revealing the

maximal arterial TOF effect without the use of contrast agent. One thing worth mentioning is that due to its fast flow, the superior sagittal sinus would also appear bright in all methods compared (Fig. 7), albeit it can be easily distinguished. Inferior sagittal sinus, however, is only seen with contrast agent (Fig. 7d) but not in TOF, LS, or NLS results.

Due to partial volume effects and blood flow velocity, it is expected that the CNR_{at} may vary according to artery sizes. Moreover, because squaring the image in NLS will amplify the noise by twice the original signal intensity, SNR_{nls} will have lower value than SNR_{ls} (Fig. 2f vs. 2c) on a voxelwise basis. According to Fig. 8, CNR_{at} becomes greater for larger vessels with all methods, which is expected. Paired *t*-test results indicate that CNR_{at} of NLS is significantly greater than LS for arteries larger than 1.5 mm (two-tailed $P = 0.046$ and 0.035 for 1.5–2.0 mm and 2.0–2.5 mm groups, respectively), while both have similar CNR_{at} for those smaller than 1.5 mm ($P = 0.126$ and 0.395 for <1mm and 1.0–1.5 mm groups, respectively). This indicates that NLS results are similar to LS for small arteries, but will significantly outperform LS for larger arteries (Figs. 7, 8).

On the other hand, since veins have very low signal while arteries still have high signal (provided competent flow rephasing) in SWI processed images, multiplying with the SWI processed magnitude mask may also help suppress the veins in the LS results (10,27), and we have also tested this method using the same data we collected (results not shown). For large

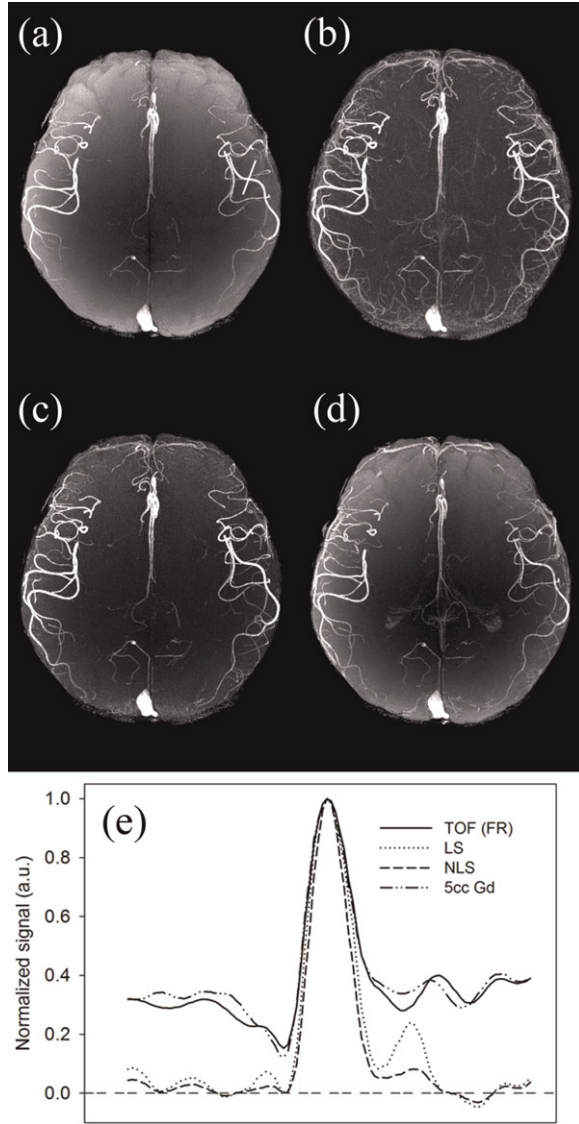


Figure 7. MIP images of (a) TOF MRA, (b) LS, (c) NLS, and (d) low-dose CE MRA with 5 cc gadopentetate dimeglumine. (a–c) Collected with a single scan of the FR/FD interleaved double-echo sequence before the use of contrast agent, and α was 1 for both LS and NLS calculation. (e) Comparison of the normalized profiles of one representative artery as shown in (a), extracted from the corresponding single slice images.

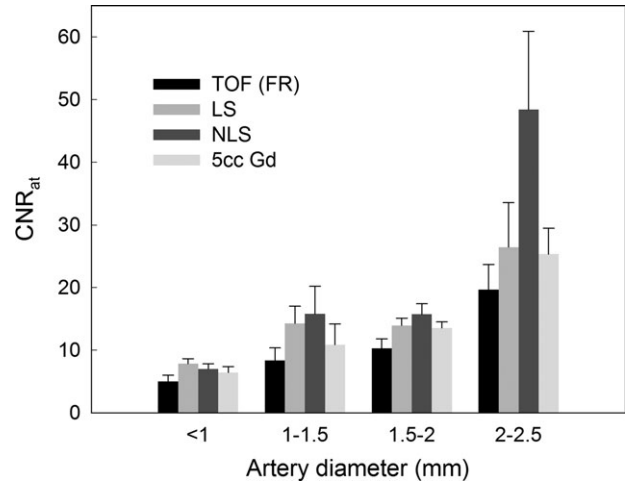


Figure 8. Artery-tissue CNR of different artery size groups. Two-tailed paired *t*-test results between LS and NLS are: $P = 0.126$ for <1 mm, $P = 0.395$ for 1–1.5 mm, $P = 0.046$ for 1.5–2 mm and $P = 0.035$ for 2–2.5 mm.

arteries, masking with SWI images also yielded very high artery-tissue contrast and negative vein-tissue contrast. Smaller arteries, on the other hand, were not as equally enhanced as in LS or NLS, probably due to the local signal variations and increased noise caused by phase masking process. Another potential drawback of this SWI masking method would be the introduction of susceptibility artifacts commonly seen in SWI images (11), which may suppress nearby arteries due to signal dropout especially at the edge of the brain. The SWI masking method may find itself useful in full-dose CE MRA scans, in which both arteries and veins display high values in the original images, rendering both subtraction methods less effective in reducing venous signals. By integrating phase information, the SWI masking method may have the potential to selectively suppress the veins even with the presence of contrast agent.

The major drawback of the interleaved design of the sequence is that it still requires approximately the same total scan time as the separate acquisition of both MRA and SWI data. However, compared to separate acquisition of both MRA and SWI, our MRV method offers strictly aligned images for direct and accurate comparison between the two vascular networks, and a selectively enhanced MRA map that surpasses any existing noncontrast-enhanced MRA or MRV methods. Also with proper adjustment in scanning parameters, this method may have the potential for MRV imaging of proximal vessels such as the carotid arteries and the jugular veins in the neck.

In conclusion, we have proposed an FR/FD interleaved double-echo MRV sequence which for the first time can provide both fully flow-compensated SWI results and selective MRA enhancement in a single scan, while maintaining a good balance between the two contrast sets. Three different types of images, i.e., TOF MRA, SWI, and flow dephased, could be obtained simultaneously with perfect alignment to each other so that no realignment process is necessary. In conjunction with NLS, one can obtain high-resolution SWI and enhanced TOF MRA without the need for contrast agent, and the process can be easily automated with minimal additional computational power. NLS offers a clean TOF angiography free of venous contamination as if acquired with minimal saturation effects. For future works, the acquisition time may be further reduced to provide whole brain coverage using a segmented echo planar imaging (EPI) readout approach (28) or compress sensing (29–31) since the subtracted images contain highly sparse information of arteries. Also, a TONE pulse may be implemented with proper flip angle range to further improve the enhanced MRA results while maintaining high SWI contrast.

REFERENCES

1. Marchal G, Bosmans H, Van Fraeyenhoven L, et al. Intracranial vascular lesions: optimization and clinical evaluation of three-dimensional time-of-flight MR angiography. *Radiology* 1990;175:443–448.
2. van den Berg R, Verbist BM, Mertens BJ, van der Mey AG, van Buchem MA. Head and neck paragangliomas: improved tumor detection using contrast-enhanced 3D time-of-flight MR angiography as compared with fat-suppressed MR imaging techniques. *AJNR Am J Neuroradiol* 2004;25:863–870.
3. Sehgal V, Delproposto Z, Haddad D, et al. Susceptibility-weighted imaging to visualize blood products and improve tumor contrast in the study of brain masses. *J Magn Reson Imaging* 2006;24:41–51.
4. Kohler R, Vargas MI, Masterson K, Lovblad KO, Pereira VM, Becker M. CT and MR angiography features of traumatic vascular injuries of the neck. *Am J Radiol* 2011;196:W800–809.
5. Shen Y, Kou Z, Kreipke CW, Petrov T, Hu J, Haacke EM. In vivo measurement of tissue damage, oxygen saturation changes and blood flow changes after experimental traumatic brain injury in rats using susceptibility weighted imaging. *Magn Reson Imaging* 2007;25:219–227.
6. Du YP, Jin Z. Simultaneous acquisition of MR angiography and venography (MRV). *Magn Reson Med* 2008;59:954–958.
7. Barnes S, Haacke E. Single echo simultaneous angiography and venography (MRV) techniques at 3T. In: *Proc 17th Annual Meeting ISMRM*, Honolulu; 2009. p 1861.
8. Park SH, Moon CH, Bae KT. Compatible dual-echo arteriovenography (CODEA) using an echo-specific K-space reordering scheme. *Magn Reson Med* 2009;61:767–774.
9. Du YP, Jin Z, Hu Y, Tanabe J. Multi-echo acquisition of MR angiography and venography of the brain at 3 Tesla. *J Magn Reson Imaging* 2009;30:449–454.
10. Haacke EM, Xu Y, Cheng YC, Reichenbach JR. Susceptibility weighted imaging (SWI). *Magn Reson Med* 2004;52:612–618.
11. Haacke EM, Mittal S, Wu Z, Neelavalli J, Cheng YC. Susceptibility-weighted imaging: technical aspects and clinical applications, Part 1. *AJNR Am J Neuroradiol* 2009;30:19–30.
12. Mittal S, Wu Z, Neelavalli J, Haacke EM. Susceptibility-weighted imaging: technical aspects and clinical applications, Part 2. *AJNR Am J Neuroradiol* 2009;30:232–252.
13. Lin W, Mukherjee P, An H, et al. Improving high-resolution MR bold venographic imaging using a T1 reducing contrast agent. *J Magn Reson Imaging* 1999;10:118–123.
14. Brown BG, Bolson E, Frimer M, Dodge HT. Quantitative coronary arteriography: estimation of dimensions, hemodynamic resistance, and atheroma mass of coronary artery lesions using the arteriogram and digital computation. *Circulation* 1977;55:329–337.
15. Coatrieux JL, Garreau M, Collorec R, Roux C. Computer vision approaches for the three-dimensional reconstruction of coronary arteries: review and prospects. *Crit Rev Biomed Eng* 1994;22:1–38.
16. Kimura T, Ikeda M, Takemoto S. Hybrid of opposite-contrast MR angiography (HOP-MRA) combining time-of-flight and flow-sensitive black-blood contrasts. *Magn Reson Med* 2009;62:450–458.
17. Axel L, Morton D. MR flow imaging by velocity-compensated/uncompensated difference images. *J Comput Assist Tomogr* 1987;11:31–34.
18. James E, Potchen MD, Haacke EM. *Magnetic resonance angiography: concepts & applications*. St. Louis: Mosby YearBook; 1993. p 169–170.
19. Wedeen VJ, Meuli RA, Edelman RR, et al. Projective imaging of pulsatile flow with magnetic resonance. *Science* 1985;230:946–948.
20. Laub GA, Kaiser WA. MR angiography with gradient motion refocusing. *J Comput Assist Tomogr* 1988;12:377–382.
21. Jeong EK, Parker DL, Tsuruda JS, Won JY. Reduction of flow-related signal loss in flow-compensated 3D TOF MR angiography, using variable echo time (3D TOF-VTE). *Magn Reson Med* 2002;48:667–676.
22. Haacke EM, Brown R, Thompson M, Venkatesan R. *Magnetic resonance imaging. Physical principles and sequence design*. New York: Wiley-Liss; 1999. p 670–697.
23. Edelman RR, Ahn SS, Chien D, et al. Improved time-of-flight MR angiography of the brain with magnetization transfer contrast. *Radiology* 1992;184:395–399.
24. Atkinson D, Brant-Zawadzki M, Gillan G, Purdy D, Laub G. Improved MR angiography: magnetization transfer suppression with variable flip angle excitation and increased resolution. *Radiology* 1994;190:890–894.
25. Parker DL, Yuan C, Blatter DD. MR angiography by multiple thin slab 3D acquisition. *Magn Reson Med* 1991;17:434–451.

26. Tkach J, Masaryk T, Ruggieri P. Use of tilted optimized nonsaturating excitation. SMRM. Vol. 2. Berlin: 1992. p 3095.
27. Ishimori Y, Monma M, Kohno Y. Artifact reduction of susceptibility-weighted imaging using a short-echo phase mask. *Acta Radiol* 2009;50:1027–1034.
28. Xu Y, Haacke EM. An iterative reconstruction technique for geometric distortion-corrected segmented echo-planar imaging. *Magn Reson Imaging* 2008;26:1406–1414.
29. Lustig M, Donoho D, Pauly JM. Sparse MRI: the application of compressed sensing for rapid MR imaging. *Magn Reson Med* 2007;58:1182–1195.
30. Wu B, Li W, Guidon A, Liu C. Whole brain susceptibility mapping using compressed sensing. *Magn Reson Med* 2012;67:137–147.
31. Cukur T, Lustig M, Saritas EU, Nishimura DG. Signal compensation and compressed sensing for magnetization-prepared MR angiography. *IEEE Trans Med Imaging* 2011;30:1017–1027.